To the Graduate Council:

I am submitting herewith a dissertation written by Erik Gregory Herbert entitled "An Experimental Investigation of the Elastic and Viscoelastic Properties of Small Volumes of Material." I have examined the final electronic copy of this dissertation for form and content and recommend that it be accepted in partial fulfillment of the requirements for the degree of Doctor of Philosophy, with a major in Materials Science and Engineering.

George M. Pharr
Major Professor

We have read this thesis
and recommend its acceptance:

Warren C. Oliver

Dayakar Penumadu

Easo P. George

Accepted for the Council:

Carolyn R. Hodges

Vice Provost and Dean of the
Graduate School

(Original signatures are on file with official student records.)

An Experimental Investigation of the Elastic and Viscoelastic Properties of Small Volumes of Material

A Dissertation
Presented for the
Doctor of Philosophy
Degree
The University of Tennessee, Knoxville

Erik Gregory Herbert
August 2008

Abstract

The purpose of this work is to further develop experimental methodologies using flat punch nanoindentation to measure the constitutive behavior of viscoelastic solids in the frequency and time domain. The reference material used in this investigation is highly plasticized polyvinylchloride (PVC) with a glass transition temperature of -17 degrees Celsius. The nanoindentation experiments were conducted using 103 and 983 micron diameter flat punches. For comparative purposes, the storage and loss modulus obtained by dynamic mechanical analysis are also presented. Over the frequency range of 0.01 to 50 Hz, the storage and loss modulus measured using nanoindentation and uniaxial compression are shown to be in excellent agreement. The creep compliance function predicted from nanoindentation data acquired in the frequency domain is also found to be in excellent agreement over two decades in time with the creep compliance function measured using a constant stress test performed in uniaxial compression. A constraint factor of 1.55 is found to overlay the creep compliance function measured by nanoindentation in the time domain with the creep function measured in uniaxial compression.

A new method is proposed to determine the elastic modulus and residual stress of free-standing thin films based on nanoindentation techniques. The experimentally measured stiffness-displacement response is applied to a simple membrane model that assumes the film deformation is dominated by stretching

as opposed to bending. Experimental verification of the method is demonstrated for Al/0.5 weight percent Cu films nominally 22 microns wide, 0.55 microns thick, and 150, 300, and 500 microns long. The estimated modulus for the four free-standing films matches the value measured by electrostatic techniques within 2 percent, and the residual stress within 19.1percent. The difference in residual stress can be completely accounted for by thermal expansion and a modest change in temperature of 3 degrees Celsius.

Table of Contents

Introduction ……..……..……1

Chapter 1: Nanoindentation and the dynamic characterization of viscoelastic solids ……..……..…4

Abstract ……..……..……5

1. Introduction ……..……..……..6
2. Theory ……..……..…… 9
   - 2.1. The dynamic response of a linear viscoelastic solid 9
   - 2.2. The dynamic response of a damped, forced oscillator – the test instrument ……..... 11
   - 2.3. Determining *E*’ and *E*” in a dynamic nanoindentation experiment ……14
     - 2.3.1. Modeling the sample ……..……..16
3. Experimental measurements ……..…… 17
   - 3.1. Instrument characterization ……..……20
     - 3.1.1. Determining the cutoff frequency ……22
     - 3.1.2. Measuring the reference phase angle ……..…23
     - 3.1.3. Measuring the dynamic stiffness and damping of the testing system ……..…… 23
   - 3.2 Measurement of the complex modulus by dynamic nanoindentation ……...25
     - 3.2.1. Determining full contact with the flat punch .....…26
     - 3.2.2. Generating steady-state harmonic motion ……...27
     - 3.2.3. Determining the linear viscoelastic regime ……... 29
     - 3.2.4. Comparing nanoindentation and DMA results …. 30
4. Summary and conclusions ……..…… 31

Acknowledgements ……..…… 33

References ……..……34

Appendix 1.1. ……..……..35

Chapter 2: Measuring the constitutive behavior of viscoelastic solids in the time and frequency domain using flat punch nanoindentation ……..…48
Abstract ……..…. 49
1. Introduction ……..……..50
2. Theory ……..…53
2.1. Flat Punch nanoindentation …….....53
2.2. Uniaxial compression ……..…….....56
2.3. Constitutive relations ..……..……57
3. Experimental measurements ……..…… 59
4. Results and discussion …..……..…65
4.1. The time domain …… 65
4.2. The frequency domain ……..…… 68
5. Transformation from the frequency domain to the time domain …….72
6. Summary and conclusions ……..…….74
References ……76
Appendix 2.1. ……..……..…77

Chapter 3: Measuring the elastic modulus and residual stress of free-standing thin films using nanoindentation techniques ……..… 95
Abstract ……..…. 96
1. Introduction ……..……..97
1.1. Sample geometry and properties …….…… 102
2. Theory ……..…. 104
2.1. The proposed membrane model ……..…….…..... 104
2.2. Limitations of the model ……..... 107
3. Experimental measurements ……..…… 109
3.1. Minimizing thermal drift effects ……..……..... 111
3.2. Determination of the film thickness ……..... 114
3.3. The measured stiffness-displacement response of doubly-clamped, free-standing thin film bridges ……..…..... 115
4. Summary and conclusions …..……..…… 120

References …… 122
Acknowledgements …… 124
Appendix 3.1. …… 125
Appendix 3.2. ……128
Vita ……...140

List of Figures

Figure 1.1. Schematic illustrations showing the imaginary and real components of a) the complex modulus of a linear viscoelastic solid subject to sinusoidal loading, b) the frequency response of a damped, forced oscillator, and c) the combined frequency response of a viscoelastic solid (sample) and a damped, forced oscillator (instrument). ..…36

Figure 1.2. a) A schematic illustration of the testing system and the dynamic model used to describe the behavior of the system as a function of frequency. b) The dynamic model used to describe the combined frequency response of the instrument and sample. Throughout this work, the load frame is assumed to be rigid relative to the stiffness of the support springs, K_s. ……..……..…39

Figure 1.3. a) The phase angle as a function of frequency, measured in increments of 1 Hz with the indenter column hanging in free space. The discontinuity at 53 Hz indicates the point at which the difference in stiffness between the *z* and *x-y* plane is no longer large enough to prevent cross-talk. b) The reference phase angle as a function of frequency, measured with the indenter column hanging in free space and at the same frequencies to be used in characterizing the sample. ……..……..……..……..…40

Figure 1.4. The dynamic stiffness and damping of the testing system as a function of frequency, measured with the indenter column hanging in free space and at the same frequencies to be used in characterizing the sample. The indenter is positioned at the raw displacement (position in the capacitance gauge) that corresponds to full contact. ……..…… 42

Figure 1.5. The harmonic displacement and phase angle as a function of raw displacement. These data are used to determine the raw displacement at both the point of initial contact and full contact between the face of the punch and the surface of the sample. The criterion for initial contact is a specified change in the phase angle. The criterion for full contact is a specified time rate of change in the harmonic displacement. 43

Figure 1.6. The raw displacement and oscillation amplitude as a function of time for a typical measurement performed on the sample. At each frequency, the harmonic load is different but fixed. The resulting oscillation amplitude is constant at each frequency only because the contact area does not change, despite the transient behavior in the raw displacement. 44

Figure 1.7. The storage modulus and loss factor as a function of frequency and static pre-compression distance. These data show that the static pre-compression distance must be less than 5 μm in order to generate data consistent with the assumptions of linear viscoelasticity. 45

Figure 1.8. The storage modulus and loss factor as a function of frequency and oscillation amplitude. These data clearly show that oscillation amplitudes ranging from 50 to 3000 nm generate data consistent with the assumptions of linear viscoelasticity. 46

Figure 1.9. The complex modulus as a function of frequency as determined by dynamic nanoindentation and DMA. 47

Figure 2.1. The load on sample and the displacement into surface as a function time, a) Data representing a complete experiment, b) Restricting the strain and stabilizing the contact, c) The creep measurement, showing a 6 mN step load and the resulting displacement-time response, and d) Dynamic characterization at 0.5 and 1 Hz. …...78

Figure 2.2. The creep displacement as a function of time, measured in uniaxial compression in response to a 6 mN step load. The displacement-time response is shown for 4 different pre-loads, 100, 200, 300, and 400 mN. ……82

Figure 2.3. The creep compliance function measured in uniaxial compression and by flat punch nanoindentation. The data illustrate 1 of the 5 measurements performed using each technique. …….. 83

Figure 2.4. The relaxation rate versus time acquired during a flat punch nanoindentation experiment performed with an 80 mN pre-load followed by a stabilization criterion of 0.3 nm/s. ……..…….. 84

Figure 2.5. a) The displacement-time response measured by flat punch nanoindentation. The 1 and 3 mN data are corrected to account for the relaxation rate associated with the pre-load. b) The 1 and 3 mN data multiplied by 6 and 2, respectively, showing the data are consistent with the assumptions of linear viscoelasticity. ……85

Figure 2.6. A typical elliptical lisajous figures showing the load-displacement response at 0.01 Hz measured by flat punch nanoindentation. ...87

Figure 2.7. a) The storage modulus and b) the loss factor as a function of frequency as determined in uniaxial compression, by flat punch nanoindentation, and DMA. …….. 88

Figure 2.8. The storage modulus as a function of frequency and temperature as determined by flat punch nanoindentation. ……..…….. 90

Figure 2.9. Superposition of the storage modulus to 22 ^{o}C. …… 91

Figure 2.10. Superposition of the storage modulus and the loss factor. ……... 92

Figure 2.11. The 4 term Prony series fit to *J*' versus radial frequency. ……..... 93

Figure 2.12. The creep compliance function as determined in uniaxial compression and by flat punch nanoindentation experiments performed in both the time and frequency domains. ……..…… 94

Figure 3.1. SEM image of the test structure, showing the thin film bridges and cantilevers on sample 3568 C3. …… 129

Figure 3.2. Schematic illustration of the Membrane Deflection Experiment (MDE). The support posts are assumed to be rigid and the film is modeled as a membrane (it does not support bending moments). …… 130

Figure 3.3. The load and stiffness as a function of deflection distance. The reversibility of the *S-h* data indicate the behavior is dominated by elasticity. The hysteretic *P-h* behavior is an experimental artifact due to thermal drift and the damping in the measurement system. ……..…..131

Figure 3.4. Film thickness measurements performed on the cantilever beams, a) samples 3568 C2 short, medium, and long, b) sample 3568 C3 short. ……... 132

Figure 3.5. *S* vs. *h*, taken on sample 3568 C3 short. The data clearly show the point of contact and illustrate the films behavior is dominated by elasticity, as the loading and unloading are quite repeatable. ...134

Figure 3.6. *S* vs. h^2, taken on 3568 C3 short. As the data show, the slope is relatively constant as a function of h^2, as predicted by the membrane model. ……..……..135

Figure 3.7. *S* vs. h^2 for the 8 measurements performed on the 3568 C2 short, medium, and long bridges. ……..……..136

Figure 3.A1. A free body diagram of the membrane deflection experiment. ..137

Introduction

This dissertation is a compilation of three journal articles: 1) "Nanoindentation and the dynamic characterization of viscoelastic solids", 2) "Measuring the constitutive behavior of viscoelastic solids in the time and frequency domain using flat punch nanoindentation", and 3) "Measuring the elastic modulus and residual stress of free-standing thin films using nanoindentation techniques". The first article was published in the *Journal of Physics D: Applied Physics*, the second will be submitted to a focus issue of the *Journal of Materials Research* covering indentation methods in advanced materials research, and the third will be submitted to *Acta Materialia*. In accordance with the dissertation guidelines set forth by the Graduate School of the University of Tennessee, each journal article is presented as an individual chapter in the dissertation. The references and figures for each article are presented at the end of each chapter.

The first and second articles focus on using nanoindentation to characterize the mechanical behavior of linear viscoelastic solids in the time and frequency domains. The third article utilizes nanoindentation techniques to characterize the elastic modulus and the residual stress of free-standing metallic thin films. Although the articles cover two different topics, they are related in that they present new experimental methods that can be used to investigate the elastic and viscoelastic properties of small volumes of material using nanoindentation techniques.

Over the past 20 years, nanoindentation has played an important role in characterizing the mechanical behavior of thin films and small volumes of material. The technique finds widespread application because of its high spatial resolution and its ability to determine mechanical properties without requiring an image of the residual impression; rather, the properties can be determined by modeling and analyzing the measured load-displacement response of the material or structure under investigation. In addition to measuring the hardness and elastic modulus, investigators have developed numerous other methods by which nanoindentation may also be employed to measure other plastic flow properties such as the yield strength, the work hardening exponent, and in some instances, the entire uniaxial stress-strain curve. Testing methodologies and models also exist to estimate the residual stress, fracture toughness, the stress exponent for creep, adhesion, and time dependent properties of viscoelastic solids such as the stress relaxation modulus, the creep compliance, and the complex modulus. However, it is important to recognize that many of the techniques proposed to measure these properties lack the experimental verification required to demonstrate their validity and identify their limitations. In many cases, the primary obstacle in modeling an indentation experiment is the complex state of stress and strain associated with the contact geometry. For example, even in the case of a bulk, homogeneous, isotropic, linear elastic solid, there is no closed form analytical solution to describe the state of stress or strain for an elastic-plastic contact.

The goal of this work is to provide experimental evidence that will help demonstrate the viability of dynamic nanoindentation as a characterization technique for viscoelastic solids and free-standing metallic thin films. In doing so, a strategy is established that can be used to ensure the accuracy and precision of dynamic nanoindentation measurements. These objectives are achieved by: 1) developing a thorough understanding of the key factors that control the design of robust experiments, 2) demonstrating how these factors can be incorporated experimentally, 3) presenting a direct comparison of the complex modulus and creep compliance function for a high damping thermoplastic as measured by nanoindentation, dynamic mechanical analysis, and uniaxial compression, and (4) directly comparing the elastic modulus for a well known reference material to the value estimated by the proposed nanoindentation technique.

Nanoindentation and the dynamic characterization of viscoelastic solids

E. G. Herbert[1], W. C. Oliver[1], and G. M. Pharr[2]

[1] University of Tennessee, Dept. of Materials Science and Engineering;

& MTS Nano Instruments Innovation Center

[2] University of Tennessee, Dept. of Materials Science and Engineering;

& Oak Ridge National Laboratory, Materials Science and Technology Division

Abstract

Using a high-damping thermoplastic as a standard reference material, the purpose of this work is to compare measured values of the complex modulus as determined by dynamic nanoindentation and dynamic mechanical analysis (DMA). Experiments were performed at approximately 22º C and 7 frequencies over the range of 1 to 50 Hz. The indentation measurements were performed using a 103 μm diameter flat punch and a newly developed test method that optimizes the accuracy and precision of the measured stiffness and damping. As determined by dynamic nanoindentation, values of the storage modulus and loss factor (tangent delta) ranged from 4.2 to 10.2 MPa, and 0.28 to 1.05, respectively. Over the range of 1 to 25 Hz, DMA confirmed the nanoindentation results to within 15% or better. Collectively, these data and the testing methods used to generate them should help future investigators make more accurate and precise measurements of the dynamic properties of viscoelastic solids using nanoindentation.

1. Introduction

The attractiveness of nanoindentation is its ability to characterize the mechanical behavior of small volumes of material with spatial resolutions in the nanometer to micrometer range. Over the past 20 years, the technique has been routinely used to investigate the linear elastic and plastic properties of thin films, modified surfaces, individual phases in alloys and composites, and other microscopic features and structures [1,2]. Attempts to characterize viscoelastic solids, on the other hand, have been far fewer in number, and additionally, most have focused on the strain-rate sensitivity and the transient properties of creep and stress relaxation [3-12]. Among the reasons for the large gap between dynamic elastic and dynamic viscoelastic indentation data in the open literature is the added complexity of performing meaningful experiments in the frequency domain. Loubet and Lucas were the first investigators to use dynamic nanoindentation to investigate the frequency response of polymers [13,14]. As they emphasized, accurate experimental techniques are entirely dependent on rigorous dynamic characterization of the measurement system itself. In addition, experimental data are most frequently modeled such to be representative of steady-state harmonic motion, a known contact geometry, and in many cases, linear viscoelasticity. Only under these conditions are the storage and loss modulus uniquely related to the transient functions from which the material parameters are derived, namely creep and stress relaxation.

Among the investigations that have used dynamic nanoindentation to measure the complex modulus, notable contributions have been made by Odegard and White [15-17]. In both cases, the investigators present a direct comparison of results generated by nanoindentation and dynamic mechanical analysis (DMA). This comparison is important because it provides a means of assessing the accuracy of the nanoindentation results, since DMA is regarded as the standard testing technique used by many modelers and designers. Odegard and White's results show good agreement between nanoindentation and DMA data for glassy, high modulus materials (E' ~1 GPa). In contrast, White's results on a rubbery, low modulus material (E' ~1 MPa) did not match as well; the nanoindentation results overestimated the DMA by nearly a factor of 2.

If nanoindentation is to become a viable characterization tool for the dynamic behavior of viscoelastic solids, a comparison between nanoindentation and DMA results like that of Odegard and White is needed to demonstrate the strengths and weaknesses of the technique. Additionally, meaningful comparisons must be supported by experimental verification of a steady-state harmonic response, a known contact geometry, and linear viscoelasticity. Seemingly simple choices like indenter geometry have an important impact on the ability to make meaningful measurements, as pyramids, spheres, and punches each have their own unique advantages and disadvantages. For example, recent work by Tweedie and Van Vliet [18] found that experiments performed with a pyramidal indenter on a number of polymer materials failed to generate a contact consistent

with the assumptions of linear viscoelasticity. Conversely, spheres used in the limit of small displacements relative to the radius of the tip were successful in generating data that accurately describes the linear viscoelasticity in these materials. The message from these investigations is that accurate experimental determination of the complex modulus by nanoindentation requires thoughtful experiments based on the general properties of the material and the choice of indenter geometry. Moreover, the cornerstone of the technique is a rigorous dynamic characterization of the measurement system itself.

The goal of this work is to provide experimental evidence that will help demonstrate the viability of dynamic nanoindentation as a characterization technique for viscoelastic solids. In doing so, a strategy will be established that may be used to ensure the accuracy and precision of dynamic nanoindentation measurements. These objectives are achieved by: 1) developing a thorough understanding of the key factors that control the design of robust experiments, 2) demonstrating how these factors can be incorporated experimentally, and 3) presenting a direct comparison of complex modulus measurements made on a high-damping thermoplastic using dynamic nanoindentation and DMA.

2. Theory

2.1. The dynamic response of a linear viscoelastic solid

For a linear viscoelastic material under sinusoidal loading, the stress-strain relationship may be expressed as

$$\sigma = \varepsilon_o E' \sin \omega t + \varepsilon_o E'' \cos \omega t \,, \tag{1}$$

where σ is the stress, ε_o is the strain amplitude, ω is the angular frequency, *t* is the time,

$$E' = \frac{\sigma_o}{\varepsilon_o} \cos \phi \,, \tag{2}$$

and

$$E'' = \frac{\sigma_o}{\varepsilon_o} \sin \phi \,, \tag{3}$$

where σ_o is the stress amplitude, and ϕ is the phase lag between the stress and the strain [19]. E' and E'' are, respectively, the storage and loss modulus. E' represents the material's capacity to store energy; it is the component in phase

with the applied displacement or load. E'' represents the materials capacity to dissipate energy; it is the component 90 degrees out of phase with the applied displacement or load. The ratio $\frac{E''}{E'} = \tan\phi$ is called the loss factor and is often used as a measure of damping in a linear viscoelastic material. Collectively, these frequency-dependent properties are used to characterize the viscoelastic response of a material.

It is often useful to analyze the mechanics of viscoelasticity by writing the stress-time and strain-time relationships in their complex forms:

$$\sigma = \sigma_o e^{i\omega t}, \tag{4}$$

and

$$\varepsilon = \varepsilon_o e^{i(\omega t+\phi)}. \tag{5}$$

Taking the ratio of stress to strain,

$$\frac{\sigma}{\varepsilon} = \frac{\sigma_o}{\varepsilon_o} e^{i\phi} = E^*, \tag{6}$$

where E^* is called the complex modulus, and in accordance with Euler's identity,

$$E^* = \frac{\sigma_o}{\varepsilon_o}\left(\cos\phi + i\sin\phi\right) = E' + iE''. \qquad (7)$$

One benefit of casting the relationship in this form is that it allows the complex harmonic motion to be graphically represented by a phasor diagram, which provides a simple interpretation of the relationship between E^*, E', E'', and ϕ. The phasor diagram is shown in Fig. 1.1a, where ϕ is an angle in the complex plane. E^* is the phasor, whose magnitude equals $\frac{\sigma_o}{\varepsilon_o}$, which is also equivalent to $\sqrt{E'^2 + E''^2}$ (note that figures and tables appear in appendices). In accordance with Eq. 7, the *x* and *y*-axes represent, respectively, the real (elastic stress) and imaginary (viscous stress) components of the complex modulus. The value of the phasor diagram here is that it helps provide physical insight in developing robust indentation experiments to measure the complex modulus of viscoelastic solids.

2.2. The dynamic response of a damped, forced oscillator – the test instrument

Fig. 1.2a shows a schematic illustration of the instrument used to perform the dynamic nanoindentation testing and its corresponding dynamic model. In response to a sinusoidally varying force, the differential equation which describes the motion of the system is

$$F_o e^{i\omega t} = m\ddot{h} + C\dot{h} + Kh\,, \tag{8}$$

where F_o is the amplitude of the load oscillation, m is the mass of the indenter, h is the displacement response, C is the damping coefficient of the instrument, and K is the stiffness of the support springs. Since Eq. 8 is nonhomogeneous, the general solution is the sum of a complimentary solution and a particular solution. The particular solution, which describes the steady-state motion of the system, is assumed to be

$$h(t) = h_o e^{i(\omega t - \phi)}, \tag{9}$$

where h_o is the amplitude of the displacement oscillation. Thus, the displacement oscillates at the same frequency as the applied force but potentially lags behind by the phase angle. By substituting the necessary time derivatives and simplifying Eq. 8, the real and imaginary components can be equated to solve for the magnitude of the dynamic compliance of the system,

$$\frac{h_o}{F_o} = \left[\left(\left(K - m\omega^2 \right)^2 + \omega^2 C^2 \right)^{1/2} \right]^{-1}. \tag{10}$$

Additionally, the phase angle between the applied load and the resulting displacement is given by

$$\tan\phi = \frac{C\omega}{K - m\omega^2}. \tag{11}$$

Using Eqs. 10 and 11, the dynamic stiffness, $K - m\omega^2$, and damping, $C\omega$, of the instrument are found to be

$$K - m\omega^2 = \frac{F_o}{h_o}\cos\phi, \tag{12}$$

and

$$C\omega = \frac{F_o}{h_o}\sin\phi. \tag{13}$$

Analogous to Fig. 1.1a, the dynamic response of a damped, forced oscillator may also be represented by a phasor diagram. Fig. 1.1b illustrates the instrument's frequency response in the complex plane and shows the relationships between $K - m\omega^2$, $C\omega$, ϕ, and $\frac{F_o}{h_o}$. As shown in the figure, $\frac{F_o}{h_o}$ is the magnitude of the phasor representing the frequency response of the instrument and ϕ is an angle in the complex plane. The *x* and *y*-axes represent the real (stiffness) and imaginary (damping) components of the displacement response of the system. Although the axes in Figs. 1.1a and b are fundamentally different, they are uniquely related through the geometry of the contact.

2.3. Determining E' and E'' in a dynamic nanoindentation experiment

For a load controlled testing system, the force amplitude is set and the resulting displacement amplitude and phase angle are measured. When the indenter and sample, which are coupled through the geometry of the contact, undergo steady state harmonic motion, the measured stiffness (Eq. 12) and damping (Eq. 13) represent the combined frequency response of the instrument and the sample. The dynamic stiffness and damping of the contact (i.e., material response and parameters) are determined by subtracting out the instrument's contribution to the total measured response. It is important to note, however, only in the limit that the additional moving mass of the sample is small in comparison to the mass of the column do the $m\omega^2$ terms cancel. In other words, the inertial contribution of the sample is assumed to be negligible in comparison to the testing system. In the limit of linear viscoelasticity, the elastic-viscoelastic correspondence principle is deemed valid and thus Sneddon's stiffness equation, the fundamental equation of nanoindentation, may be used to relate the dynamic stiffness and damping of the contact to E' and E'' [20],

$$\frac{E'}{1-\nu^2} = \frac{F_o}{h_o}\cos\phi\,\frac{\sqrt{\pi}}{2}\,\frac{1}{\beta}\,\frac{1}{\sqrt{A}}, \tag{14}$$

and

$$\frac{E''}{1-\nu^2} = \frac{F_o}{h_o}\sin\phi\frac{\sqrt{\pi}}{2}\frac{1}{\beta}\frac{1}{\sqrt{A}}, \tag{15}$$

where ν is Poisson's ratio, β is a term related to the geometry of the contact and *A* is the projected contact area. β = 1 for a circular contact (circular flat punch, sphere, and cone), β = 1.034 for a Berkovich [21]. While Poisson's ratio is physically capable of exhibiting time dependent behavior, it was assumed to be a constant value of 0.3 for all of the nanoindentation and DMA data analysis presented in this work.

The phasor diagram in Fig. 1.1c can now be used to explain the coupled dynamic response of the sample and the testing system. As previously explained, the frequency response of the instrument is controlled by the magnitude of the moving mass, the stiffness of the support springs, and the damping in the head. For a given instrument, these parameters are essentially fixed. The frequency response of the sample is controlled by $E'(\omega)$, $E''(\omega)$ and the geometry of the contact. $E'(\omega)$ and $E''(\omega)$ are fixed for a given material and frequency, and the geometry of the contact can be controlled by using a flat punch indenter. As such, control of the contact geometry is the means by which robust experiments can be designed so that the sample dominates the measured response. In working with constraints such as the available volume of material and microstructure, however, this criterion is not always simple to achieve. Thus, when the instrument's contribution comprises a significant fraction the combined

response, it is imperative to know the dynamic stiffness and damping of the instrument as accurately and precisely as possible, since the accuracy of the experimental measurements then relies on isolating small changes in potentially large numbers. As dictated by many applications, this is frequently the condition under which many experiments are performed, i.e., thin films and small volumes of material.

2.3.1. Modeling the sample

The dynamic behavior of viscoelastic solids is most frequently modeled using combinations of linear springs and linear dashpots. The various groupings of springs and dashpots are used to establish the differential equations which describe the materials response to an applied load or displacement. At one end of the spectrum, the Voigt model, a spring and dashpot in parallel, offers the simplest means of describing viscoelastic behavior, as its response to a sinusoidal input is a sinusoidal output with a phase lag. At the other end of the spectrum, models incorporating more complex assemblages of springs and dashpots may be used to capture more complex material behavior as a function of frequency. All these models are phenomenological in nature and based on the assumption of linear viscoelasticity. This condition is valid only in the limit of small strains, loosely defined as strains less than 1%.

In this work, the sample was chosen to be modeled as a Voigt solid, as indicated by the “contact” in Fig. 1.2b (the contact and the instrument are arranged in parallel because they necessarily experience the same change in displacement). This model captures the essence of viscoelastic behavior and is simple to implement. However, because this model only has the means of incorporating a single relaxation time, it is limited to modeling material behavior at a single frequency. Furthermore, it has no means of accounting for instantaneous elasticity. While more complex models offer a means to overcome these limitations, experimental evidence is needed to determine the extent of the improvements and the ability to predict the frequency dependence. The recent work of Wright et al. [22] explores this issue, and develops the rigorous mathematics required to incorporate an additional spring into the Voigt model to allow for instantaneous elasticity.

3. Experimental measurements

The storage and loss moduli, E' and E'', were measured on a bulk sample of a highly plasticized polyvinyl chloride (PVC), which is a high-damping thermoplastic. The experiments were conducted at frequencies of 1, 3, 5, 10, 20, 30, and 50 Hz. Both the indentation and DMA samples were taken from the exact same sheet of material. The indentation sample measured 8.2 mm long, 6.8 mm wide, and 7 mm thick. The precision-machined DMA sample was

approximately 35 mm long, 15 mm wide, and 5 mm thick. Every effort was made to ensure uniformity in the thickness of the sample, since E' is proportional to the thickness cubed ($E' \alpha t^3$). All of the experiments were conducted at approximately 22 ºC, which is well above the sample's glass transition temperature of -17.2 ºC. For the indentation experiments, the air temperature in the lab was controlled to within $\pm$ 1º C using a constant reheat system. The air temperature near the surface of the sample was measured using a precision thermometer. For the DMA experiments, the air temperature was controlled using a liquid nitrogen gas cooling system provided by the instrument manufacturer, TA Instruments.

The nanoindentation experiments were performed on MTS' NanoIndenter® XP using a 103 µm diameter diamond flat punch in conjunction with a 50 nm oscillation amplitude and the continuous stiffness measurement (CSM) technique. Details of the CSM technique have been described previously [1]. The DMA experiments were performed using TA Instruments' model Q800 and the dual cantilever sample mount, which clamps the sample at both ends. The instrument was completely calibrated in accordance with the procedures provided by TA Instruments. Using polycarbonate as a standard reference material, the measured E' at 1 Hz and room temperature was 2349 MPa, which compares well with the literature value of 2350 MPa. Measurements performed on the PVC at 1 Hz with amplitudes of 20, 40, and 60 µm generated data consistent with the assumptions of linear viscoelasticity, as the change in

amplitude had virtually no impact on the measured E'. As a result, the oscillation amplitude was chosen to be 20 μm for all DMA experiments performed on the PVC. In addition, the experiments incorporated a thermal soak period of 1 hour. All of the averaged nanoindentation and DMA data are presented with error bars spanning one standard deviation about the mean.

The diameter of the flat punch was chosen by design. As previously discussed, important considerations in choosing the tip geometry are: 1) the desire to achieve dynamic stiffness and damping measurements that are dominated by the response of the sample, and 2) the microstructure of the sample and the available volume of material. The reference material selected for this work is a commercially available, high-damping thermoplastic in bulk form. The material is amorphous and devoid of crosslinking; therefore even small volumes of the material are representative of the bulk microstructure. Using Eq. 12 and assuming E' at 1 Hz is on the order of 1 to 10 MPa, β = 1, and the flat punch has a radius of 50 μm, the resulting contact stiffness is 100 to 1000 N/m, which is approximately 1 to 10 times larger than the stiffness of the instrument's support springs. The fact that the instrument stiffness is actually less than that of the contact places limits on the accuracy with which specimen properties can be measured. Clearly, as the disparity between the stiffness of the instrument and the stiffness of the contact decreases, the more important it becomes to precisely know the stiffness of the instrument in order to accurately isolate the material's

response. The same is also true for the damping of the contact in comparison to the damping of the instrument.

3.1. Instrument characterization

Regardless of the type of instrumentation, accurate and precise measurements of E' and E'' are critically dependent on the ability to correctly measure and model the frequency response of the test equipment. While the characterization techniques discussed in this section are specific to the instrument used in this study the general concepts are applicable to all types of instrumentation, regardless of the manufacturer.

Fig. 1.2a shows a schematic illustration of the head design of the instrument and the simple harmonic oscillator model used to predict its frequency response. For the purposes of this discussion, it is important to note the following features: the load is controlled by electromagnetic actuation, the displacement is measured using the parallel plate capacitive gauge, and the indenter column is supported by two leaf springs with a vertical stiffness of approximately 100 N/m and a lateral stiffness of approximately 10,000 N/m. Among the most important aspects of the head design is that the lateral stiffness of the support springs effectively limits the system to only 1 degree of freedom, i.e., vertical motion. This physical limit is imperative in order for the oscillator model to be an accurate reflection of the physical motion of the indenter. However, because the

remaining degrees of freedom each have their own frequency response, there will be a cutoff frequency above which cross-talk and/or phase rotations caused by other modes of vibration effectively prevent accurate instrument characterization. Thus, accurate measurements can only be made below the cutoff frequency. Also, of significant importance is knowledge that eddy currents in the voice coil as well as moving air through the 2 mm gap of the capacitance gauge generate sufficient damping such that the instrument is over critically damped. In addition to being dependent on frequency, the dynamic stiffness and damping of the instrument are also a function of the physical location of the center plate relative to its full range of travel in the capacitance gauge. To simplify further discussion of this positional dependence, the center plate's position in the gap is called the raw displacement and the center of the gap is taken to be the zero datum (0 nm). Generally speaking, it is good experimental practice to mount the samples in the instrument such that the raw displacement at the surface of the sample is within ± 100,000 nm of 0 nm. This range in the capacitance gauge corresponds to nearly constant stiffness and damping at a given frequency. Complete dynamic characterization of the instrument consists of measuring the reference phase angle as a function of frequency, and measuring the stiffness and damping as a function of frequency and raw displacement.

3.1.1. Determining the cutoff frequency

Because other modes of vibration come into play at high frequencies, cross-talk and/or phase rotations can affect the frequency response of the instrument in a manner that is not described or accounted for in the simple 1 dimensional oscillator model shown in Fig. 1.2a. As a result, this additional motion makes it impossible to accurately determine the dynamic stiffness and damping of the instrument. Therefore, this cutoff frequency must be experimentally identified and not exceeded in any characterization work. One way to identify the cutoff is to measure the phase angle as a function of frequency with the indenter free hanging in space. Fig. 1.3a shows the phase angle as a function of frequency for the indentation system used in this work. The smooth region of the curve, from 1 to 50 Hz, indicates frequencies consistent with the 1 dimensional oscillator model. The discontinuity at 53 Hz indicates the cutoff frequency, beyond which cross-talk and/or phase rotations from other modes of vibration contribute to the measured response in a manner that is not modeled. Therefore, accurate characterization of the instrumentation, and hence the complex modulus of the sample, can be made only over the frequency range of approximately 1 to 50 Hz.

3.1.2. Measuring the reference phase angle

The dynamic measurements performed with the CSM technique are carried out using a frequency-specific phase-lock amplifier or PLA. As the command signal for the harmonic load travels through filters in the PLA, a phase shift that varies almost linearly as a function of frequency is introduced. During an experiment, accurate measurement of the phase angle between the applied harmonic load and the resulting harmonic displacement therefore depends on correcting the measured phase angle for the filter-induced phase shift.

Applying a large load (3 mN) oscillation to reduce the signal to noise ratio, the phase angle between the applied load and the load leaving the PLA is easily measured as a function of frequency. Fig. 1.3b shows the average of 15 measurements of this reference phase angle over the range of 1 to 50 Hz. The error bars span one standard deviation about the mean. The reference phase angle is used to correctly configure the PLA at each frequency during the experiment.

3.1.3. Measuring the dynamic stiffness and damping of the testing system

In order to maximize the accuracy of the measured E' and E'', it is necessary that the instrument and sample characterization be performed at or near the

same raw displacement, since the stiffness and damping of the instrument are a function of position, particularly towards the extreme ends of travel. Thus, in terms of the chronological flow of the experiment, the dynamic stiffness and damping can only be measured after determining the approximate raw displacement at which the sample characterization will subsequently take place. A number of factors affect the determination of the appropriate raw displacement to perform the sample characterization, as it depends on the choice of indenter geometry and ultimately, the necessity to generate a contact representative of linear viscoelasticity. These factors will be discussed in detail in section 3.2.

With the indenter tip hanging in free space and positioned at the approximate raw displacement at which the sample characterization will take place, the stiffness and damping of the instrument are measured as a function of frequency using Eq.'s 12 and 13. Clearly, these measurements must be performed with the PLA correctly configured with the previously measured reference phase angles. Fig. 1.4 shows the measured stiffness and damping of the testing system at each frequency that will be used to characterize the sample. These data represent the average of 15 measurements. The error bars span one standard deviation about the mean. Among the notable features in these data are the excellent reproducibility, and beyond resonance (14.3 Hz), the rapid increase in the magnitude of the dynamic stiffness. Consistent with the oscillator model and the phasor diagram in Fig. 1.1b, the dynamic stiffness goes to zero and the phase

angle goes to 90º at the resonant frequency. Beyond resonance, the dynamic stiffness is negative because the phase angle is in excess of 90º.

The data presented in Fig. 1.4 may also be used to experimentally confirm the validity of the assumed dynamic model of the instrument (Fig. 1.2a). Assuming the model is an accurate description of the physical motion of the system, then adding $m\omega^2$ to both sides of Eq. 12 and dividing both sides of Eq. 13 by ω will produce constant values as a function of frequency for both the support spring stiffness K_s and the damping coefficient C. Using the data acquired at 1 and 50 Hz in conjunction with Eq. 12, the mass was found to be 12.14 g. For each of the 7 frequencies, adding the $m\omega^2$ term back into the stiffness and dividing the damping by ω led to an average stiffness of 98 N/m ± 4.9% and an average damping coefficient of 2.9 Ns/m ± 2.5%. The fact that these values are relatively constant as a function of frequency clearly demonstrates that the simple harmonic oscillator accurately describes the physical motion of the system.

3.2. Measurement of the complex modulus by dynamic nanoindentation

In order to accurately measure E' and E'', the dynamic indentation experiment must achieve steady state harmonic motion while the instrument and sample are coupled through a known contact geometry. In addition, the resulting stress and strain must be representative of linear viscoelasticity. Once the tip geometry has

been chosen, these three criteria shape the design of the indentation experiment. As such, the purpose of this section is to develop an indentation test method that optimizes the accuracy and precision of the measured E' and E''. The results presented in this section were calculated in accordance with the procedure outlined in section 2.3.

3.2.1. Determining full contact with the flat punch

Among the reasons for choosing the flat punch indenter geometry are: 1) it effectively eliminates uncertainty in the contact area, and 2) it avoids the problem of achieving steady-state harmonic motion in the presence of transient behavior. However, the flat punch is not without its drawbacks, the most significant of which is that the punch cannot be mounted perfectly normal to the test surface. There is always a small angle between the face of the punch and the surface of the sample. As a result, the test method must have a robust means of identifying the point at which the face of the punch is brought in full contact with the surface of the sample. In addition, the punch geometry also creates a stress concentration along the circumference of the contact. It is assumed that the contribution of the stress concentration to the measured dynamic stiffness and damping is negligible. However, this has not been confirmed experimentally.

Fig. 1.5 presents data from a single experiment and shows the harmonic displacement and phase angle as a function of raw displacement. For the sake of clarity, only 5% of the data are plotted. Both the harmonic displacement and phase angle can be used as a reliable indicator of the point of contact, since the drop in both signals occurs precisely when the punch makes contact with the surface of the sample. The criterion for full contact between the face of the punch and surface of the sample is thus based on the harmonic displacement and its establishment of a stable, constant value.

3.2.2. Generating steady-state harmonic motion

A fundamental assumption in modeling the combined dynamic response of the instrument and sample (Fig. 1.2b) is that of a steady-state harmonic response. In order for the model to be an accurate reflection of the physical experiment, transient behavior must be given enough time to dissipate such that its effect on the dynamic response is negligible. For example, in a load-amplitude controlled experiment performed with a pointed indenter or sphere, creep behavior will cause the contact area to increase with time which in turn will cause the displacement amplitude to decrease until the creep transient dissipates. Only once the transient is removed is the model presented in Fig. 1.2b an accurate reflection of the experiment.

A distinct advantage of the flat punch geometry is that even in the presence of creep behavior, the contact area cannot change, and hence, neither can the amplitude of the oscillation. However, if the creep rate is large enough, it is possible that the additional strain in the vicinity of the contact may be enough to violate the small strain assumption of linear viscoelasticity. This undesirable affect of creep may be easily avoided by monitoring the creep rate, while at the same time, periodically returning the indenter to the raw displacement corresponding to full contact. Until the measured creep rate falls below a specified level, the experiment continues to measure the creep rate and then return to the raw displacement at full contact. In this way, the raw displacement is maintained at the target position and the transient behavior is given enough time to effectively dissipate.

Illustrating data from one experiment on the PVC, Fig. 1.6 shows the raw displacement and the RMS displacement amplitude as a function of time and frequency. The change in the raw displacement with time is due to creep. The increase in penetration depth over the duration of the experiment is approximately 490 nm. Despite this creep behavior, the contact area is constant and hence the displacement amplitude is constant with time as well, as shown in the figure. It is important to note that the displacement oscillation is driven by a different, but constant force oscillation at each frequency. Because the force and displacement amplitude are both constant with time at each frequency, steady-state behavior is achieved.

3.2.3. Determining the linear viscoelastic regime

In order to make a meaningful comparison between the DMA and nanoindentation test results, determination of E' and E'' requires data representative of linear viscoelasticity. By definition, this means that an increase in the applied load or displacement amplitude has no affect on the measured E' and E''. Therefore, only in the regime where the measured properties are constant as a function of static pre-compression (an increase in the applied load) and oscillation amplitude is the condition of linear viscoelasticity valid.

Fig. 1.7 shows E' and the loss factor as a function of frequency and static pre-compression. The oscillation amplitude was nominally 50 nm for all 5 compression distances. Because tan ϕ is considered the fundamental measure of damping in a linear material, the remaining test results will be presented in terms of E' and the loss factor. The data in Fig. 1.7 represent an average of 15 measurements, and the error bars span one standard deviation about the mean. For the sake of clarity, the loss factor is represented by the individual lines for each compression distance, but only one set of data markers are plotted. These results clearly show that compressing the sample up to an additional 5 µm beyond the point of full contact has no measurable affect on E'. However, between 5 and 10 microns of compression, the measured E' begins to increase. Presumably, the increase is due to the additional static strain, thereby violating the small strain assumption of linear viscoelasticity. However, it is also possible

that the surface of the sample has made partial contact with the sides of the punch. The fact that there is little to no measurable change in the loss factor, indicates that E'' mirrors the change in E'. The picture that emerges is that additional static strain in the vicinity of the contact produces a proportional increase in the materials ability to store and dissipate energy such that there is no measurable change in the material's internal friction.

Fig. 1.8 shows E' and the loss factor as a function of frequency and oscillation amplitude. The compression distance is 3 μm beyond the point of full contact. The data represent an average of 15 measurements and the error bars span one standard deviation about the mean. These data clearly show that ranging the oscillation amplitude from 50 to 3000 nm has no measurable affect on the components of the complex modulus. Collectively, the experimental observations presented in Figs. 1.7 and 1.8 indicate that compressing the sample an additional 3 μm past the point of full contact and using a 50 nm oscillation amplitude results in data which are well within the limits of linear viscoelasticity.

3.2.4. Comparing nanoindentation and DMA results

Fig. 1.9 presents a direct comparison of E' and the loss factor of highly plasticized PVC (a bulk, high-damping thermoplastic) as determined by nanoindentation and DMA at 22º C. Both the nanoindentation and DMA data

represent the average of 15 measurements and the error bars span one standard deviation about the mean. Clearly, the two techniques produce similar results over the range of 1 to 25 Hz. At 1 Hz, where the disparity in E' is greatest, the difference between the two techniques is still within 15%. Between 30 and 35 Hz, the DMA data unexpectedly break from the smooth curve for unknown reasons. Conversely, over the full frequency range of 1 to 50 Hz, the nanoindentation data give a smooth curve that is consistent with expectations for the behavior of a bulk, isotropic, homogeneous viscoelastic solid well above its glass transition temperature. While the nature of the discrepancy in the DMA data is unknown, it is important to recall that the instrument was completely calibrated in accordance with the procedure provided by TA Instruments. Nevertheless, in comparing the nanoindentation and DMA data, the clear message is the two characterization techniques produce very nearly the same results.

4. Summary and conclusions

The data presented in this work demonstrate the ability of nanoindentation to accurately and precisely measure the complex modulus of linear viscoelastic solids. Successful application of the technique requires rigorous characterization of the frequency response of the measurement system itself. For the measurement system used in this study, the crucial parameters are the reference

phase angle of the phase lock amplifier and the dynamic stiffness and damping of the instrument, both of which depend on the frequency of the measurement and the position of the center plate in the capacitance gauge. Because of cross-talk and/or phase rotations, there is a cutoff frequency above which the instrument's frequency response cannot be accurately modeled. This cutoff frequency must be experimentally determined and not exceeded in any measurements. In order to confirm the accuracy of the nanoindentation test results, experimental verification should be provided to prove the data are representative of steady state harmonic motion, a known contact geometry, and linear viscoelasticity. Only under these conditions are the measured storage and loss modulus uniquely related to the transient functions from which they are derived, namely creep and stress relaxation.

Acknowledgements

The authors are particularly grateful for the input of Kermit Parks and Lee Spencer of the MTS Nano Instruments Innovation Center and Dr. Mark Dadmun of the University of Tennessee. Tom Malmgren, also of UT, provided outstanding support in performing the DMA experiments.

References

[1] W. C. Oliver and G. M. Pharr, J. Mater. Res. **19** 1 (2004) 3.

[2] J. L. Hay, G. M. Pharr, ASM Handbook **8** (2000) 232.

[3] M. R. VanLandingham, J. Res. Natl. Inst. Stand. Technol. **108** 4 (2003) 249.

[4] L. Cheng, X. Xia, W. Yu, L. E. Scriven, W. W. Gerberich, J. Polym. Sci.: Part B: Polym. Phys. **38** (2001) 10.

[5] P. –L. Larrson, S. Carlsson, Polym. Test. **17** (1998) 49.

[6] S. Shimizu, T. Yanagimoto, M. Sakai, J. Mater. Res. **14** 10 (1999) 4075.

[7] M. Sakai, Phil. Mag. **A82** 10 (2002) 1841.

[8] M. L. Oyen, R. F. Cook, J. Mater. Res. **18** 1 (2003) 139.

[9] J. L. Bucaille, E. Felder, G. Hochstetter, J. Mater. Sci. **37** (2002) 3999.

[10] T. C. Ovaert, B. R. Kim, J. Wang, Prog. Org. Coat. **47** (2003) 312.

[11] N. Huber, E. Tyulyukovskiy, J. Mater. Res. **19** (2004) 101.

[12] Y. -T. Cheng, W. Ni, C.-M. Cheng, J. Mater. Res. **20** 11 (2005) 3061.

[13] J. -L. Loubet, B. N. Lucas, W. C. Oliver, NIST Special Publication **896** (1995) 31.

[14] B. N. Lucas, Ph. D. Dissertation, The University of Tennessee, Knoxville (1997).

[15] Y. -T. Cheng, W. Ni, C.-M. Cheng, Phys. Rev. Let. **97** 7 (2006) 075506.

[16] G. M. Odegard, T. S. Gates, H. M. Herring, Exp. Mech. **45** 2 (2005) 130.

[17] C. C. White, P. L. Drzal, M. R. VanLandingham, Mater. Res. Soc. Symp. Proc. **841** (2005) R5.3.

[18] C. A. Tweedie, K. J. Van Vliet, J. Mater. Res. **21** (2006) 1576.

[19] R. S. Lakes, Viscoelastic Solids, CRC Press (1999) 63.

[20] I. N. Sneddon, Int. J. Eng. Sci. **3** (1965) 47.

[21] R. B. King, Int. Journal Solids Struct. **23** (1987) 1657.

[22] W. J. Wright, A. R. Maloney, and W. D. Nix, Int. J. Surface Science and Engineering, **1** 2/3 (2007) 274.

Appendix 1.1.

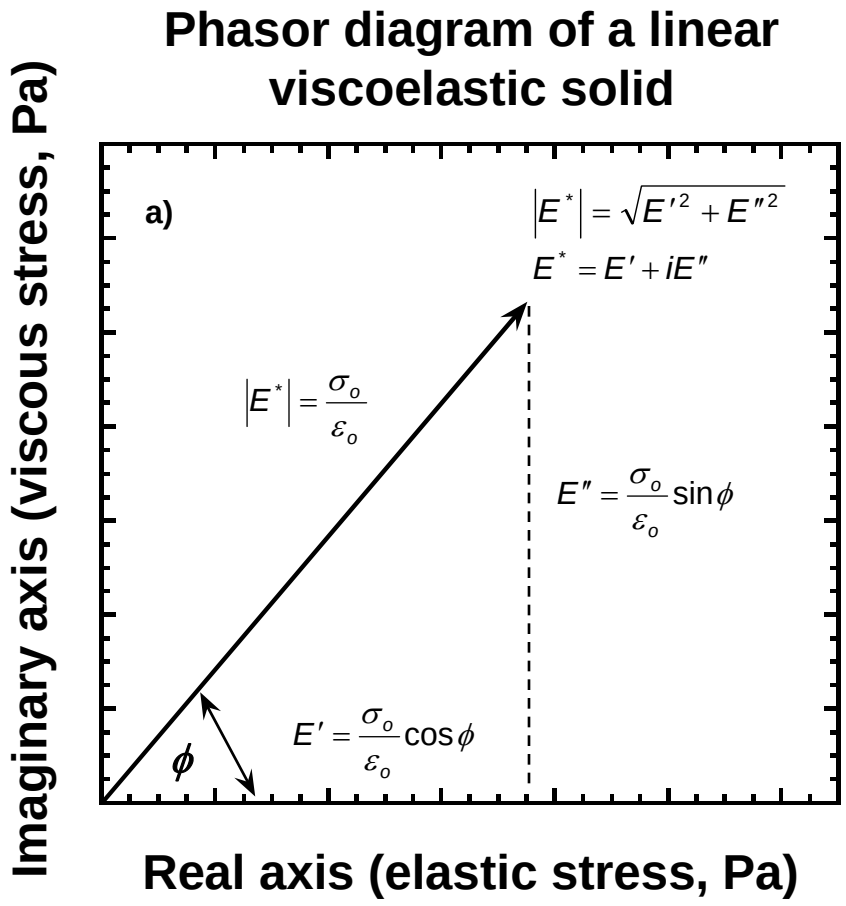


Figure 1.1. Schematic illustrations showing the imaginary and real components of a) the complex modulus of a linear viscoelastic solid subject to sinusoidal loading, b) the frequency response of a damped, forced oscillator, and c) the combined frequency response of a viscoelastic solid (sample) and a damped, forced oscillator (instrument).

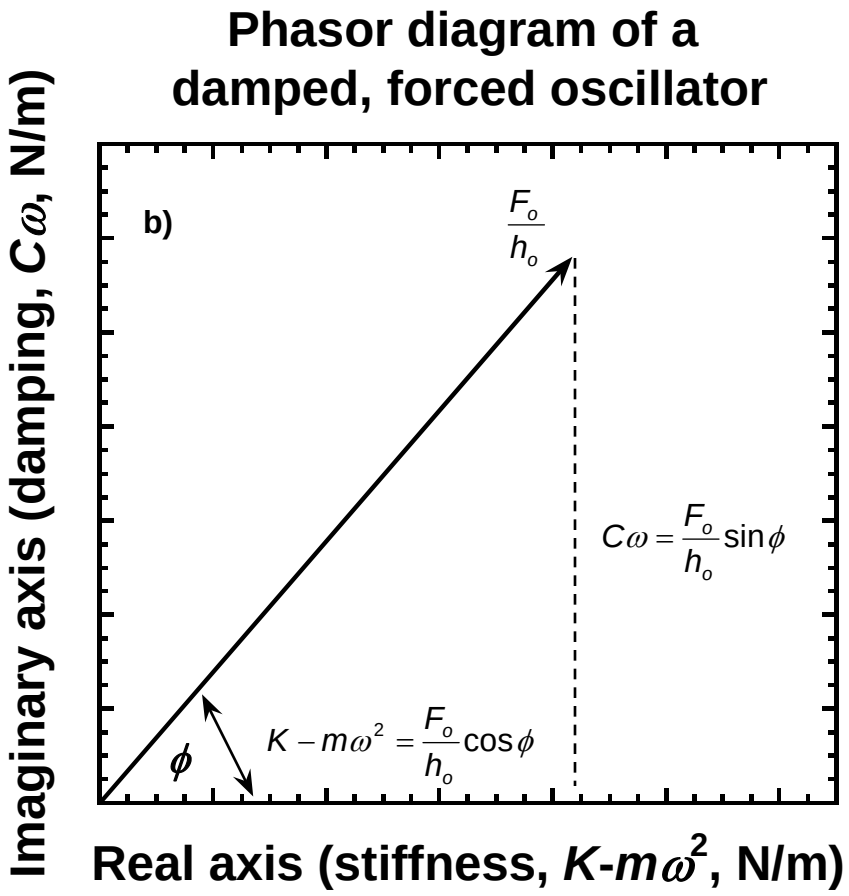


Figure 1.1 continued.

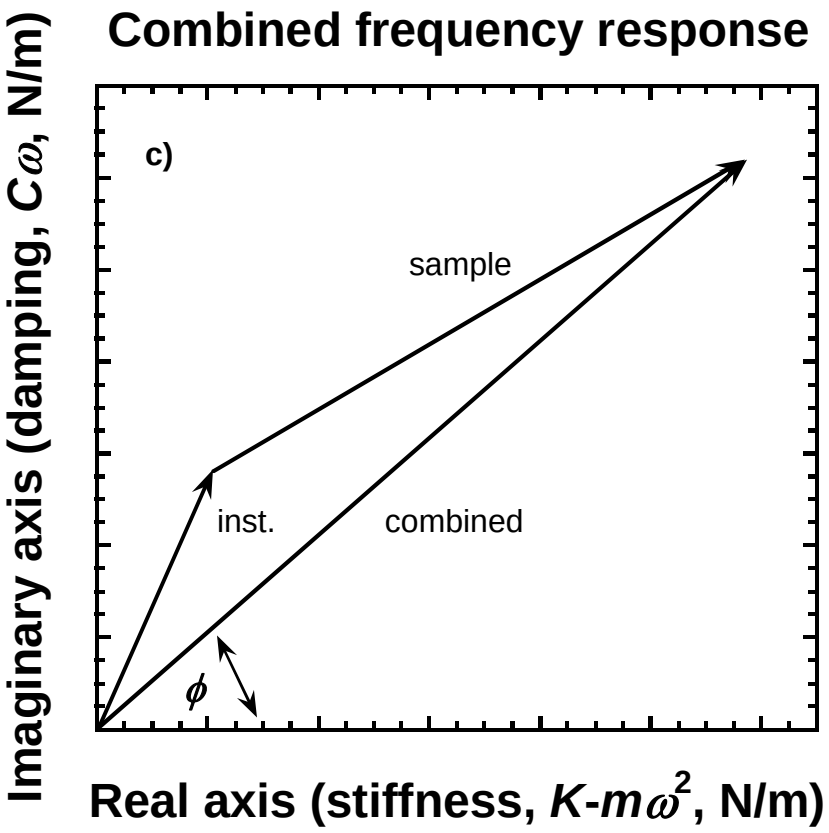


Figure 1.1 continued.

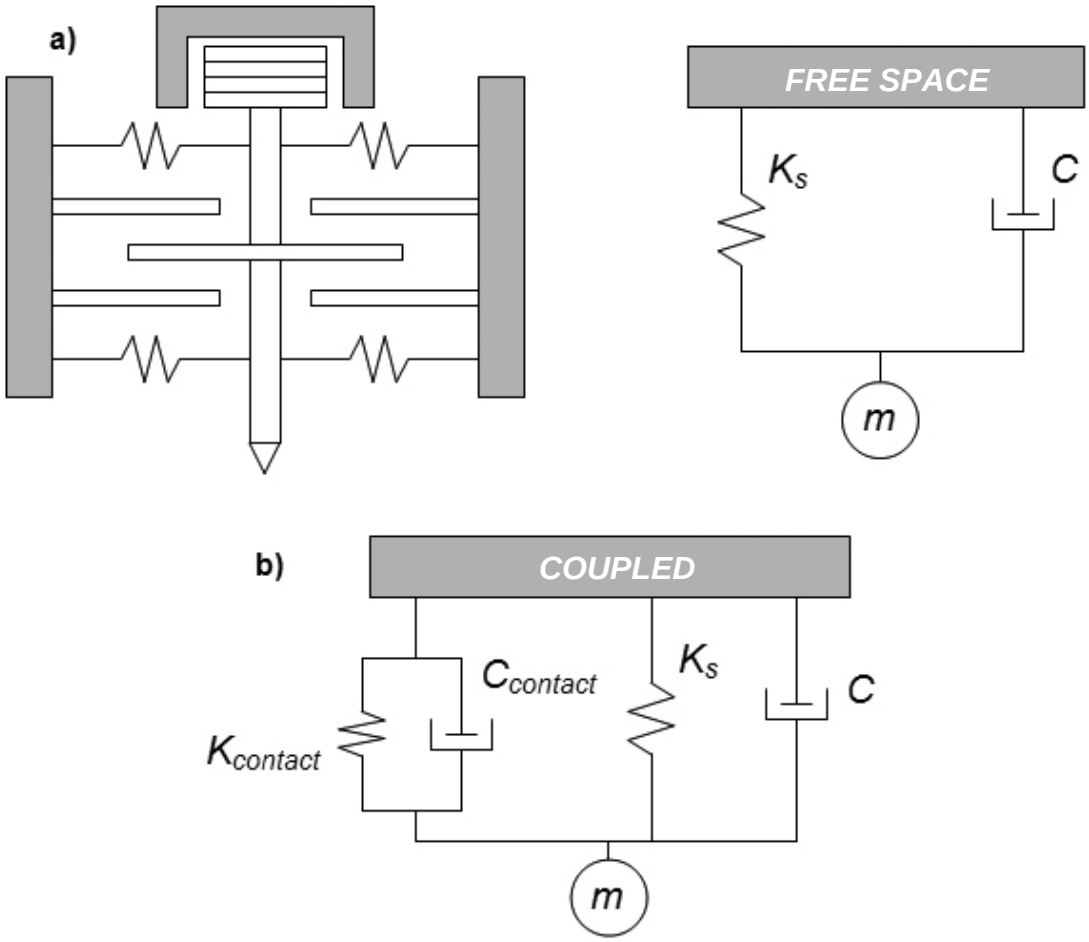


Figure 1.2. a) A schematic illustration of the testing system and the dynamic model used to describe the behavior of the system as a function of frequency. b) The dynamic model used to describe the combined frequency response of the instrument and sample. Throughout this work, the load frame is assumed to be rigid relative to the stiffness of the support springs, K_s.

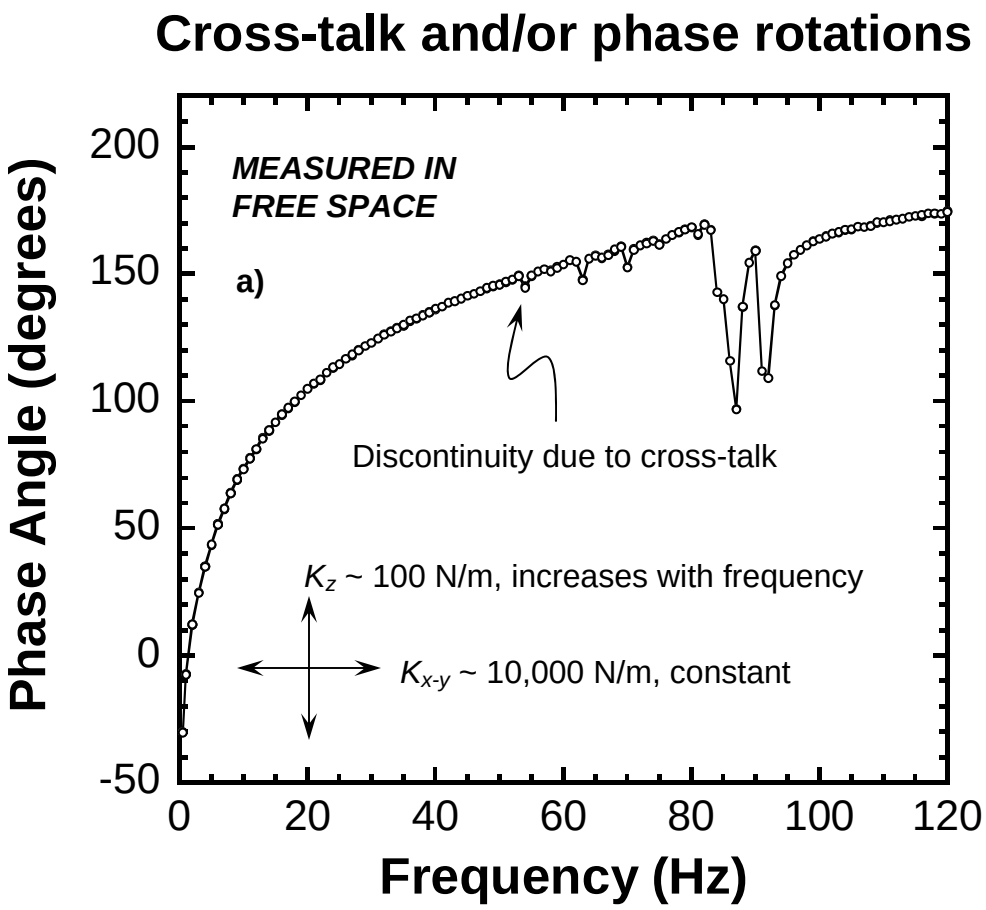


Figure 1.3. a) The phase angle as a function of frequency, measured in increments of 1 Hz with the indenter column hanging in free space. The discontinuity at 53 Hz indicates the point at which the difference in stiffness between the *z* and *x-y* plane is no longer large enough to prevent cross-talk. b) The reference phase angle as a function of frequency, measured with the indenter column hanging in free space and at the same frequencies to be used in characterizing the sample.

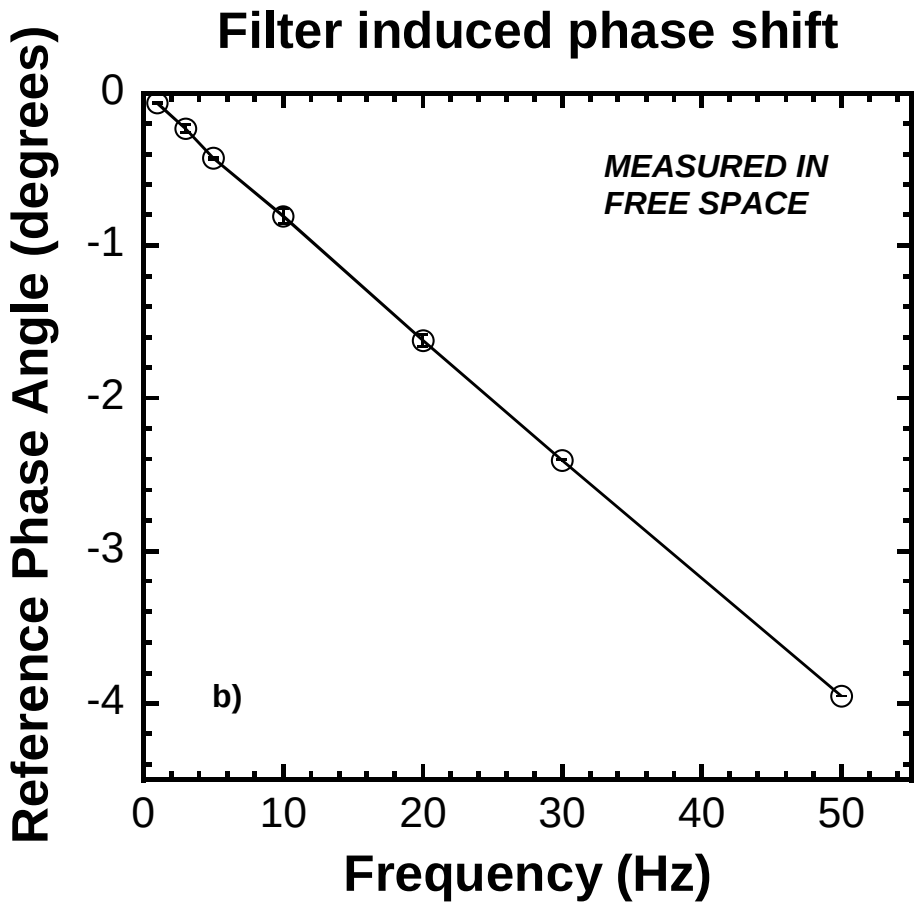


Figure 1.3 continued.

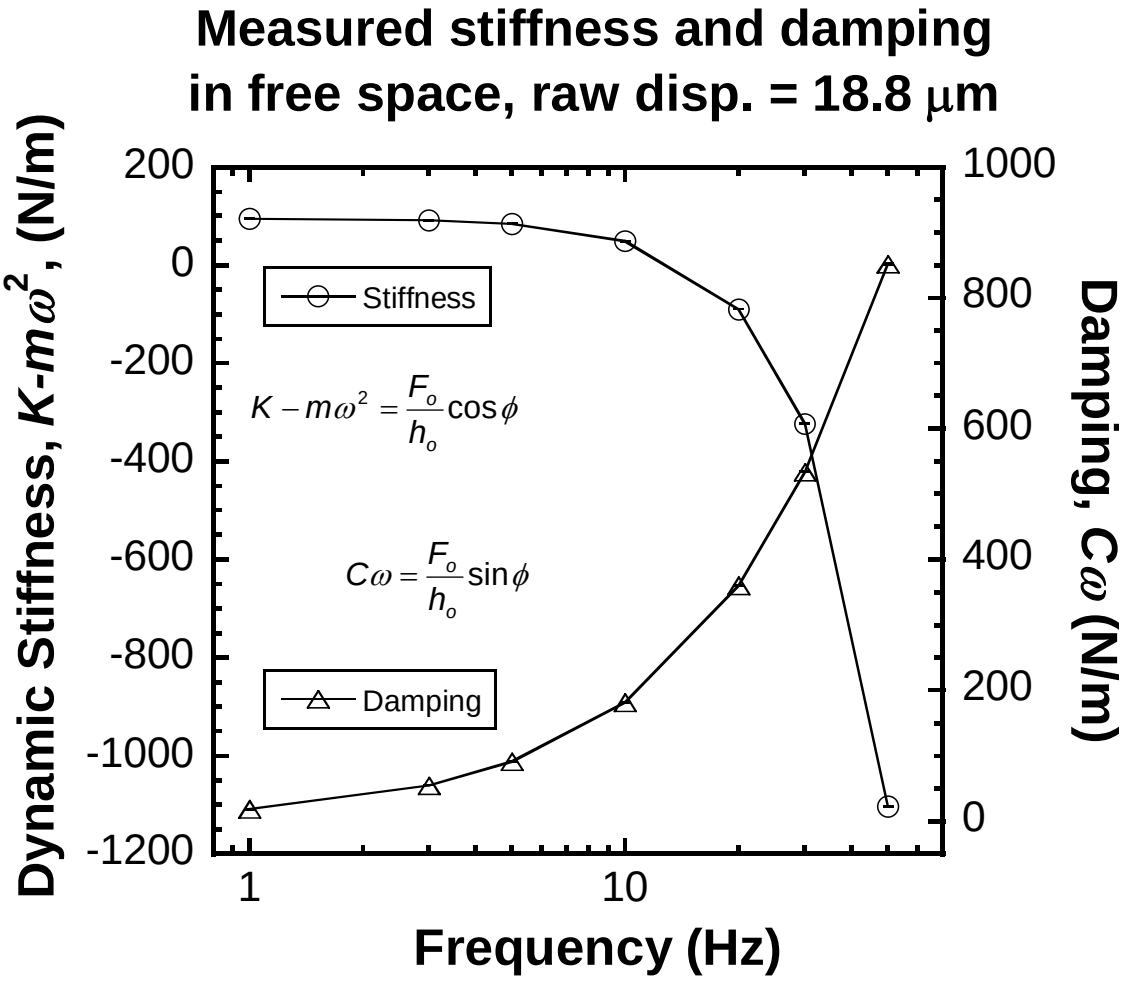


Figure 1.4. The dynamic stiffness and damping of the testing system as a function of frequency, measured with the indenter column hanging in free space and at the same frequencies to be used in characterizing the sample. The indenter is positioned at the raw displacement (position in the capacitance gauge) that corresponds to full contact.

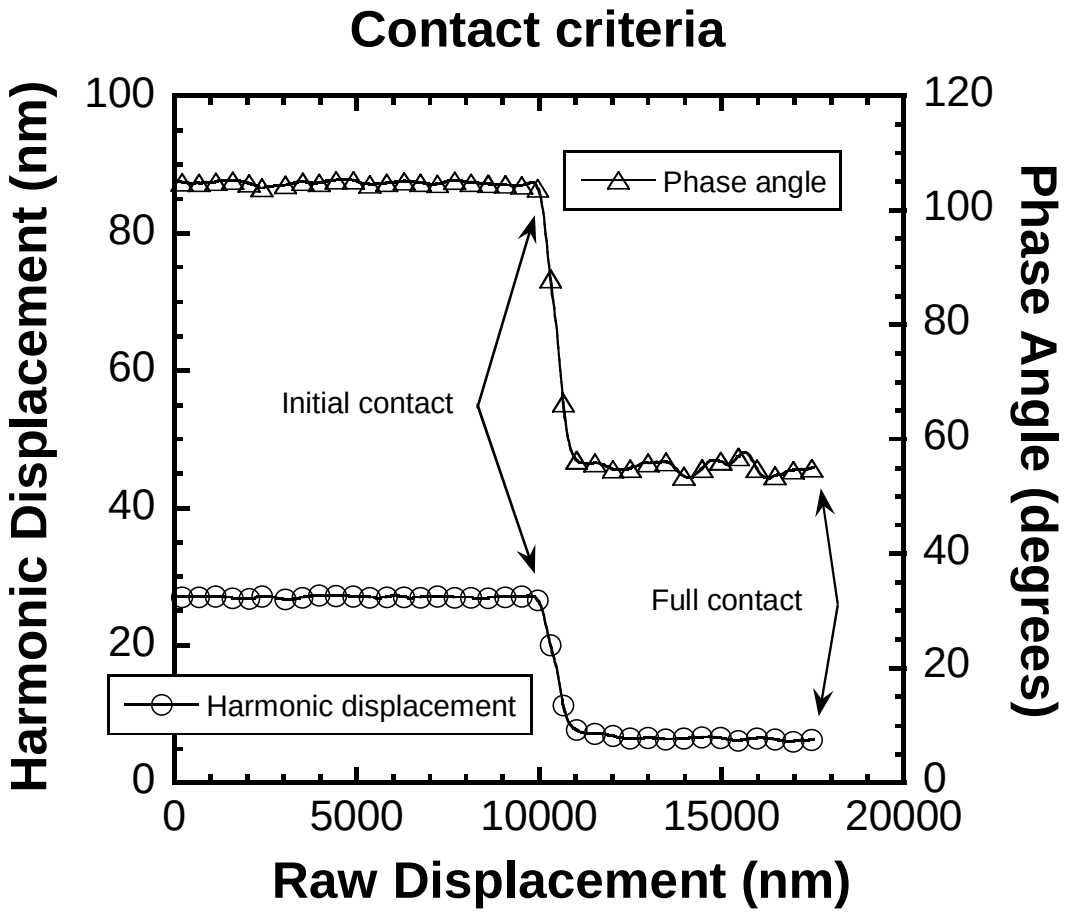


Figure 1.5. The harmonic displacement and phase angle as a function of raw displacement. These data are used to determine the raw displacement at both the point of initial contact and full contact between the face of the punch and the surface of the sample. The criterion for initial contact is a specified change in the phase angle. The criterion for full contact is a specified time rate of change in the harmonic displacement.

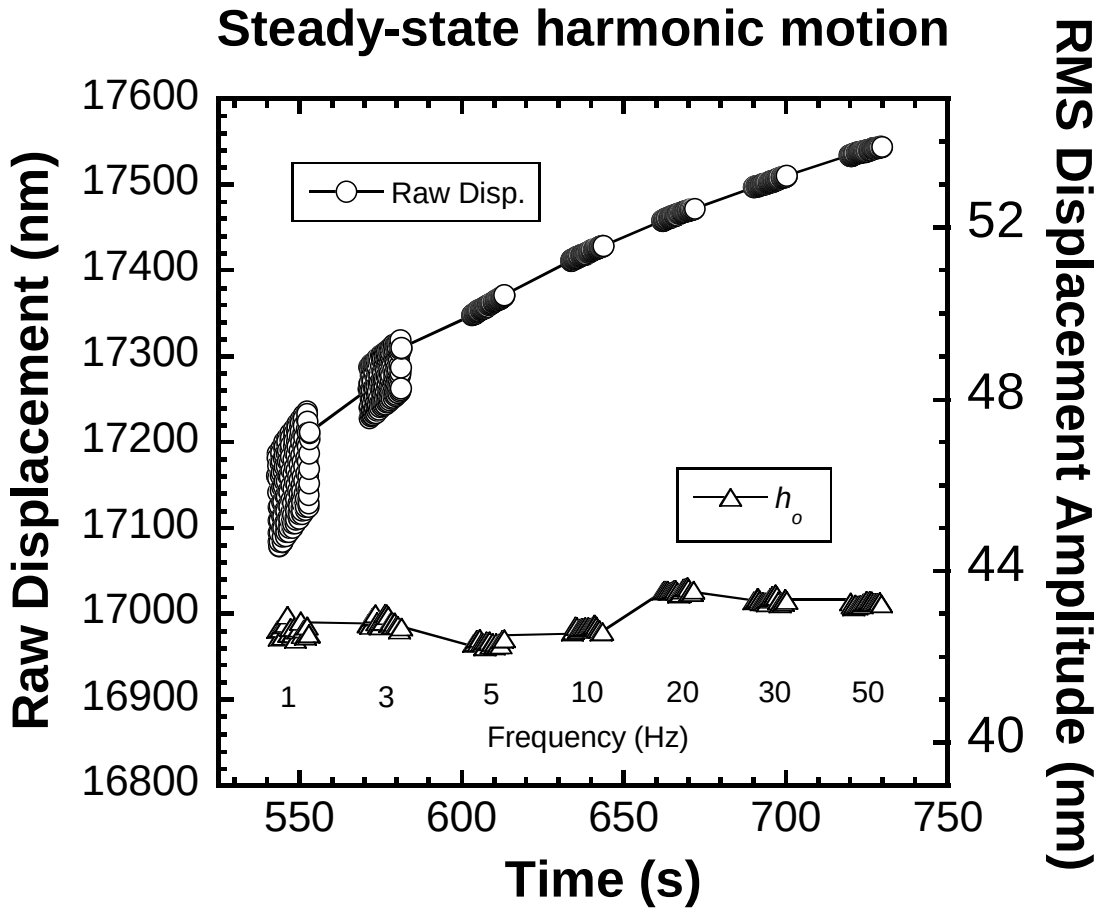


Figure 1.6. The raw displacement and oscillation amplitude as a function of time for a typical measurement performed on the sample. At each frequency, the harmonic load is different but fixed. The resulting oscillation amplitude is constant at each frequency only because the contact area does not change, despite the transient behavior in the raw displacement.

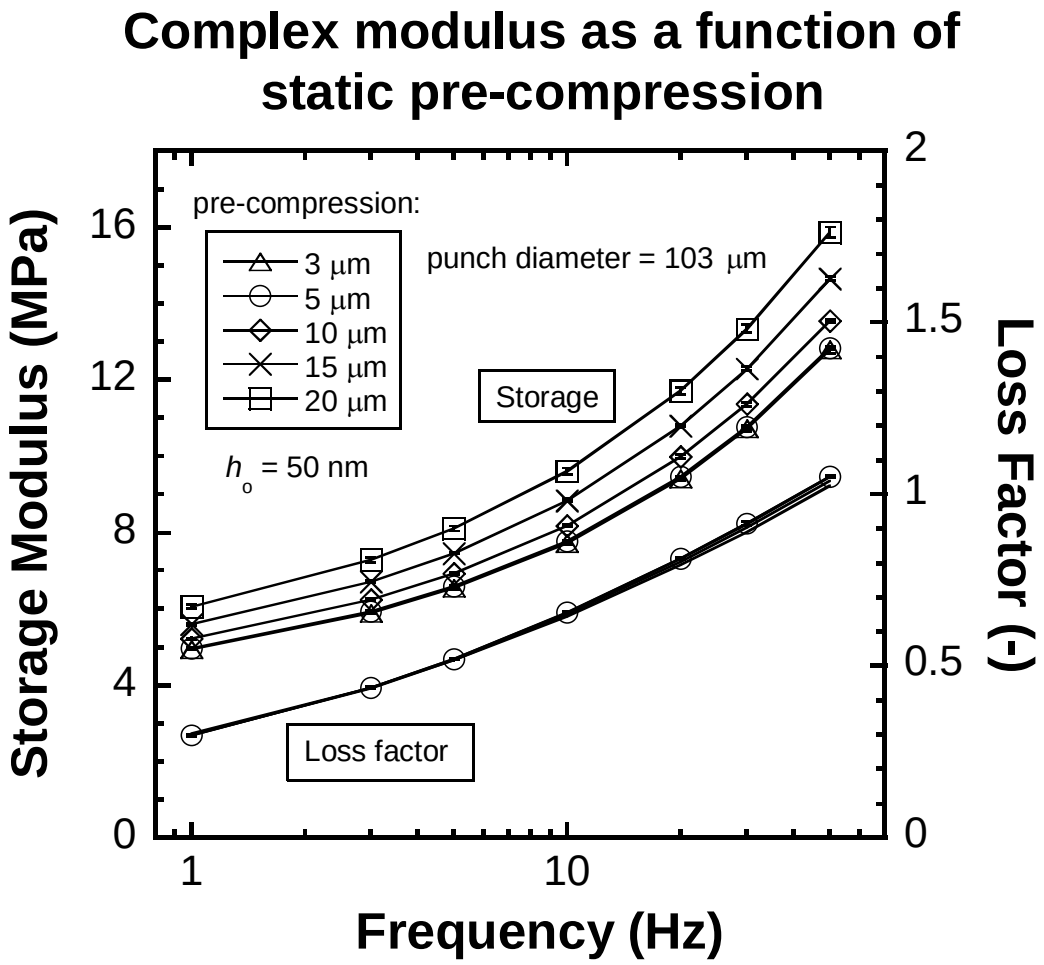


Figure 1.7. The storage modulus and loss factor as a function of frequency and static pre-compression distance. These data show that the static pre-compression distance must be less than 5 μm in order to generate data consistent with the assumptions of linear viscoelasticity.

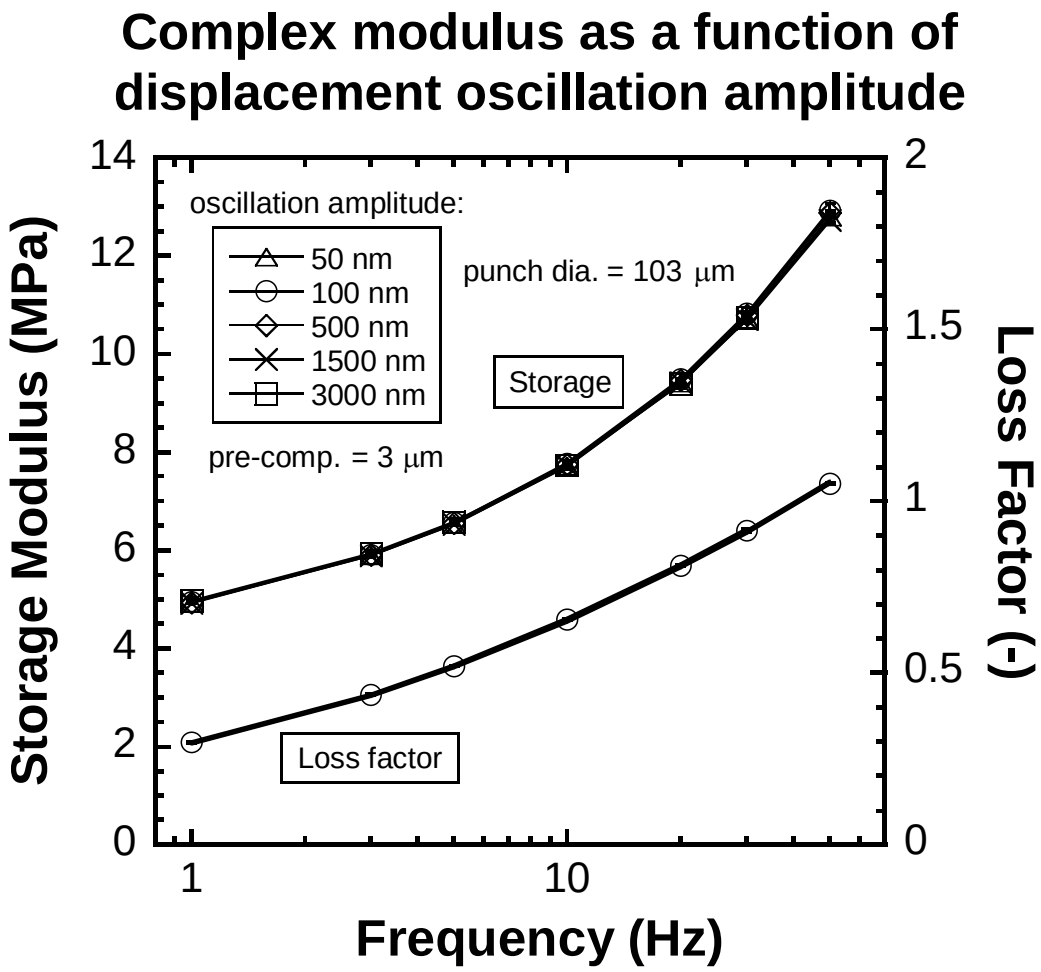


Figure 1.8. The storage modulus and loss factor as a function of frequency and oscillation amplitude. These data clearly show that oscillation amplitudes ranging from 50 to 3000 nm generate data consistent with the assumptions of linear viscoelasticity.

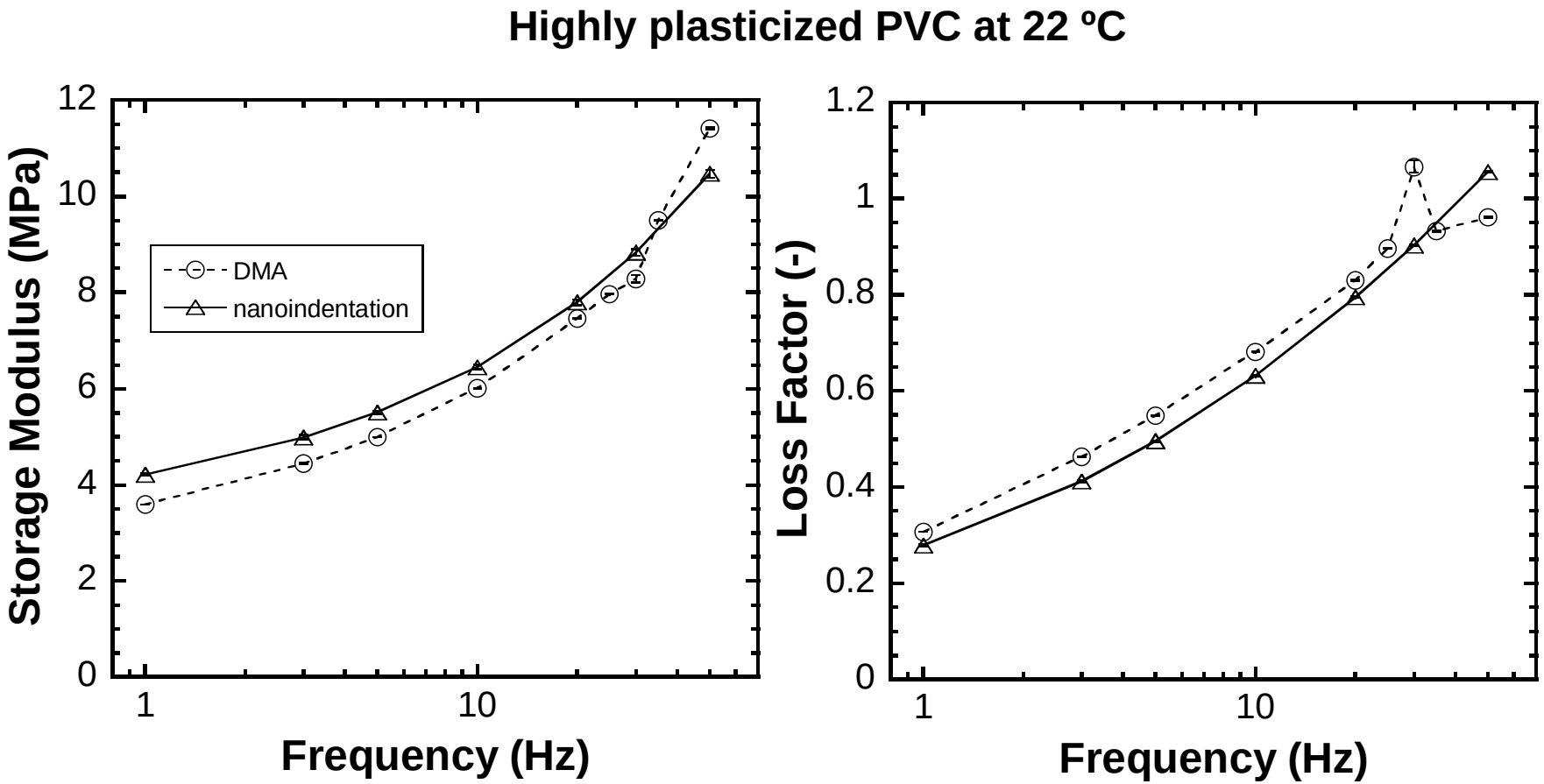


Figure 9. The complex modulus as a function of frequency as determined by dynamic nanoindentation and DMA.

Measuring the constitutive behavior of viscoelastic solids in the time and frequency domain using flat punch nanoindentation

E. G. Herbert[1], W. C. Oliver[1], A. Lumsdaine[1], and G. M. Pharr[2]

[1] MTS Nano Instruments Innovation Center,

[2] University of Tennessee, Dept. of Materials Science and Engineering;

& Oak Ridge National Laboratory, Materials Science and Technology Division

Abstract

The purpose of this work is to further develop experimental methodologies using flat punch nanoindentation to measure the constitutive behavior of viscoelastic solids in the frequency and time domain. The reference material used in this investigation is highly plasticized polyvinylchloride (PVC) with a glass transition temperature of -17 ^{o}C. The nanoindentation experiments were conducted using a 983 μm diameter flat punch. For comparative purposes, the storage and loss modulus obtained by nanoindentation with a 103 μm diameter flat punch and dynamic mechanical analysis are also presented. Over the frequency range of 0.01 to 50 Hz, the storage and loss modulus measured using nanoindentation and uniaxial compression are shown to be in excellent agreement. The creep compliance function predicted from nanoindentation data acquired in the frequency domain is also found to be in excellent agreement over two decades in time with the creep compliance function measured using a constant stress test performed in uniaxial compression. A constraint factor of 1.55 is found to overlay the creep compliance function measured by nanoindentation in the time domain with the creep function measured in uniaxial compression. Time-temperature superposition of nanoindentation data taken at 5, 10, 15, and 22 ^{o}C show the sample is not thermorheologically simple and thus the technique cannot be used to expand the mechanical characterization of this material. Collectively, these results clearly demonstrate the ability of flat punch nanoindentation to accurately

and precisely determine the constitutive behavior of viscoelastic solids in the time and frequency domain.

1. Introduction

Nanoindentation experiments are attractive because they provide the opportunity to characterize a wide range of materials with spatial resolutions in the nanometer to micrometer range. However, contact experiments introduce additional complexity in interpreting experimental data because the state of stress and strain in the volume of material being sampled is not uniform. While the instrumentation is capable of performing experiments at very small length scales (tens of nanometers in contact size), the relationship between the measured quantities such as load, displacement, and stiffness, to the constitutive behavior of the sample is seldom clear, even from contact dimensions in the micrometer range. Only by comparing results from nanoindentation experiments to properties determined by techniques that are well understood is it possible to investigate the ability of nanoindentation to accurately and precisely determine the constitutive behavior of viscoelastic solids. Over the frequency range of 1 to 20 Hz, the nanoindentation technique has been applied to a low modulus, high damping thermoplastic and shown to correlate well with the storage and loss modulus obtained using dynamic mechanical analysis (DMA) [1]. Among the goals of this work is to compare nanoindentation results to an even simpler test

geometry, uniaxial compression. Compression experiments provide the opportunity to maintain a uniform state of stress and strain, and although constraint effects at the top and bottom platens may influence the test results, the effects are negligible, as the imposed strain can be accurately controlled and kept to less than 2%. The ultimate utility of measuring the constitutive behavior in uniaxial compression is that it provides a comparative basis and thus the opportunity to better understand the results obtained by nanoindentation.

Contact experiments are performed with various tip geometries. Among the most frequently used are spheres, pyramids, punches, cones, and wedges. Since each geometry has its own unique advantages and disadvantages, it is important to carefully consider which geometry is best suited for a given application. In terms of characterizing viscoelastic behavior, no single tip geometry provides the best solution. Pyramids, particularly the Berkovich, are used extensively for numerous applications because the sharp geometry affords a high degree of spatial resolution and it induces plasticity at a shallow depth. However, because of the self-similar geometry, pyramids (and cones) impose a strain that is constant with depth, and thus, as recently demonstrated in the literature, pyramids may impose a level of strain that exceeds the small strain assumptions of linear viscoelasticity [2-4]. Furthermore, for low modulus materials, the sharp tip produces a compliant contact that can make it difficult to accurately determine the point of contact between the indenter tip and the surface of the sample. Spheres, on the other hand, have been shown to generate data consistent with

the assumptions of linear viscoelasticity [2-4]. However, it is difficult to accurately manufacture small radii spheres, and, in the presence of transient behavior, the changing contact area prevents meeting the conditions of steady-state harmonic motion and a known contact area, both of which are criteria required of experiments performed in the frequency domain. The flat punch indenter geometry alleviates these problems because the contact area can be directly measured and it is not affected by transient behavior or thermal drift; this is not true of any other tip geometry. The flat punch is not without its drawbacks, however, the most significant of which is that the punch cannot be mounted perfectly normal to the test surface. There is always a small angle between the face of the punch and the surface of the sample. As a result, the test method must have a robust means of identifying the point at which the face of the punch is brought in full contact with the surface of the sample. In addition, the punch geometry also creates a stress concentration along the circumference of the contact. It is assumed that the contribution of the stress concentration to the measured load, displacement, and stiffness is negligible. However, this has not been confirmed experimentally.

2. Theory

2.1 Flat punch nanoindnetation

The details associated with making meaningful measurements in the frequency domain using nanoindentation have been identified elsewhere [1]. To summarize, accurate measurements must be accompanied by rigorous characterization of the measurement system itself and the data must be representative of steady-state harmonic motion, a known contact geometry, and linear viscoelasticity. Only under these conditions is the measured frequency response of the sample uniquely related to the sample's behavior in the time domain.

For linear viscoelastic behavior, the elastic-viscoelastic correspondence principle is valid and thus Sneddon's stiffness equation, the fundamental equation of nanoindentation, may be used to relate the dynamic stiffness and damping of the contact to the storage and loss modulus through [5,6],

$$\frac{E'}{1-\nu^2} = \frac{F_o}{h_o}\cos\phi\frac{\sqrt{\pi}}{2}\frac{1}{\beta}\frac{1}{\sqrt{A}}, \qquad (1)$$

and

$$\frac{E''}{1-\nu^2} = \frac{F_o}{h_o}\sin\phi\frac{\sqrt{\pi}}{2}\frac{1}{\beta}\frac{1}{\sqrt{A}}, \quad (2)$$

where E' is the storage modulus, E'' is the loss modulus, ν is Poisson's ratio, F_o is the amplitude of the harmonic load oscillation, h_o is the resulting harmonic displacement amplitude, ϕ is the phase angle between the harmonic load and displacement, β is a term related to the geometry of the contact, and *A* is the projected contact area. β = 1 for a circular contact (circular flat punch, sphere, and cone), and β = 1.034 for a triangular pyramid, which is often applied to the Berkovich [7]. If the experiments are performed with a circular flat punch indenter, then there is virtually no ambiguity in the contact area and there is little debate that the most appropriate value of β = 1. When the stiffness and damping are measured with a standard deviation less than 1%, which they frequently are, the assumed value of Poisson's ratio becomes the dominant source of error in using Eq.'s 1 and 2 to estimate E' and E''. For viscoelastic solids, the uncertainty in Poisson's ratio may also be compounded by the fact that Poisson's ratio can be frequency dependent [8]. It is important to note, however, that a generous uncertainty in Poisson's ratio, 40% for example, is significantly attenuated in determining E' and E'', as the resulting error is approximately 5.3%. In the absence of information about Poisson's ratio for the sample in this investigation, it is assumed to be 0.42. While the dependence on Poisson's ratio could be avoided by reporting the results as $E^* = \frac{E'}{1-\nu^2}$, this

would preclude making any comparison to the results obtained in uniaxial compression, as E' and E'' estimated from the compression experiments are not directly dependent on Poisson's ratio (see Eq.'s 7 and 8).

The creep compliance function measured in uniaxial compression is defined as

$$D(t) = \frac{\varepsilon(t)}{\sigma_o}, \tag{3}$$

where $\varepsilon(t)$ is the strain as a function of time, and σ_o is the constant applied step in stress [9,10]. The problem in applying this expression to contact experiments is that the stress and strain are largely unknown. In a nanoindentation experiment, the stress, σ, is taken to be proportional to the mean pressure, or the hardness, *H*,

$$\sigma \propto H = \frac{P}{A}, \tag{4}$$

where *P* is the applied normal load, and *A* is the face area of the flat punch indenter. The strain, ε, is taken to be proportional to the measured displacement, *h*, divided by the diameter of the punch, *D*,

$$\varepsilon \propto \frac{h}{D}. \tag{5}$$

Based on Eq.'s 4 and 5, the definition for the creep compliance function determined by nanoindentation is therefore

$$D(t) = C\frac{h}{HD}, \tag{6}$$

where C is a factor that provides the scaling between stress and strain in an indentation experiment. In contrast to experiments performed in the frequency domain, where Sneddon's stiffness equation relates the measured stiffness and damping to the contact geometry, the scaling factor in the time domain, referred to here as C, is unknown.

2.2 Uniaxial compression

By virtue of the cylindrical sample geometry, conditions of uniaxial stress and strain are achieved, and thus the determination of E', E'', and $D(t)$ are simplified. The storage and loss modulus are defined accordingly as:

$$E' = \frac{F}{h}\cos\phi\left(\frac{L}{A}\right), \tag{7}$$

and

$$E'' = \frac{F}{h}\sin\phi\left(\frac{L}{A}\right), \tag{8}$$

where L is the length of the sample, and A is the cross-sectional area. $D(t)$ is determined in accordance with Eq. 3. End effects due to the sample's high value of Poisson's ratio (assumed to be 0.42) and the sample being constrained by mounting and friction are possible, but are assumed to be negligible given that the strain is kept to less than 2%.

2.3 Constitutive relations

Among the simplest, most useful, and widely used methods in the rheology community to describe the constitutive behavior of viscoelastic solids is through parametric models [10]. They excel at capturing unique features in the data, such as transitions, they can be used to describe data over many decades in frequency or time, they can be expressed in a form directly related to the material properties, and they can be implemented into commercially available finite element codes. The models are typically very sensitive to parameter count, interactions between the parameters, and the data density.

The parametric model used in this investigation is a Prony series consisting of four elements. Two and three element series (the Voigt model and the standard

linear solid) were also fit but the models could not adequately reproduce the data. Expressed as a Prony series, the constitutive relationship for the creep compliance function is

$$D(t) = J_0 + \sum_{i=1}^{4} J_i \left(1 - \exp\left(\frac{-t}{\tau_i} \right) \right), \tag{9}$$

where J_i and τ_i are fitting parameters and *t* is time [10].

The relationship between *D*(*t*) and the components of the complex modulus can be expressed through the storage compliance, J',

$$J' = J_0 + \sum_{i=1}^{4} \frac{J_i}{1 + \tau_i{}^2 \omega^2}, \tag{10}$$

where ω is the radial frequency and

$$J' = \frac{E'}{E'^2 + E''^2}. \tag{11}$$

Using Eq.'s 9 - 11 it is therefore possible to predict the uniaxial creep compliance function, *D*(*t*), from the components of the complex modulus, E' and E'' [10].

3. Experimental measurements

The nanoindentation and compression experiments were performed using the NanoIndenter® XP (MTS Nano Instruments) and the continuous stiffness measurement (CSM) technique, the details of which have been described elsewhere [1,10]. The indentation experiments were conducted using a stainless steel right cylindrical flat punch measuring 983 μm in diameter. The compression experiments were performed with one end of the cylindrical sample glued to a glass slide that was rigidly mounted to the sample stage of the instrument. The top compression platen was created by gluing a 6 by 6 mm section of a glass microscope slide to a blank indenter tip holder. The tip holder was mounted in the indenter column and the platen (the 6 by 6 mm section of glass slide) was supported by the sample stage when they were glued together, thereby ensuring the platen was mounted in parallel with the sample stage. The sample was a highly plasticized polyvinylchloride (PVC) with a glass transition temperature of -17 ^{o}C. The indentation sample was approximately 17 mm long, 15 mm wide, and 5 mm thick. The compression sample, which was taken from the same block of material as the indentation sample, was 3.04 mm in diameter and 5.1 mm long. The cylindrical sample was cut using a skin biopsy tool mounted in a drill press. Because it is exceedingly sharp and uniform in shape, the biopsy tool produced samples that were remarkably uniform in shape. The nanoindentation and uniaxial compression experiments performed in the frequency domain (CSM technique) were conducted with a harmonic oscillation amplitude of 50 nm.

Presented here for comparative purposes, the DMA results (E' and E'' over the range of 1 to 50 Hz) have been previously reported [1]. The data were generated using TA Instruments' Q800 and the dual cantilever sample mount. The precision-machined DMA sample, also taken from the same block as the indentation and compression sample, was approximately 35 mm long, 15 mm wide, and 5 mm thick. In an effort to ensure linear viscoelasticity, the DMA experiments were performed using a 20 μm oscillation amplitude. In addition, the experiments incorporated a thermal soak period of 1 hour.

Also previously reported but briefly revisited here for comparative purposes, are nanoindentation data acquired over the frequency range of 1 to 50 Hz at 22 ^{o}C using the NanoIndender XP®, the CSM technique, and a truncated 60 degree diamond cone with a diameter of 103 μm [1]. This sample was also taken from the same block of material and measured 8.2 mm long, 6.8 mm wide, and 7 mm thick. In addition, the NanoIndenter® XP was housed in an ESPEC environmental chamber and the sample was characterized over the frequency range of 1 to 50 Hz at 5, 10, and 15 ^{o}C. The advantage of using an environmental chamber is that the sample temperature is uniform and known with a high level of precision. Furthermore, because the indenter tip is maintained at the sample temperature, the tip does not function as a mechanism for heat transfer. The ESPEC chamber controlled the temperature to within ± 0.1

^{o}C and the system (instrument and sample) was equilibrated at each temperature for approximately 36 hours.

The compression and indentation experiments were performed using the load-time history shown in Figs. 2.1a-d. Among the notable features of the experiment are an initial pre-load to establish full contact with the face of the flat punch or the compression platen, a stabilization period that allows the sample to reach a state of equilibrium, the step load applied to evaluate the creep compliance function, and then low frequency sine waves (ranging from 0.01 to 1 Hz) followed by higher frequency measurements conducted with a phase-lock amplifier (PLA) which characterize the combined frequency response of the sample and the instrument as well as the instrument's response in free space. Upon reaching the prescribed load limit, Fig. 2.1b shows the how the load was controlled in order restrict the strain and stabilize the contact within 50 nm of the displacement at the load limit, hereafter referred to as the displacement target. Using an iterative routine, the sample's relaxation rate was measured over 30 second intervals, during which, the load on sample was held constant. At the end of each interval, the relaxation rate was calculated and then compared to the prescribed stabilization criteria, which was 0.3 nm/s. While the measured relaxation rate was greater than the prescribed stabilization criteria, the routine iterated by reducing the load until the indenter returned to within 50 nm of the displacement target, at which point, the reduced load was held constant for 30 seconds and the new relaxation rate was calculated. Once the measured

relaxation rate was determined to be less than the prescribed stabilization criteria, then the step load was applied. As the data in Fig. 2.1b show, this experiment required 16 cycles to achieve the stabilization criteria of 0.3 nm/s. The data in Fig. 2.1c show that the step load was held constant for 10 minutes and then removed in order to return the indenter to within 50 nm of the displacement target. Although not explicitly shown, the iterative stabilization routine was also used before and after each of the low frequency sine wave measurements, which are shown in Fig. 2.1d. The higher frequency measurements conducted with the PLA, which characterize the combined response of the sample and the instrument, were also performed within 50 nm of the displacement target. The instrument characterization, on the other hand, was performed in free space, which is why the load on sample is near 0 mN from approximately 3600 to 4000 seconds, as shown in Fig. 2.1a.

Performing the creep experiment with a step load is attractive because implementation of the mathematical model (Eq. 3) is simple and the material's transient response at short times correlates well to frequencies that can be readily measured by the NanoIndenter XP® (0.01 to 50 Hz). However, because it is not possible to instantaneously apply any load, it is important to recognize that there is a time limit below which transient data from a step load experiment are not reliable, i.e., the load has not been completely transmitted to the surface of the sample. The limiting factor for the NanoIndenter® XP, and other commercially available systems as well, is rooted in the relationship between the

instrument's dynamic behavior (specifically the mass, stiffness, and damping), the magnitude of the applied step load, and the measurement time constant on the displacement signal. For example, modeling the XP as a simple harmonic oscillator (stiffness, K = 93.2 N/m, damping, c = 2.71 Ns/m, and mass, m = 13.1 g), its displacement-time response to a 6 mN step load in free space shows the indenter reaches 98.3% of its equilibrium position (64.4 μm) in 0.1 seconds. The maximum velocity of 1732.1 μm/s is achieved in approximately 0.01 s and then falls to 47.0 μm/s at 0.1 s. With a 1 ms time constant on the displacement signal, the measured displacement lags behind the actual position by 1732.1 nm (14.2% of the actual position) at 0.01 s and 47 nm (0.07% of the actual position) at 0.1 s. Therefore, at 0.1 s and beyond, the error in the displacement due to the measurement time constant is less than 0.07% and thus, at 0.1 s and beyond, it is possible to adequately measure the displacement-time behavior of the system in response to a 6 mN step load in free space. When the instrument and a sample are coupled through the geometry of the contact, the stiffness and damping increase by an amount that is proportional to the square root of the contact area. As a result, the velocity of the indenter, the lag in the measured displacement, and the time to reach the equilibrium position are reduced. Therefore, it is safe to assume that in response to a 6 mN step load, the full load is transmitted to the sample in no longer than 0.1 s and the measured displacement may be considered an accurate representation of the indenter's actual position.

Among the goals of the dynamic characterization of the sample is to cover the widest frequency range possible. In this investigation, experiments were performed over the range of 0.01 to 500 Hz. At the low end, the practical limit is determined by the patience of the experimenter and thermal drift. At the high end, the limit is generally determined by the highest frequency at which the instrument's frequency response in free space can be accurately modeled as a simple harmonic oscillator, which for the NanoIndenter XP® is approximately 50 Hz [1]. However, under certain conditions, it is possible to exceed the 50 Hz limit and acquire reliable data. These options are discussed in section 4.2.

The frequency response of the sample was measured using two techniques. At 1 Hz and above, the PLA was used to control the harmonic load, measure the phase angle, and recover the sample's displacement response, i.e., the CSM technique. While the PLA is fully capable of performing measurements below 1 Hz, more work is needed to further integrate this capability with the NanoIndenter®. As a result, at 1 Hz and below, sinusoidal loading was generated by controlling the normal load applied to the surface of the sample. In this way, it was possible to produce an elliptical lissajous figure representative of the sample's frequency response, from which the stiffness and damping of the contact could be determined. Above 1 Hz, this technique is limited due to the data acquisition rate and the measurement time constant on the displacement signal; hence utilization of the PLA.

4. Results and discussion

4.1 The time domain

In uniaxial compression, contact between the free end of the sample and the top compression platen was established by applying a pre-load to generate full contact between the compression platen and the surface of the sample. In order to better understand what effect, if any, the pre-load had in determining the creep compliance function, four pre-loads of 100, 200, 300, and 400 mN were investigated. The resulting stress and strain for each pre-load was, respectively, 13.8, 27.5, 41.3, and 55.1 kPa, and 1.1, 1.5, 2.1, and 2.6%. As shown in Figs. 2.1a - c, once the contact was stabilized below 0.3 nm/s, a step load of 6 mN was applied and held constant for 10 minutes. The resulting step in stress was 827 Pa, which, depending on the pre-load, ranged from 1.5 to 6% of the pre-load stress. For linear viscoelasticity, the pre-load is expected to have no effect on the measured displacement-time response. Fig. 2.2 shows the five measurements performed at each pre-load and clearly illustrates that there is no significant dependence in the creep response at 200, 300, and 400 mN of pre-load. The data at 100 mN, however, show a small but measurable increase in the creep displacement as a function of time. Despite significant efforts made to align the compression platen and the sample stage in parallel, it appears that it was not possible to generate full contact for the 100 mN pre-load, as the resulting displacement of 53 μm from the pre-load requires the platens and sample to be

aligned better than 1% to achieve full contact. Because the remaining pre-load data (200, 300, and 400 mN) show very little effect on the displacement-time response, the data are taken to be independent of the applied pre-load, and therefore representative of linear viscoelasticity. For the remaining discussions, all of the compression data (time and frequency domain) were acquired from experiments performed with the 200 mN pre-load, which generated 1.5% strain. Based on these data, the creep compliance function was determined using Eq. 3 and is plotted in Fig. 2.3. The shaded region from $t = 10^{-3}$ to 10^{-1} seconds indicates the region in which the step load has not been fully applied to the surface of the sample. As such, the data in the shaded region are not taken to be representative of the creep compliance function.

The indentation experiments were performed with a pre-load of 80 mN (105 kPa). In order to determine whether or not the data were consistent with the assumptions of linear viscoelasticity, the creep experiments were conducted using three step loads of 1, 3, and 6 mN (1.3, 4.0, and 7.9 kPa); each step load was held constant for 10 minutes. The 80 mN pre-load generated a displacement of approximately 50 μm, which is 5.1% of the diameter of the punch.

In hindsight, it was discovered for the 1 and 3 mN step load experiments that the measured displacement-time response needed a correction to account for a significant contribution from the relaxation associated with the pre-load, i.e., the

0.3 nm/s stabilization criterion was not sufficiently small to be used in conjunction with the 1 and 3 mN step load experiments. For the 6 mN step load, on the other hand, the displacement-time response after 10 minutes was dominated by the step load and thus no correction was necessary. In order to account for the relaxation rate associated with the pre-load in the 1 and 3 mN step load experiments, the relaxation rate over the duration of the creep measurement was measured after applying the 80 mN pre-load and allowing the sample to reach the stabilization criterion of 0.3 nm/s. Fig. 2.4 shows the measured relaxation rate as a function of time for four measurements. As expected, the relaxation rate is near the stabilization criterion at short times and then decreases by nearly 60% over the measured time span. The red line represents a curve fit to the relaxation rate which can be expressed as:

$$\dot{h} = \frac{a + ct}{1 + bt + dt^2}, \tag{12}$$

where $\dot{h}$ is the relaxation rate in nm/s, and t is the time in seconds. The fit coefficients were found to be a = 3.79814339E^{-}1, b = 8.19197E^{-}4, c = -3.9814E^{-}5, and d = -1.0199E^{-}7. For the 1 and 3 mN step load data, the displacement-time response was corrected in accordance with Eq. 12. Fig. 2.5a shows the results from the five measurements performed at each step load. Fig. 2.5b shows that multiplying the 1 and 3 mN creep data by 6 and 2, respectively, brings both displacement-time responses completely coincident with the 6 mN data (which required no correction), thereby demonstrating all three data sets are

representative of linear viscoelasticity. Recalling the previous discussions, the creep data are deemed representative of the sample's transient response to the 6 mN step load over the time scale of 0.1 to 600 s. The creep compliance function was calculated using the 6 mN step load data and Eq. 6 (C = 1) and the result is plotted in Fig. 2.3. The discrepancy between $D(t)$ measured in uniaxial compression and nanoindentation is due to the unknown constraint factor, C. Here, through empirical observation it is found that multiplying the nanoindentation $D(t)$ by 1.55 brings the nanoindentation result remarkably close to $D(t)$ obtained in uniaxial compression, thus suggesting the magnitude of C is approximately 1.55.

4.2 The frequency domain

Fig. 2.6 shows a typical elliptical lissajous figure representative of the sample's displacement response to the sinusoidal loading. The displacement has been drift rate corrected. The drift rate is taken to be the slope of a linear fit to the uncorrected or raw displacement versus time over the duration of the frequency specific measurement. The load on the sample has been corrected to account for the contribution of the dual support springs and the pre-load has been subtracted. No correction has been made to the load to account for the affect of damping in the instrument because its effect is negligible, i.e., at 1 Hz with a harmonic amplitude of 6 mN, the maximum velocity is approximately 8 μm/s, and

assuming the damping coefficient is 2.71 Ns/m, then at the peak velocity damping in the instrument absorbs approximately 22 μN of force, which is only 0.4% of the oscillation amplitude and thus makes no significant contribution. The stiffness of the contact is determined by performing a least squares fit to the load-displacement response, as shown by the red line in Fig. 2.6. The damping of the contact is taken to be the ratio of the load evaluated at zero displacement to the maximum displacement. For the flat punch experiments, E' and E'' are determined using Eq.'s 1 and 2. For the compression experiments, E' and E'' are determined using Eq.'s 7 and 8.

In uniaxial compression, the frequency response of the sample was measured over the range of 0.01 to 500 Hz. Recently reported experimental evidence has demonstrated that the NanoIndenter® XP's frequency response in free space can be accurately modeled as a simple harmonic oscillator only over the range of 1 to 50 Hz [1]. It is possible to use data beyond 50 Hz, however, by utilizing one of the two following options: 1) if the combined response of the sample and the instrument is completely dominated by the sample, then the instrument's contribution may be safely ignored; alternatively, 2) using the known mass, stiffness, and damping of the instrument in conjunction with the simple harmonic oscillator model, the frequency response of the instrument can be predicted and removed from the coupled response [1]. This option, however, is based on the assumption that the additional constraint afforded by the contact prevents other modes of vibration from contributing to the measured frequency response. In

analyzing the data beyond 50 Hz from the compression sample, it was found that the instrument's contribution could not be ignored, as it comprised as much as 80% of the combined response of the sample and the instrument. Therefore, option 2 was employed for the data acquired above 50 Hz. Utilizing the known mass, stiffness, and damping of the instrument, the instrument's contribution was predicted at each frequency and then subtracted from the coupled response. The resulting storage modulus and loss factor $\left(\frac{E''}{E'}\right)$ over the range of 0.01 to 500 Hz are plotted in Fig.'s 2.7a and b. It is not possible to present a compelling argument that explains why the data beyond 50 Hz do not extrapolate smoothly from the data over the range of 0.01 to 50 Hz. If other modes of vibration are preventing the instrument from being accurately characterized in free space beyond 50 Hz, then it appears that the additional lateral stiffness in the coupled response is not sufficient to limit the system to a single degree of freedom when the instrument and sample are coupled through the geometry of the contact. In conclusion, none of the data beyond 50 Hz are deemed valid because the motion of the system is no longer representative of a simple harmonic oscillator, i.e., above 50 Hz an additional mode of vibration is contributing to the response of the system in a way that is not understood.

Nanoindentation experiments performed in the frequency domain using the 983 μm diameter flat punch were conducted over the range of 0.01 to 50 Hz. The estimated E' and loss factor are presented in Fig.'s 2.7a and b. For comparative purposes, the previously reported results from 103 μm flat punch nanoindentation

and DMA experiments are plotted as well; note the 103 μm punch data cover the range of 1 to 50 Hz and the DMA data cover the range of 1 to 25 Hz. As the results show, over the frequency range of 0.01 to 50 Hz, the correlation between the 983 μm flat punch, the 103 μm flat punch, and the uniaxial compression experiments is excellent. Agreement with the DMA data is not as good, but the results agree within 20% or better. It is worth noting that the exceptional correlation between the indentation and compression results suggests that Sneddon's stiffness equation properly relates the measured stiffness and damping to the geometry of the contact.

With the intent of using time-temperature superposition to maximize the frequency range over which the storage and loss modulus were estimated, the PVC was characterized by nanoindentation using a 103 μm diameter flat punch at 5, 10, and 15 ^{o}C. Fig. 2.8 shows the storage modulus as a function of frequency and temperature. The 983 μm flat punch data were acquired at 22 ^{o}C. Implementing empirically derived shift factors, a_T, of 200, 140, and 8, respectively, the storage modulus measured at 5, 10, and 15 ^{o}C superposes remarkably well onto the 22 ^{o}C results, as shown in Fig. 2.9. Superposition of the loss factor, on the other hand, is not as good, as illustrated in Fig. 2.10, which shows the superposition of the storage modulus and the loss factor. The dashed black lines represent the band of expected values based on the sample manufacturers reduced frequency nomogram. In contrast to the storage modulus, superposition of the loss factor does not produce a smooth, continuous

curve because the sample is not thermorheologically simple, i.e., the activation energy associated with each mechanism contributing to the frequency response of the sample is changing with temperature. As a result, these data suggest that time-temperature superposition should not be considered valid for this material and thus the technique should not be used to expand the frequency range over which the storage and loss modulus are estimated.

5. Transformation from the frequency domain to the time domain

As evidenced by the results shown in Fig.'s 2.7a and b, nanoindentation experiments performed in the frequency domain correlate very well with results obtained in uniaxial compression. Assuming the constitutive relations expressed by the prony series provide a reliable path to transform data in the frequency domain to the time domain, then the storage and loss modulus measured by nanoindentation can be used to predict the creep compliance function at times faster than the full step load can be applied in a constant stress test. In accordance with Eq. 11, J' was calculated using the values of E' and E'' measured by the nanoindentation experiments performed with the 983 μm flat punch. The 4 term prony series fit to J' versus the radial frequency is shown in Fig. 2.11. Based on the coefficients from the fit, Eq. 9 was used to predict $D(t)$. Fig. 2.12 shows $D(t)$ measured in uniaxial compression in the time domain, $D(t)$ predicted from nanoindentation data acquired in the frequency domain, and $D(t)$

measured by nanoindentation in the time domain. The data showing $D(t)$ measured in uniaxial compression and measured by nanoindentation in the time domain represent 1 of the 5 measurements performed on each sample, and the results are only plotted for $t > 10^{-1}$ seconds. As the data show, the correlation between the transient response predicted from nanoindentation data in the frequency domain and the transient response measured in uniaxial compression in the time domain is very good over nearly two decades, from 0.1 to 10 seconds. The plateaus at either end of the predicted $D(t)$ are not considered valid because they are the result of the parametric model extrapolating beyond the experimentally acquired data, as shown in Fig. 2.11. It is observed here for the lowest and highest frequencies, 0.01 and 50 Hz, that $\frac{0.1}{f} = 10$ and 0.002 seconds, respectively. These values are assumed to represent the time scale over which the frequency domain data can adequately predict $D(t)$. As shown in Fig. 2.12, the slower time limit of 10 seconds corresponds very well with the observed deviation between $D(t)$ measured in uniaxial compression and $D(t)$ predicted from nanoindentation data in the frequency domain. At the faster time limit of 0.002 seconds, there is no measured $D(t)$ to make a direct comparison, nevertheless, the value appears to provide a reasonable estimate of the point at which the predicted $D(t)$ is determined by the extrapolated curve fit and not the measured frequency response. These observations suggest that the nanoindentation data acquired in the frequency domain can be used to predicted $D(t)$ over the approximate time scale of 2×10^{-3} to 10^{1}, which is nearly 2 decades lower than can be achieved by measuring $D(t)$ in the time domain alone. The

constraint factor associated with nanoindentation data acquired in the time domain is not well understood, despite the empirical observation that its magnitude is approximately 1.55. Nevertheless, the time domain data measured by nanoindentation can still be used to estimate the uniaxial $D(t)$ by shifting the curve vertically until it coincides with the $D(t)$ predicted from the nanoindentation data in the frequency domain. The vertical shift of the time domain data requires no prior knowledge of the magnitude of the constraint factor, rather it assumes the frequency domain data provide an accurate prediction of the uniaxial $D(t)$. In this way, the time scale over which the uniaxial $D(t)$ can be characterized by nanoindentation is maximized, in this case covering nearly 6 decades in time, from $2x10^{-3}$ to $5x10^{2}$.

6. Summary and conclusions

The data presented in this work demonstrate the ability of flat punch nanoindentation to accurately and precisely measure the components of the complex modulus and the creep compliance function of linear viscoelastic solids. The storage and loss modulus measured by nanoindentation and uniaxial compression were shown to be in excellent agreement over the range of 0.01 to 50 Hz. The constitutive behavior expressed in the form of a Prony series allows nanoindentation data acquired in the frequency domain to accurately predict the creep compliance function measured in uniaxial compression. Combining

nanoindentation data acquired in the frequency and time domain allowed the PVC reference material to be characterized over nearly 6 decades in time without resorting to time-temperature superposition, which was shown to not be applicable for this material. Successful implementation of the nanoindentation technique requires rigorous characterization of the measurement system itself. As required by the models applied to the frequency response of the sample, the data must be representative of steady state harmonic motion, a known contact geometry, and linear viscoelasticity. Only under these conditions are the measured storage and loss modulus uniquely related to the transient functions from which they are derived, namely the creep compliance function and stress relaxation.

References

[1] Herbert, E. G., Oliver, W.C. and Pharr, G. M., J. Phys. D: Appl. Phys. **41** (2008) 074021.

[2] Tweedie, C. A. and Van Vliet, K. J., J. Mater. Res. **21** (2006) 1576.

[3] VanLandingham, M. R., Drzal, P. L. and White, C. C., Mater. Res. Soc. Symp. Proc. **841** (2005) R5.5.1.

[4] Oyen, M. L. and Cook, R. F., J. Mater. Res. **18** 1 (2003) 139.

[5] Sneddon, I. N., Int. J. Eng. Sci. **3** (1965) 47.

[6] Johnson, K, Contact Mechanics, Cambridge University Press (1989).

[7] King, R. B., Int. Journal Solids Struct. **23** (1987) 1657.

[8] Tschoegl, N. W., Knauss, W. G. and Emri, I., Mech. Time-Dependent Mater. **6** (2002) 3.

[9] Lakes, R. S., Viscoelastic Solids, CRC Press (1999).

[10] Ferry, J. D., Viscoelastic Properties of Polymers, John Wiley and Sons, Inc. (1980).

[11] Oliver, W. C. and Pharr, G. M., J. Mater. Res. **19** 1 (2004) 3.

Appendix 2.1.

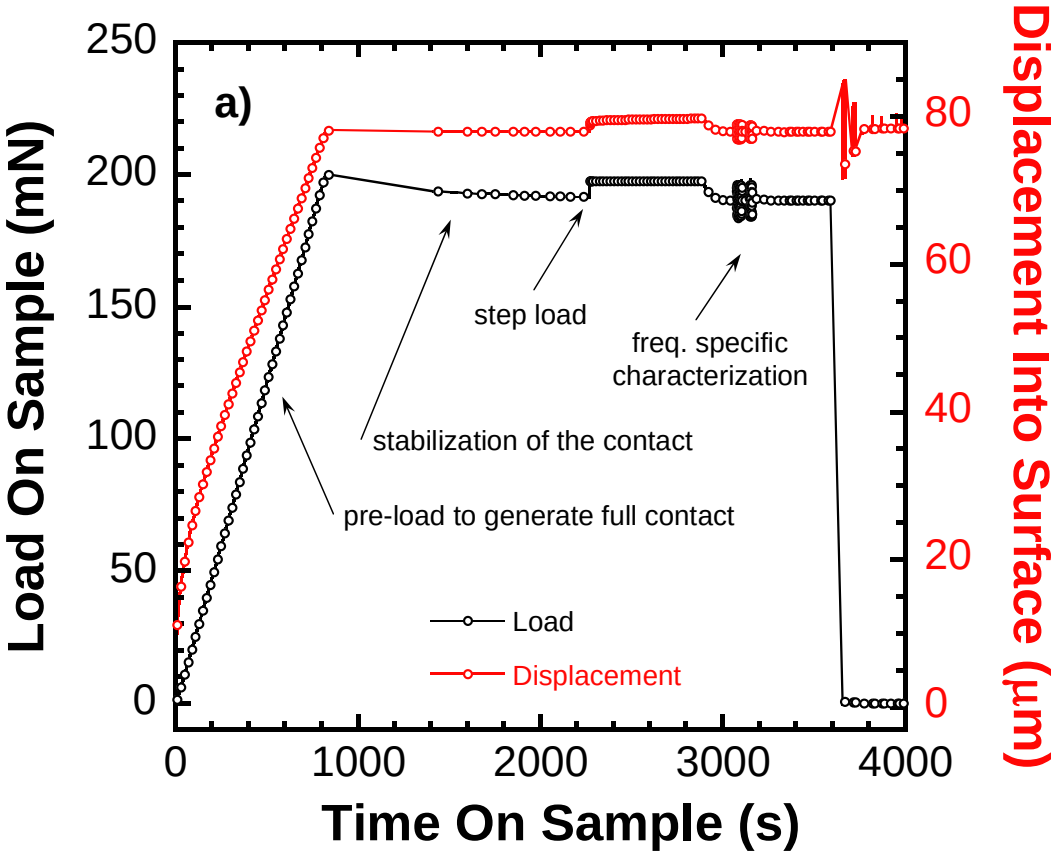


Figure 2.1. The load on sample and the displacement into surface as a function time, a) Data representing a complete experiment, b) Restricting the strain and stabilizing the contact, c) The creep measurement, showing a 6 mN step load and the resulting displacement-time response, and d) Dynamic characterization at 0.5 and 1 Hz.

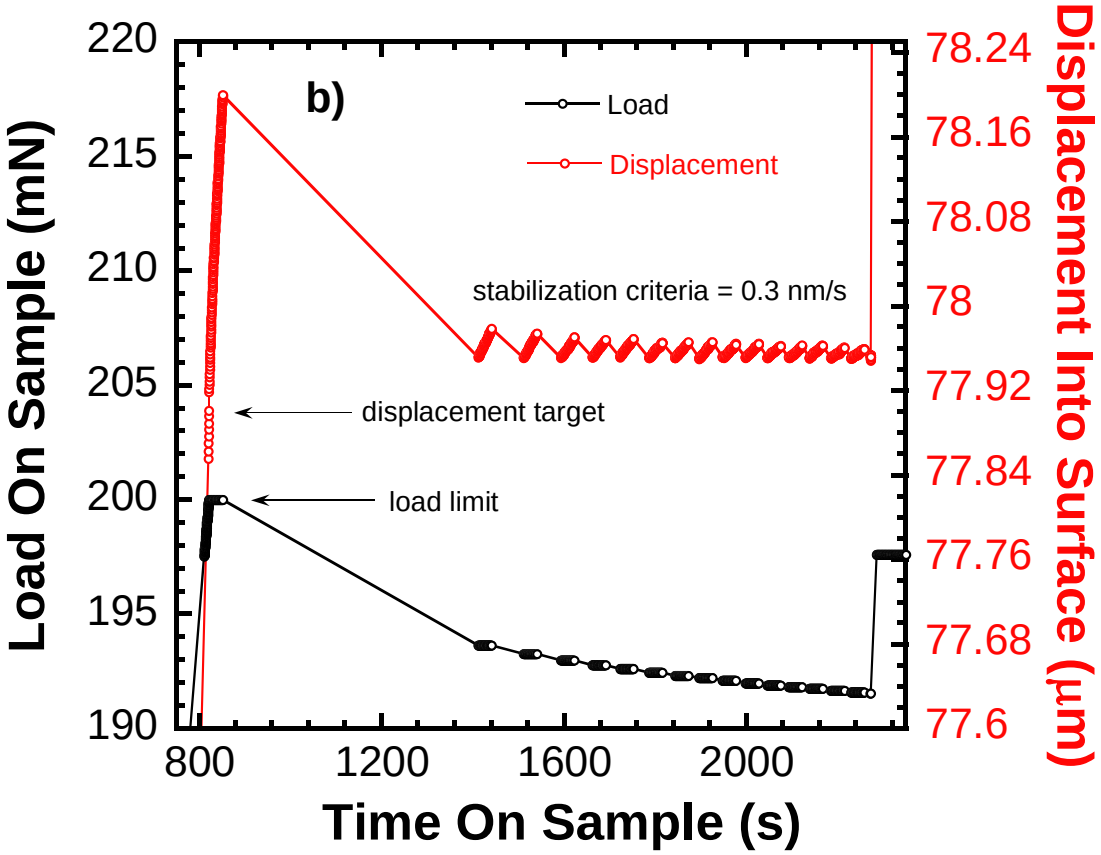


Figure 2.1. Continued.

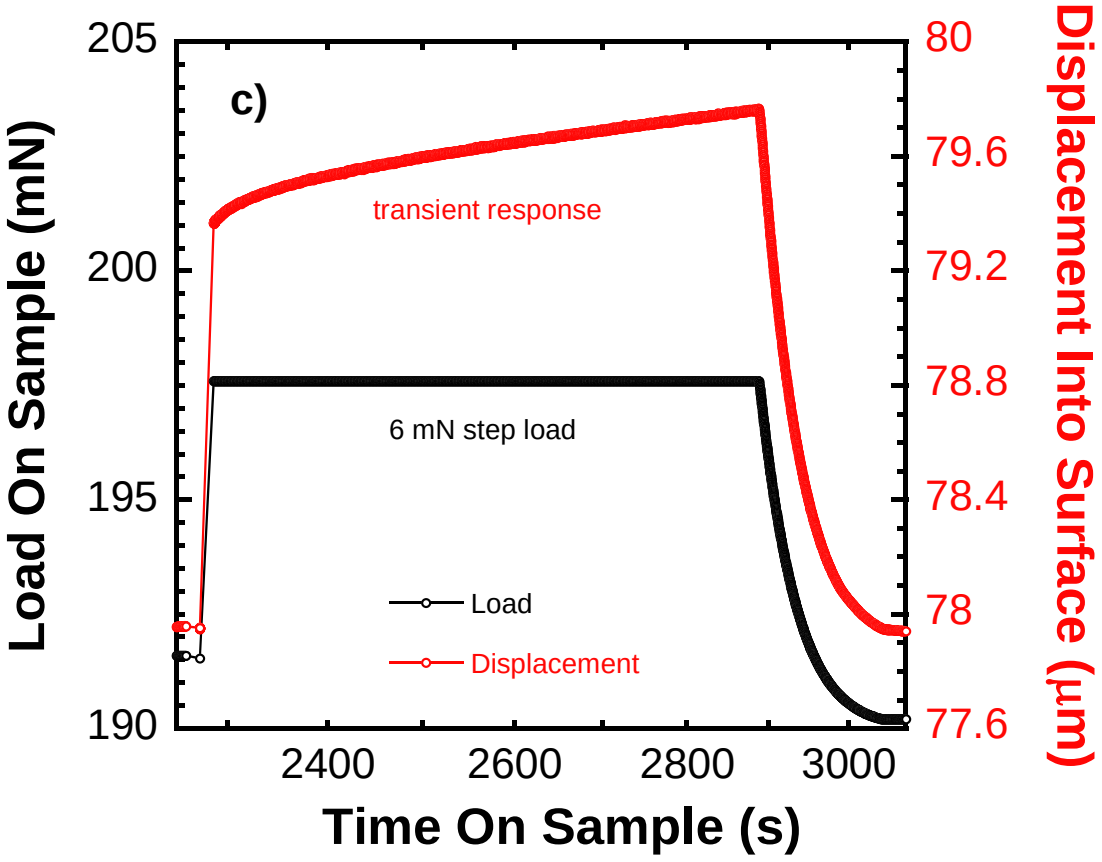


Figure 2.1. Continued.

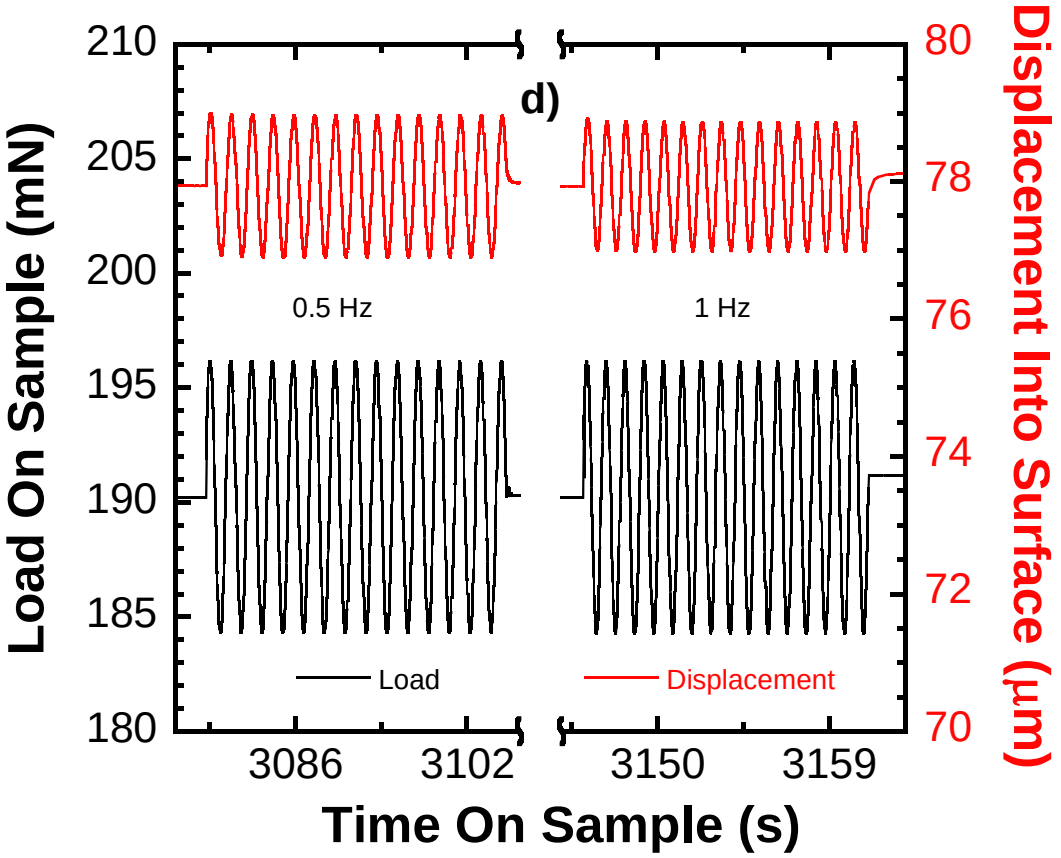


Figure 2.1. Continued.

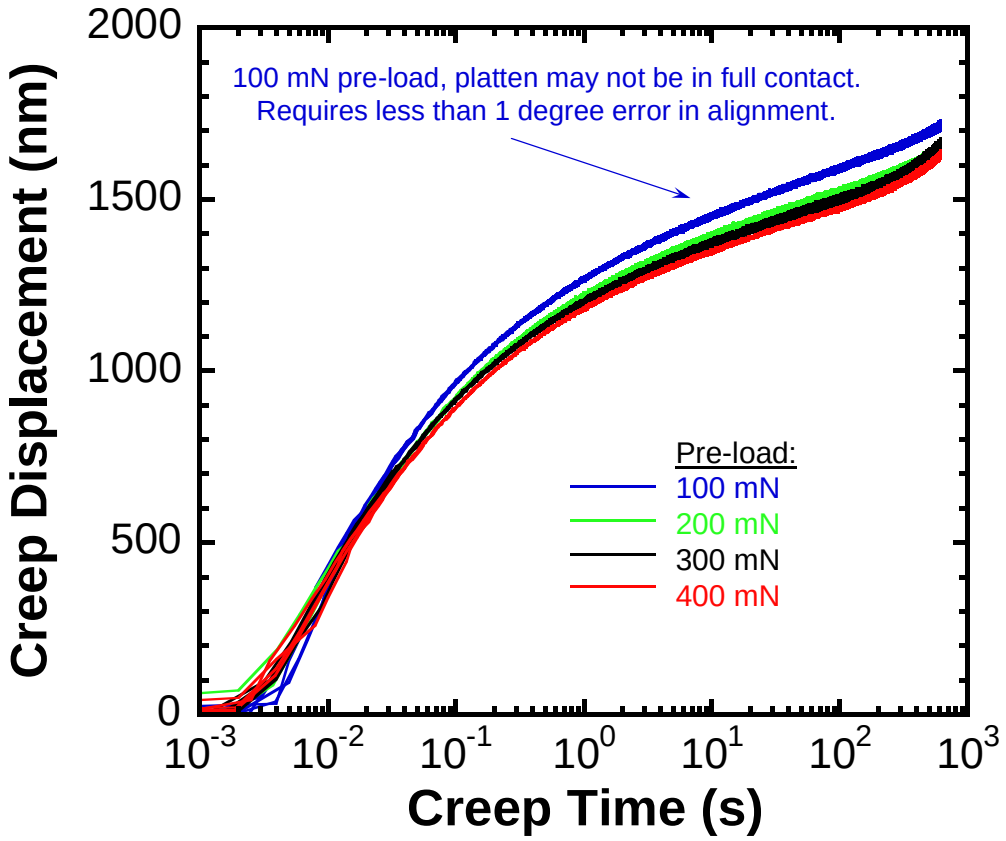


Figure 2.2. The creep displacement as a function of time, measured in uniaxial compression in response to a 6 mN step load. The displacement-time response is shown for 4 different pre-loads, 100, 200, 300, and 400 mN.

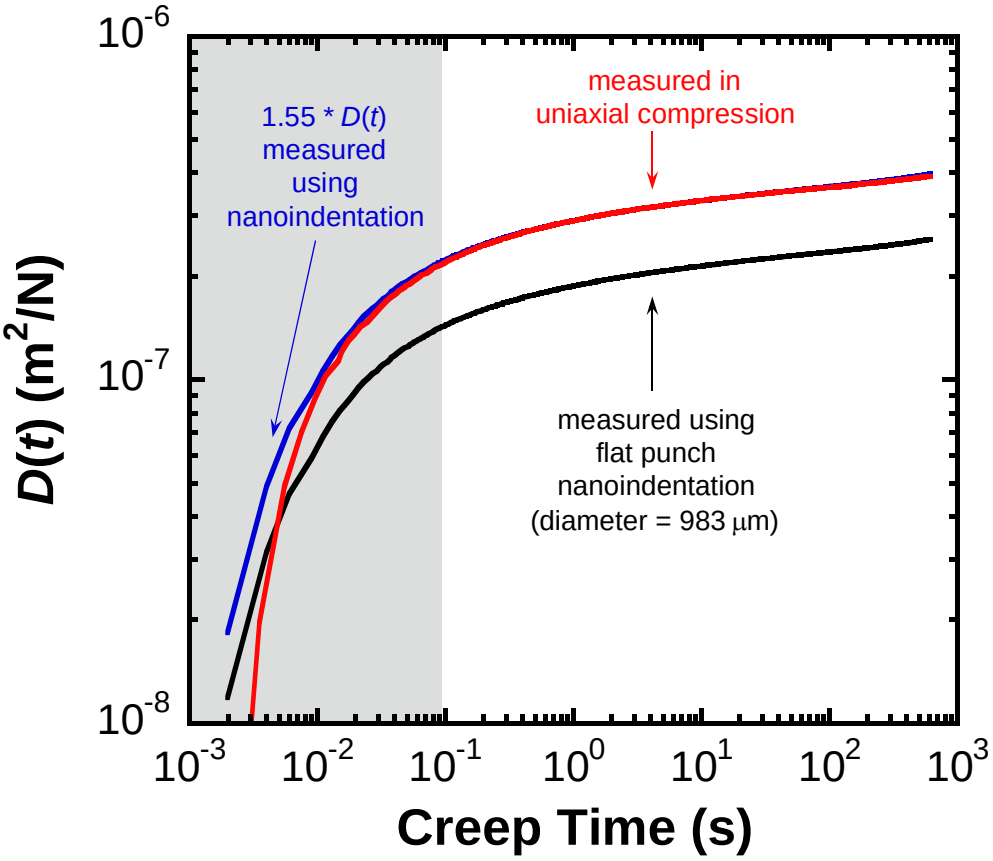


Figure 2.3. The creep compliance function measured in uniaxial compression and by flat punch nanoindentation. The data illustrate 1 of the 5 measurements performed using each technique.

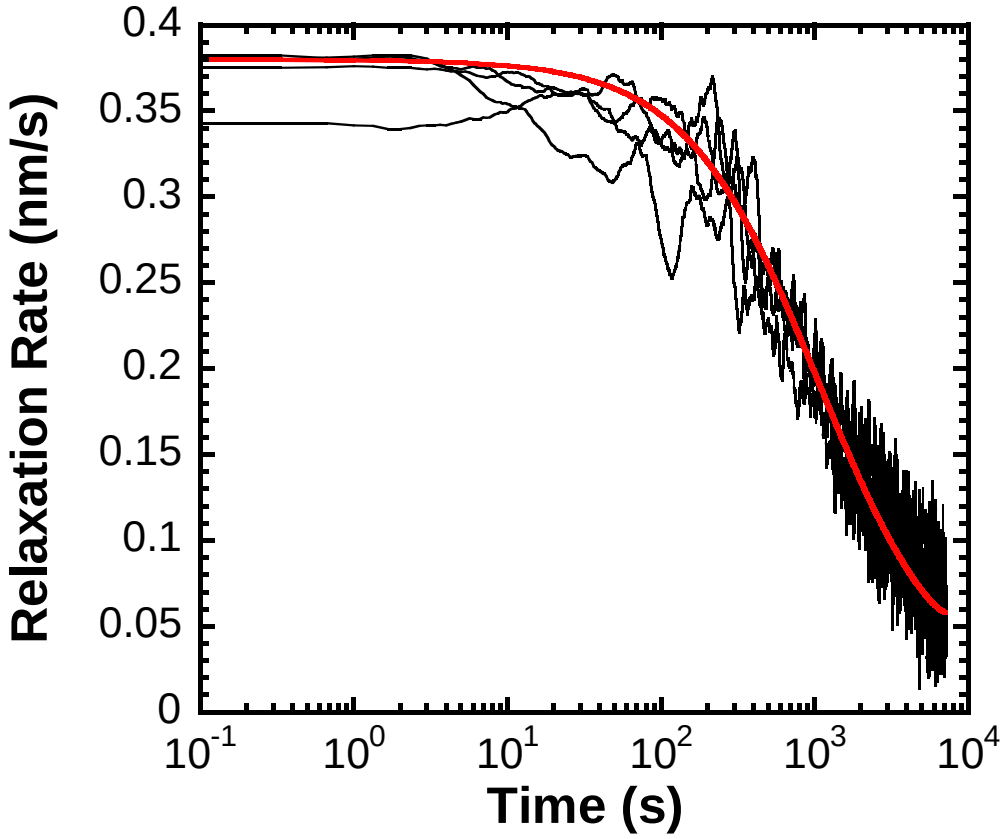


Figure 2.4. The relaxation rate versus time acquired during a flat punch nanoindentation experiment performed with an 80 mN pre-load followed by a stabilization criterion of 0.3 nm/s.

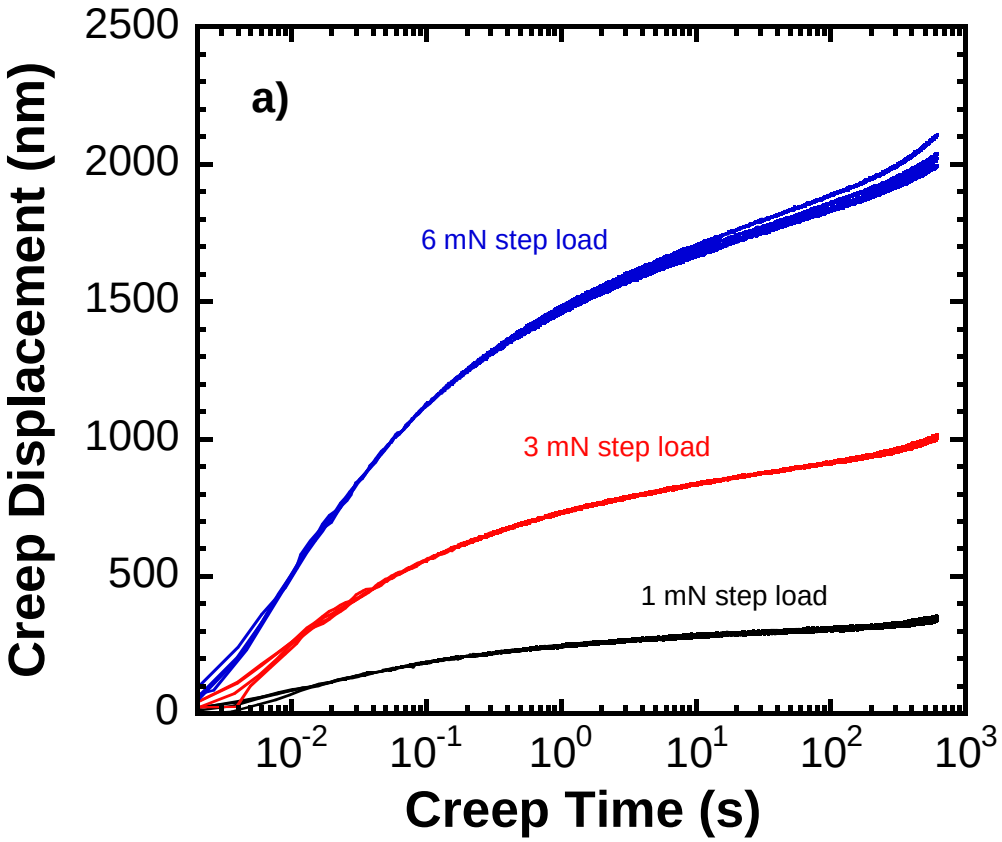


Figure 2.5. a) The displacement-time response measured by flat punch nanoindentation. The 1 and 3 mN data are corrected to account for the relaxation rate associated with the pre-load. b) The 1 and 3 mN data multiplied by 6 and 2, respectively, showing the data are consistent with the assumptions of linear viscoelasticity.

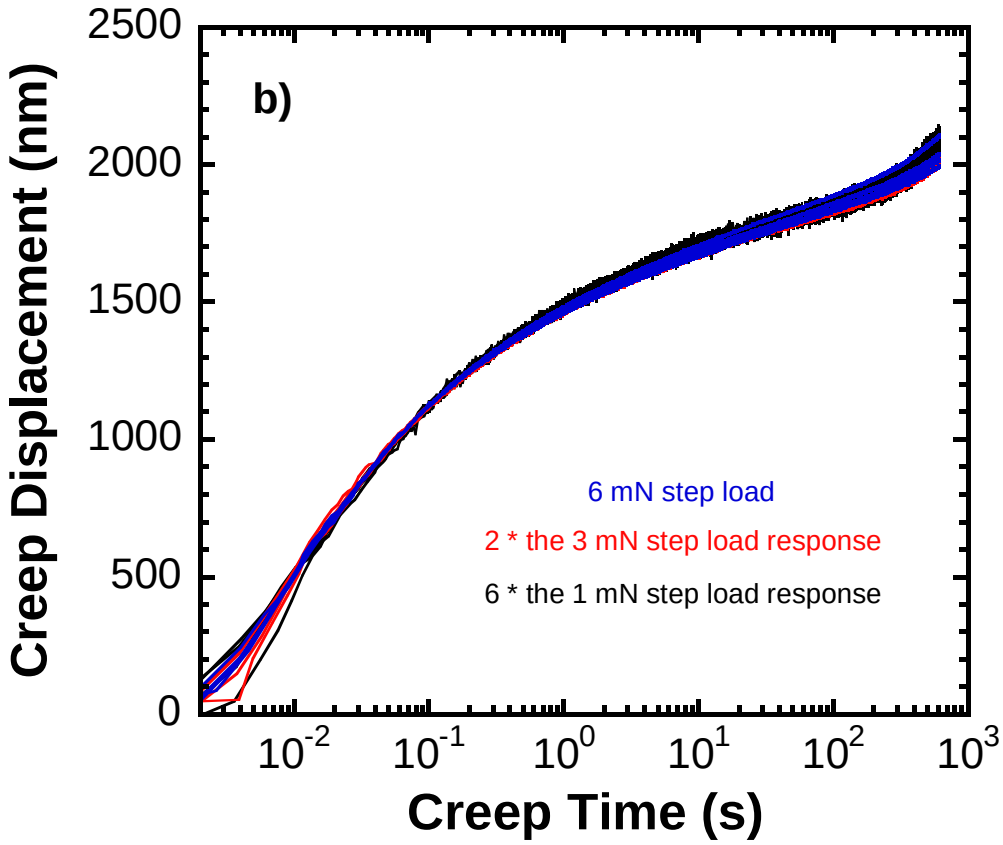


Figure 2.5. Continued.

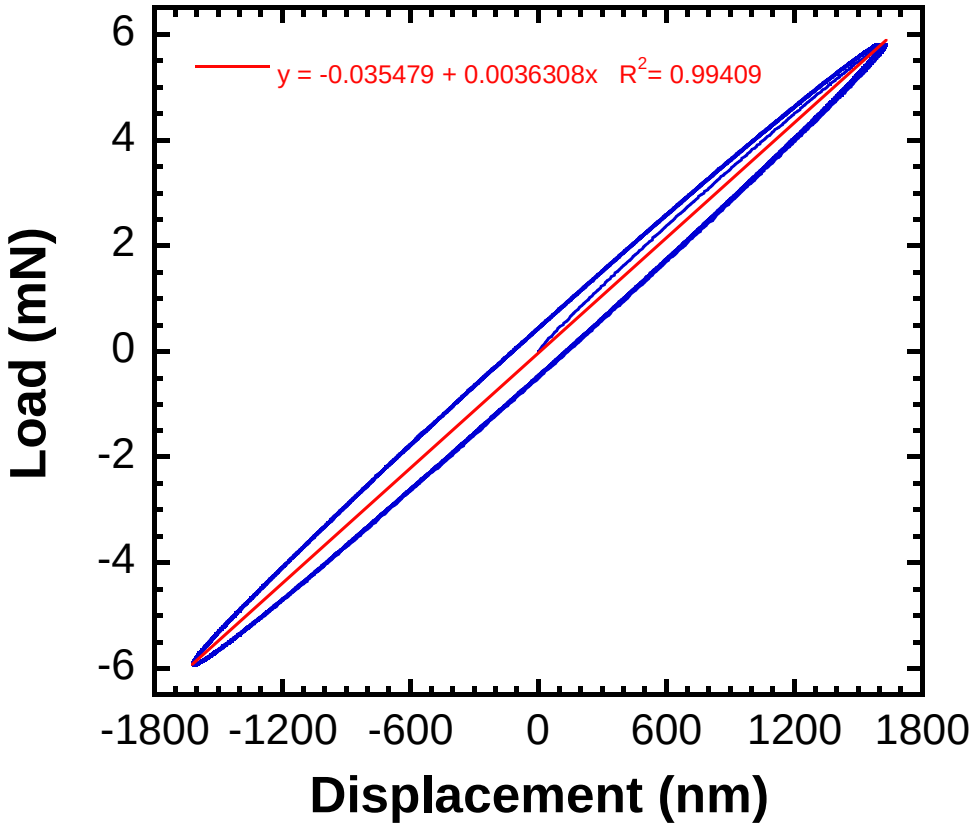


Figure 2.6. A typical elliptical lisajous figures showing the load-displacement response at 0.01 Hz measured by flat punch nanoindentation.

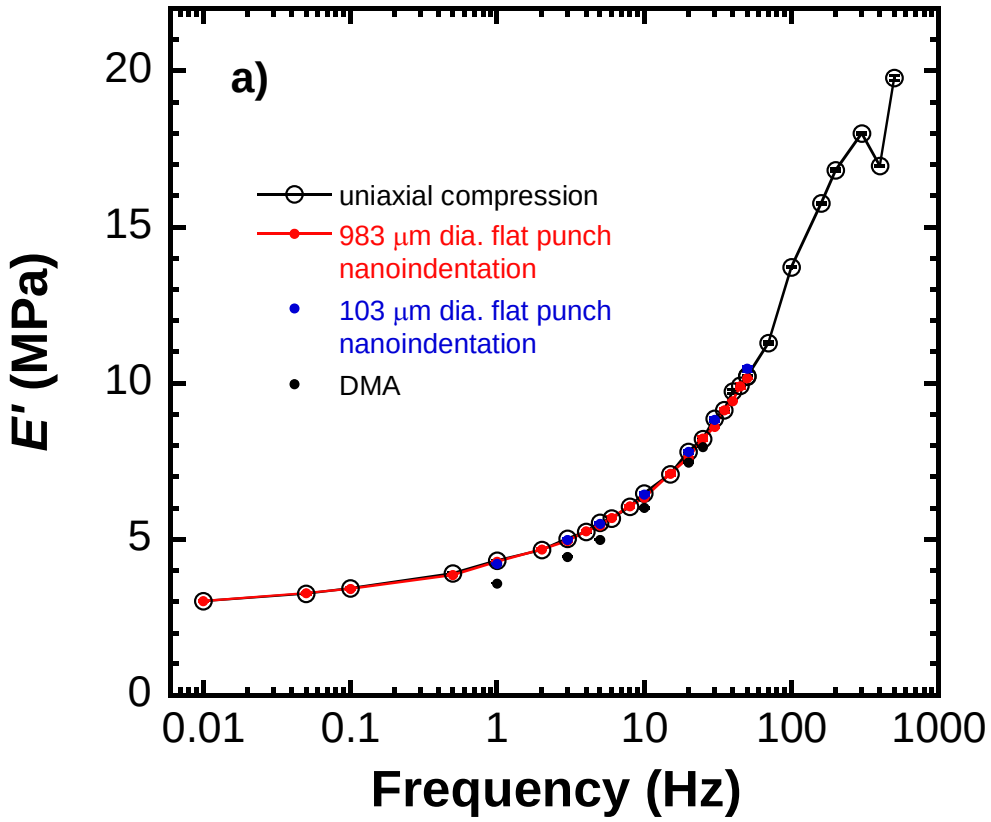


Figure 2.7. a) The storage modulus and b) the loss factor as a function of frequency as determined in uniaxial compression, by flat punch nanoindentation, and DMA.

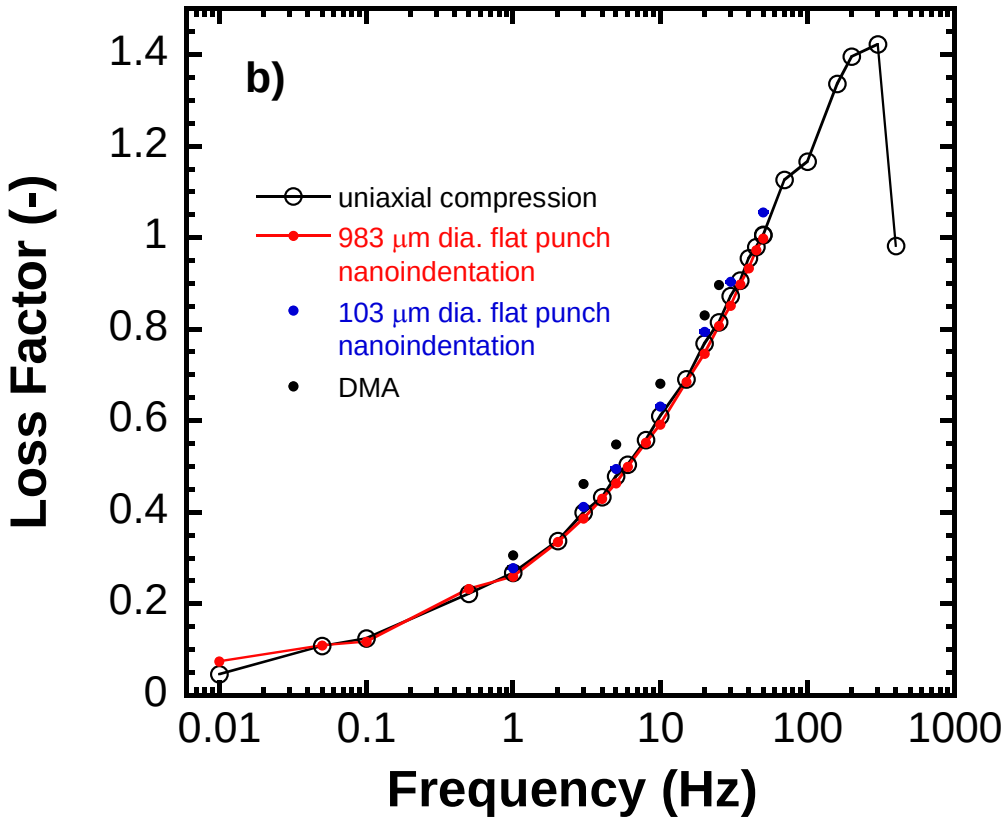


Figure 2.7. Continued.

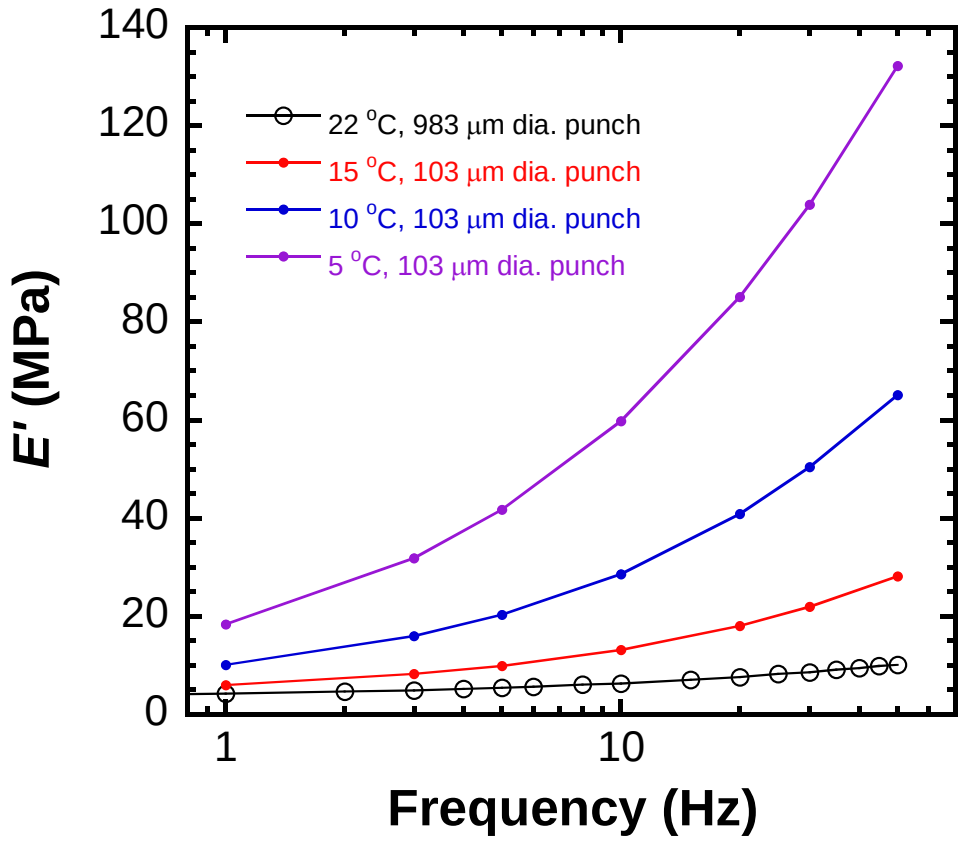


Figure 2.8. The storage modulus as a function of frequency and temperature as determined by flat punch nanoindentation.

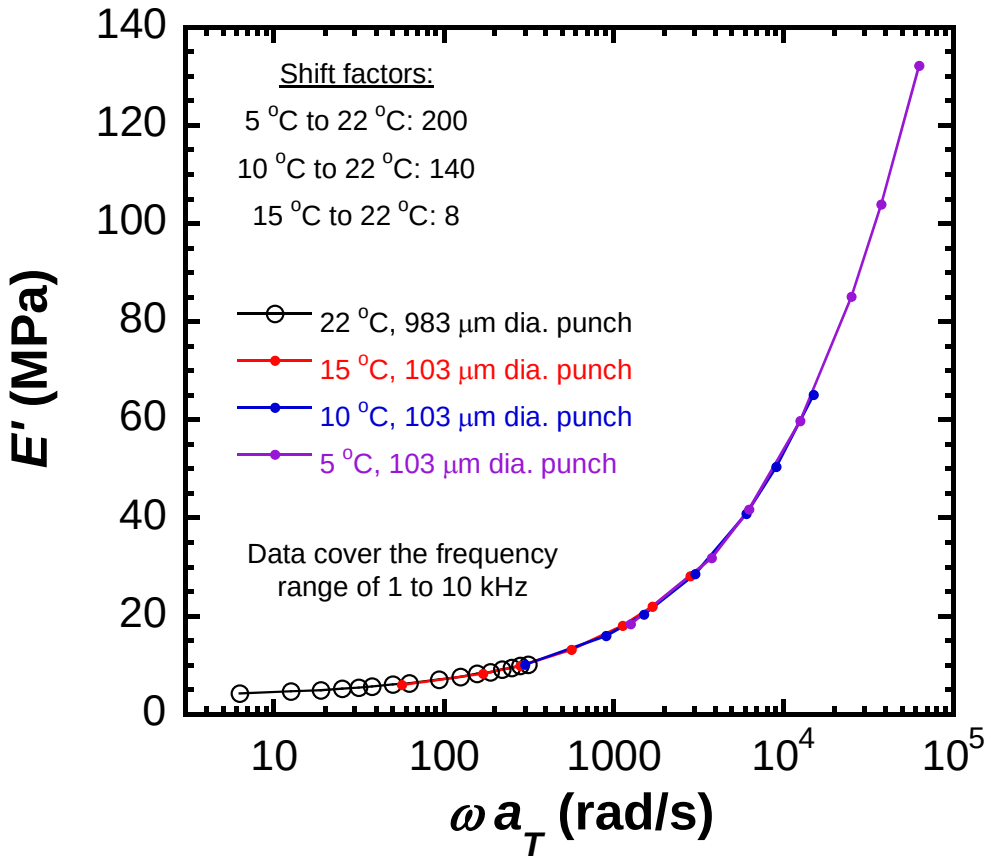


Figure 2.9. Superposition of the storage modulus to 22 °C.

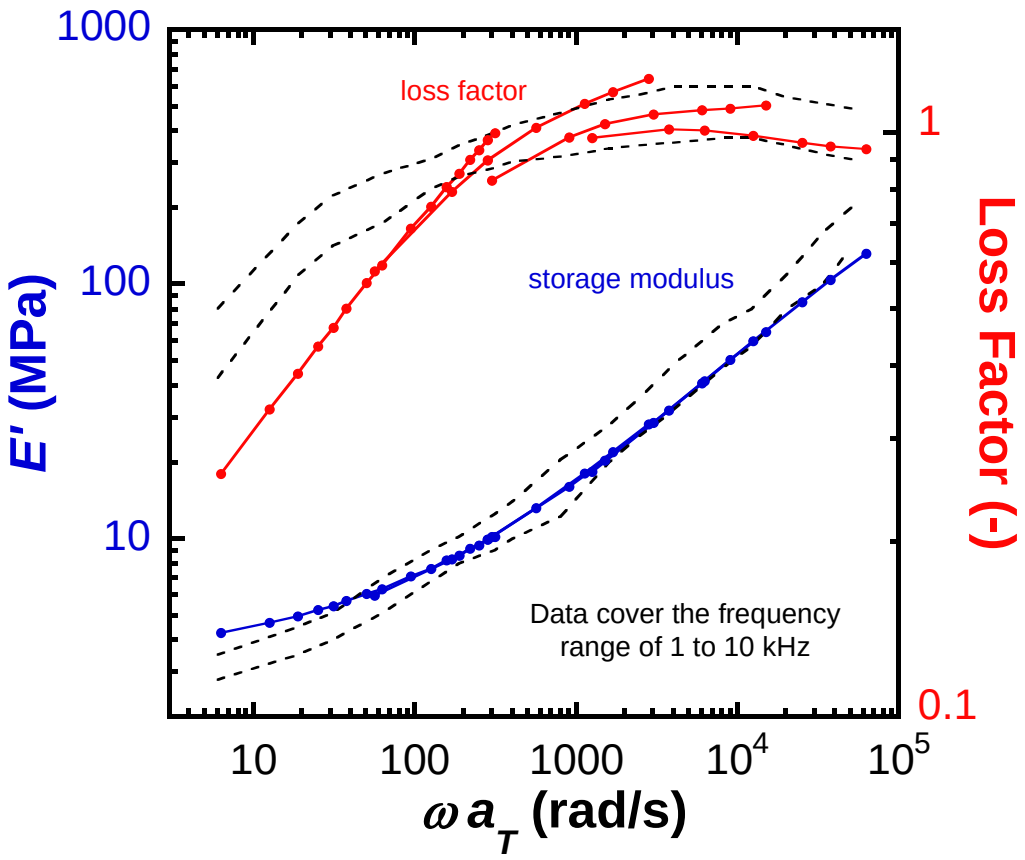


Figure 2.10. Superposition of the storage modulus and the loss factor.

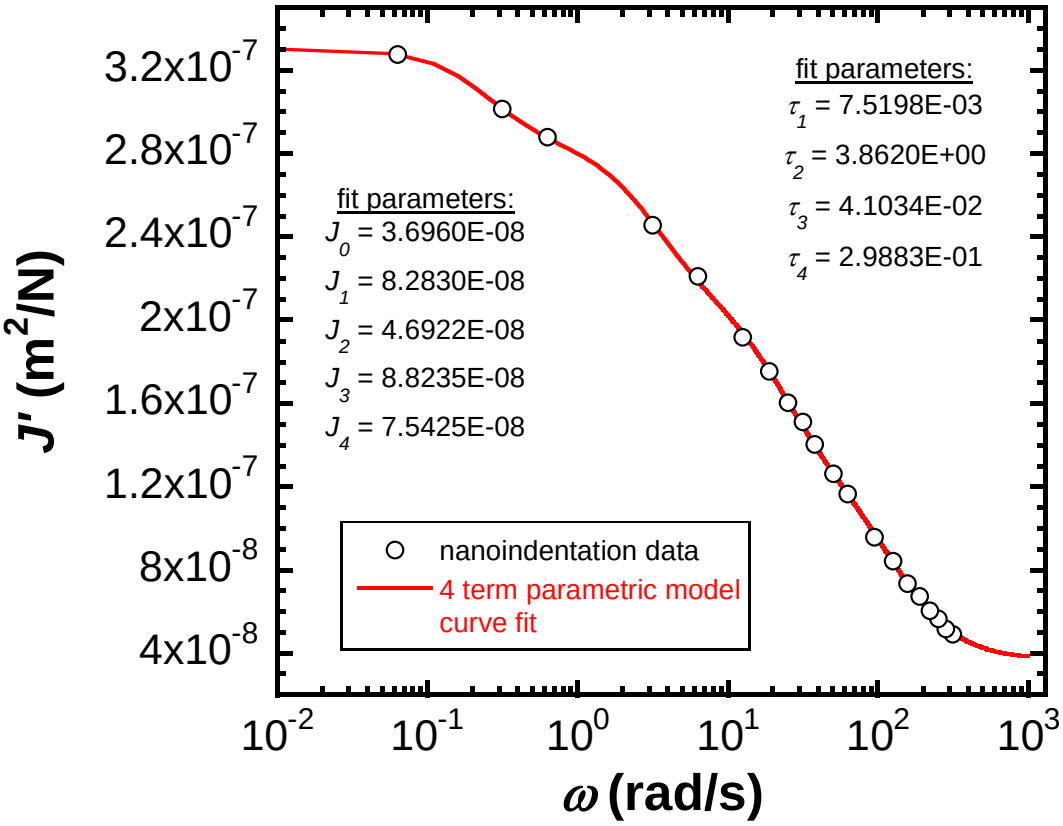


Figure 2.11. The 4 term Prony series fit to *J*' versus radial frequency.

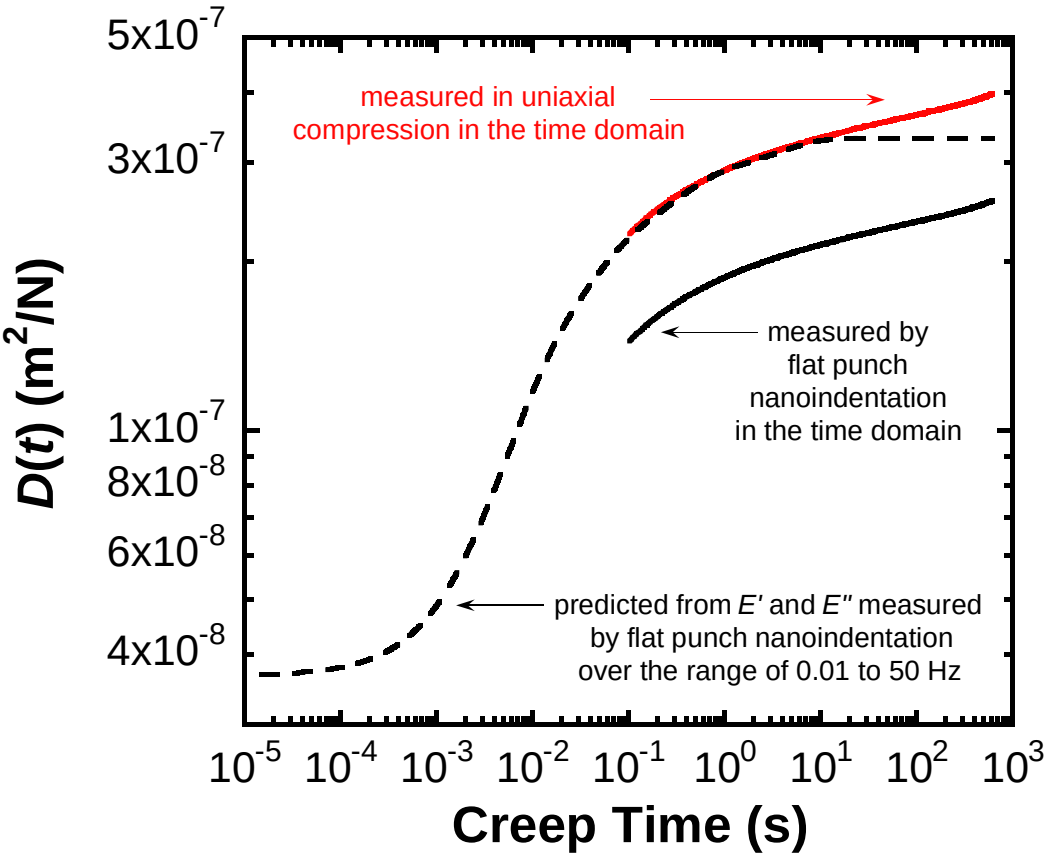


Figure 2.12. The creep compliance function as determined in uniaxial compression and by flat punch nanoindentation experiments performed in both the time and frequency domains.

Measuring the elastic modulus and residual stress of free-standing thin films using nanoindentation techniques

E. G. Herbert[1], W. C. Oliver[1], M. P. de Boer[2], and G. M. Pharr[3]

[1] University of Tennessee, Dept. of Materials Science and Engineering and MTS Nano Instruments Innovation Center;

[2] Carnegie Mellon University, Dept. of Mechanical Engineering and Sandia National Laboratory;

[3] University of Tennessee, Dept. of Materials Science and Engineering and Oak Ridge National Laboratory, Materials Science & Technology Division

Abstract

A new method is proposed to determine the elastic modulus and residual stress of free-standing thin films based on nanoindentation techniques. The experimentally measured stiffness-displacement response is applied to a simple membrane model that assumes the film deformation is dominated by stretching as opposed to bending. Dimensional analysis is used to identify appropriate limitations of the proposed model. Experimental verification of the method is demonstrated for Al/0.5 wt% Cu films nominally 22 μm wide, 0.55 μm thick, and 150, 300, and 500 μm long. The estimated modulus for the four free-standing films match the value measured by electrostatic techniques within 2%, and the residual stress within 19.1%. The difference in residual stress can be completely accounted for by thermal expansion and a modest change in temperature of 3 ^{o}C. Numerous experimental pitfalls are identified and discussed. Collectively, these data and the technique used to generate them should help future investigators make more accurate and precise measurements of the mechanical properties of free-standing thin films using nanoindentation.

1. Introduction

Developing novel techniques to characterize the elastic modulus and residual stress of thin films is an active area of research in the fields of microelectromechanical systems (MEMS) and materials science. In the case of MEMS, a successful product requires the integration of small scale mechanical and electrical components functioning together as sensors, actuators, and switches. As noted by Spearing, the MEMS industry has relied heavily on the past 50 years of research by the microelectronics industry in electrical characterization and fabrication techniques [1]. This research is a key reason for the success of the microelectronics industry, as it forms the basis to quickly and reliably simulate complex devices and thus avoids the need to incorporate extensive prototyping. If the MEMS industry is to realize its full potential, similar design simulation packages will be required, and successful implementation of the simulation process will depend on the accuracy of the mechanical properties used as inputs. Properties such as strength and residual stress are expected to vary with the microstructure of the film and the fabrication technique, with the latter influencing the density and, hence, the elastic modulus [1-4]. Recently, investigators have also argued that the lower than expected modulus values experimentally observed for metallic thin films may be due to microstructural features such as microcracking at grain boundaries [5-7]. Clearly, optimizing thin films to accommodate specific design goals can only be accomplished by

investigating their microstructure and mechanical behavior in their final, microfabricated or deposited form.

The microfabrication techniques developed by the microelectronics industry also open many doors in characterizing thin film mechanical behavior. The ability to produce films with exceedingly well controlled geometries and dimensions provides the opportunity to effectively control the state of stress and strain that result from a film being mechanically loaded during an experiment. In this way, it is possible to achieve the conditions of simple stress and strain, which are well understood and easy to model. Thus, controlling the sample geometry and dimensions enhances the capability to systematically explore structure-property relationships linked to microstructure, film thickness, microfabrication, and deposition techniques.

Over the past 20 years, nanoindentation has played an important role in characterizing the mechanical behavior of thin films and small volumes of material [8-18]. The technique finds widespread application because of its high spatial resolution and its ability to determine mechanical properties without requiring an image of the residual impression. Rather, properties can be determined by modeling the measured load-displacement response of the material under investigation. In addition to measuring the hardness and elastic modulus, numerous investigators have proposed that nanoindentation may also be employed to measure plastic flow properties such as the yield strength, the

work hardening exponent, and in some instances, the entire uniaxial stress-strain curve [10]. Testing methodologies and models also exist to estimate the residual stress, fracture toughness, the stress exponent for creep, adhesion, and time dependent properties of viscoelastic solids such as the stress relaxation modulus, the creep compliance, and the complex modulus [11-18]. However, it is important to recognize that many of the techniques proposed to measure these properties lack the experimental verification required to demonstrate their validity and identify their limitations. In many cases, the primary obstacle in modeling an indentation experiment is the complex state of stress and strain associated with the contact geometry. For example, even in the case of a bulk, homogeneous, isotropic, linear elastic solid, there is no closed form analytical solution to describe the state of stress or strain for an elastic-plastic contact. Among the myriad of applications to which nanoindentation is applied, investigating film/substrate systems is one of the most common. However, from a modeling point of view, adding the substrate to the picture only further complicates the state of stress and strain at the contact. Despite these complexities, numerical simulations, empirical observations, and clever experiments have helped investigators find appropriate ways to deal with these issues and many others. As a result, nanoindentation data are routinely used to make significant contributions to the design and modeling of products as well as the investigation of structure-property relationships of new materials.

Tensile testing of free-standing thin films has been an active area of research for a number of years [2-7,19-29]. In general, these efforts have met with success in characterizing samples with dimensions as small as 500 x 50 x 2 μm, respectively, in length, width, and thickness. However, as the dimensions decrease (particularly the ratio of thickness to length), it becomes more and more difficult to achieve the load and displacement resolution required to make meaningful measurements. Data in the literature show strain softening, and oddly, both increases and decreases in the elastic modulus [3,5,20,21]. Explanations for these observations are heavily debated, not the least of which is the method by which the data were acquired and possible measurement errors. Among the most prevalent methods are micro-tensile systems that utilize speckle pattern techniques to determine the strain [29]. Recently, techniques implementing electrostatic actuation and laser interferometry have been developed by De Boer et al. [25,26].

Due to its high resolution in load, displacement, and *x-y* positioning, nanoindentation is also well suited to probing the mechanical response of free-standing thin films. Among the first to utilize nanoindentation techniques in characterizing free-standing thin films was Espinosa [27]. Further refinements in modeling the data from these experiments have been developed by Zhang [28]. The Membrane Deflection Experiment (MDE) uses a commercially available nanoindentation system to mechanically deflect a free-standing thin film. Because of concerns about the effect of thermal drift on the measured

displacement, Espinosa incorporated a Mirau interferometric microscope directly below the specimen to independently measure the deflection of the film. Using finite element analysis, Zhang et al. developed a very thorough and complex model of the bridge deflection, incorporating the support post compliances and bending moments. While Espinosa's concerns regarding the impact of thermal drift are well founded and Zhang's numerical analysis is exceedingly meticulous, by careful experimental technique and attention to the design of the test structure structure, it is possible to greatly simplify the testing and modeling of free-standing thin film bridges using nanoindentation.

In this work, frequency specific nanoindentation techniques are used to determine the elastic modulus and residual stress of thin films in the form of a doubly-clamped, free-standing bridge. The technique is termed frequency specific because among the measured signals is the sample's displacement response to an oscillating load driven at a single frequency. The sample's response to the normal load, on the other hand, is considered a broad-band measurement because the displacement signal carries noise from a wide spectrum of frequencies. In contrast to existing models in the literature that estimate the elastic modulus and residual stress based on the relationship between a broad-band measurement of load and displacement, we propose a simple membrane model to estimate the modulus and residual stress based on the relationship between stiffness and displacement, both of which can be directly measured. This measurement technique is advantageous for two

reasons: first, it improves the signal-to-noise ratio in comparison to broad-band measurements of load and displacement, and second, by relying on the stiffness as opposed to the load, the adverse effects of thermal drift are minimized. By controlling the geometry and dimensions of the film, it is possible to achieve simple conditions of stress and strain, and by modeling the film deformation as a membrane, the mathematical description is simple to implement. Based on an estimate of the film properties, dimensional analysis provides a robust means of determining the appropriate bridge geometry to ensure the experiment is consistent with the assumptions of the membrane model.

1.1. Sample geometry and properties

Experimental examination of the proposed technique was carried out on four Al/0.5 wt% Cu thin film bridges with four different geometries. Table 1 summarizes the sample identification and dimensions of each film. Fig. 3.1 is an SEM image which shows the layout of the thin film bridges and adjacent cantilever beams. The test structures were fabricated by the Microelectronics Development Laboratory at Sandia National Laboratories. Among their important attributes are: 1) their dimensions and properties are generally consistent with the assumptions of the proposed model, that is, the films are nominally flat, bending behavior is minimized, and the support posts are relatively rigid, all of which are key assumptions of the proposed model, and 2) the microstructure and

mechanical behavior of similar structures has been previously characterized, thus providing the comparative basis needed to evaluate the accuracy of Young's modulus, *E*, and the residual stress, σ_r, estimated by the proposed method. A detailed account of the fabrication technique, the resulting microstructure, and the mechanical behavior of the films as determined by electrostatic actuation are available in a recent publication [26].

The films were dc-magnetron sputter-deposited at 175 ^{o}C. Grain orientation mapping showed a strong $\langle 111 \rangle$ texture normal to the surface and random orientation in the plane of the film. The expected value of *E* is 68 GPa [26], while the value measured by De Boer using an electrostatic actuation technique is 74.4 ± 2.8 GPa. It is assumed that these values, which match within 9%, are representative of the 4 films studied in this investigation.

The comparative basis for σ_r is not as simple, as it depends on the fabrication technique and the thickness of the film. De Boer's electrostatic measurements found that σ_r varied from one batch to the next, but it is very consistent as a function of bridge length within a batch, as would nominally be expected. The bi-axial residual stress was measured on as-deposited blanket films, although meaningful comparisons with the thin film bridges could not be made because of significant stress relief in the films due to the fabrication process. Data from De Boer's electrostatic technique showed the average σ_r to be 29.9 MPa ± 0.3 MPa. For similar films, the average grain size was found to be 1.75 μm ± 1 μm

and the yield strength was in the range from 150 to 172 MPa. Interferograms showed the bridges to be nominally flat along the long axis and curved downward across their width, with a radius of curvature of approximately 62 μm.

2. Theory

2.1. The proposed membrane model

Fig. 3.2 is a schematic illustration of the membrane deflection experiment, where *l* and *w* are, respectively, the length and width of the bridge, *P* is the applied normal load, and *h* is the measured displacement or bridge deflection distance. Although not explicitly shown in the illustration, the thickness of the film is denoted as *t*. In response to a line load across the center of the bridge applied by a wedge indenter, the elastic deformation of the structure gives a relationship of the form:

$$P = \frac{8AEh^3}{l^3} - \frac{8A\sigma_r h^3}{l^3} + \frac{4A\sigma_r h}{l}, \qquad (1)$$

where *A* is the cross-sectional area. The second term of this expression makes a significant contribution only when σ_r is large in comparison to *E*; otherwise, it can be safely ignored. The derivation of Eq. 1 is provided in Appendix 1. It is important to note that the series approximation used to derive Eq. 1 limits the applicability of the *P*-*h* relationship to small strains, i.e., it is limited to the analysis

of elastic deformation. Differentiating Eq. 1 with respect to the vertically imposed displacement yields a stiffness-displacement (*S*-*h*) relationship, given by:

$$S = \frac{dP}{dh} = \frac{24AEh^2}{l^3} - \frac{24A\sigma_r h^2}{l^3} + \frac{4A\sigma_r}{l}. \quad (2)$$

Thus, a linear fit to experimentally determined *S* vs. h^2 data should yield a slope of

$$m = \frac{24AE}{l^3} - \frac{24A\sigma_r}{l^3}, \quad (3)$$

and an intercept of

$$b = \frac{4A\sigma_r}{l}. \quad (4)$$

Therefore, the residual stress can be measured from the intercept using:

$$\sigma_r = \frac{bl}{4A}, \quad (5)$$

and the elastic modulus from the slope as

$$E = \frac{\left(m + \frac{6b}{l^2}\right) l^3}{24A}. \quad (6)$$

The fundamental assumptions of this model are as follows: the film is flat, the load is applied at the center of the bridge, the deflection is normal and elastic, the support posts are rigid, and the bending moments may be ignored, which is to say the deformation of the film is accommodated by stretching as opposed to bending. In order to meet these criteria, the physical geometry of the test structure must reflect the stiffest possible post design supporting long, thin, narrow bridges that produce a small but measurable stiffness. While it is

possible to account for a finite post stiffness, it adds to the complexity of the modeling and the uncertainty of the test results in a manner that may be avoided through careful design of the test structure.

Close examination of bending behavior is useful because it provides additional physical insight into how the thin film bridge accommodates deformation. Using an analytical variational method and the principle of virtual work, Senturia examined the bending behavior by using a solution which assumes the deformed shape of the film can be described by a cosine function [4]. The resulting *P*-*h* relationship is

$$P = \frac{\pi^4 AEh^3}{8l^3} + \frac{\pi^4 AEt^2 h}{6l^3} + \frac{\pi^2 A\sigma_r h}{2l}. \tag{7}$$

The second term expresses the bending contribution, and in comparison to the membrane model, the first and third terms only differ in the magnitude of the numerical constants. It is important to understand, however, that the constants generated by this solution method may not be exact. As Senturia explained, only through additional finite element analysis can these values be confirmed or improved. An error in these constants, however, does not diminish the value of the solution, as it does provide the correct functional dependence between the properties of the film and its geometry. The corresponding *S*-*h* relationship is

$$S = \frac{dP}{dh} = \frac{3\pi^4 AEh^2}{8l^3} + \frac{\pi^4 AEt^2}{6l^3} + \frac{\pi^2 A\sigma_r}{2l}. \tag{8}$$

In comparison to the membrane model (Eq. 2), this expression clearly shows that bending behavior does not change the slope of linear relationship between *S* and

h^2, it only contributes to the *y*-intercept. This is an important observation because it indicates that evaluations of the elastic modulus from the membrane model are insensitive to the effect of bending. On the other hand, σ_r may be overestimated when bending makes a significant contribution.

2.2. Limitations of the model

While bending behavior does not affect the membrane model's ability to predict *E*, it can affect the predicted value of σ_r. Casting Eq. 8 in a non-dimensional form provides a convenient means of determining the extent to which the membrane model can be expected to overestimate σ_r when bending makes a significant contribution. The non-dimensional form of the *S*-*h* relationship for Senturia's bending model is

$$\frac{Sl}{AE} = \frac{3\pi^4}{8}\left(\frac{h}{l}\right)^2 + \frac{\pi^4}{6}\left(\frac{t}{l}\right)^2 + \frac{\pi^2}{2}\frac{\sigma_r}{E}. \tag{9}$$

The utility of the non-dimensional groups $\left(\frac{h}{l}\right)^2$, $\left(\frac{t}{l}\right)^2$, and $\left(\frac{\sigma_r}{E}\right)$, is in identifying which parameters control how the deformation of the film is accommodated as a function of displacement. More specifically, they can be used to determine the extent to which bending behavior contributes to the magnitude of the *y*-intercept in the linear relationship between *S* and h^2. The non-dimensional group from the first term, $\left(\frac{h}{l}\right)^2$, increases as the structure is vertically displaced during an

experiment. This term begins with a magnitude of zero and becomes more and more significant as the vertical displacement increases. The remaining two groups, $\left(\frac{t}{l}\right)^2$ and $\left(\frac{\sigma_r}{E}\right)$, are both fixed for a given test structure, and thus, their contribution is independent of the vertical displacement. In comparing the parameters $\left(\frac{\sigma_r}{E}\right)$ and $\left(\frac{h}{l}\right)^2$, it is clear that the initial stiffness is dominated by either σ_r or, a combination of σ_r and bending. It is precisely the combination of σ_r and bending that needs to be avoided in application of the membrane model. As the parameter $\left(\frac{h}{l}\right)^2$ increases during an experiment, the contributions of σ_r and bending to the measured stiffness become less and less important. In comparing the parameters $\left(\frac{\sigma_r}{E}\right)$ and $\left(\frac{t}{l}\right)^2$, it is clear that bending (the second term of the equation) can be safely ignored only in the limit that $\frac{\pi^2}{2}\left(\frac{\sigma_r}{E}\right) >> \frac{\pi^4}{6}\left(\frac{t}{l}\right)^2$. It should be recalled, however, that the magnitude of the numerical constants in Senturia's model lack numerical and experimental verification.

Table 1 summarizes the dimensions and the magnitude of $\left(\frac{t}{l}\right)^2$ for each of the four films investigated in this study. As discussed above, it is possible to

determine the contribution of bending in each film by estimating $\frac{\pi^2}{2}\left(\frac{\sigma_r}{E}\right)$ and comparing it to $\frac{\pi^4}{6}\left(\frac{t}{l}\right)^2$. Based on grain orientation mapping and De Boer's electrostatic measurements, *E* is assumed to be 70 GPa. For the thickest films (which are expected to exhibit the most significant bending contribution), De Boer found σ_r = 30 MPa, and thus, $\left(\frac{\sigma_r}{E}\right) = 4.286 \times 10^{-4}$. Table 1 shows that the maximum value of $\left(\frac{t}{l}\right)^2$ is 1.449 x 10^{-5}, which as expected, corresponds to the shortest and thickest film (3568 C3 short). In comparing the two terms, $\frac{\pi^2}{2}\left(\frac{\sigma_r}{E}\right)$ is approximately 9 times larger than $\frac{\pi^4}{6}\left(\frac{t}{l}\right)^2$. Thus, bending contributes 10% to the initial stiffness, which means the membrane model can be expected to overestimate σ_r by 10%. However, the predicted overestimation should not be taken as absolutely definitive since the numerical constants in Eq. 8 lack verification.

3. Experimental measurements

The membrane deflection experiments were performed using a Nano Indenter® XP and DCM (MTS Nano Instruments), both utilizing the continuous stiffness

measurement (CSM) technique. Details of the CSM technique have been described previously [8]. Because CSM experiments are used here to measure small changes in large values of stiffness, it is critical to characterize the dynamic stiffness of the instrument as accurately as possible using methods described elsewhere [18]. For both the XP and DCM, the displacement is calibrated using a laser interferometer and the load is calibrated using traceable weights. The theoretical resolution in load is 50 nN (XP) and 1 nN (DCM) and in displacement is 0.01 nm (XP) and 0.0002 nm (DCM). In practice, the instruments are limited by the noise floor in the electronics and environmental effects such as mechanical vibrations. In well controlled laboratory conditions, frequently observed noise levels with the indenter hanging in free space are of the order of 3 nm for the XP and 0.6 nm for the DCM. However, these values improve by nearly an order of magnitude when the indenter is in contact with the surface of a sample. Both the XP and the DCM are load controlled, and the noise associated with the load command signal is less than the noise associated with the measured displacement. Thus, noise in the applied load is primarily a reflection of the noise in displacement, since the applied load depends on the deflection of the support springs. The membrane deflection experiments were performed using a 90 degree diamond wedge indenter with an edge length of 50 μm. The profiling experiments used to determine the film thickness were performed with a blunt Berkovich indenter oriented face forward and a piezo motion stage that has sub-nanometer lateral resolution.

The length of each bridge was measured using the optical microscope and *x*-*y* translation stages of the XP, which have a lateral resolution of 1 μm or better. The width was measured using the optical microscope of the XP and the piezo motion stage. The thickness was determined by profiling cantilever beams adjacent to the thin film bridges (the cantilevers are shown in Fig. 3.2). Details of the thickness measurements are discussed in section 3.2.

Using a process of trial and error, residual impressions left by the wedge indenter in the surrounding structure were used to align the long axes of the bridges perpendicular to the edge of the wedge. It is important to note that no attempt was made to level the sample with respect to the 50 μm edge. Based on the geometry of the residual impressions, the angle between the surface of the film and the edge of the indenter was no more than 3 degrees.

3.1. Minimizing thermal drift effects

As previously noted, a key advantage of the frequency specific technique is that by relying on the measured stiffness as opposed to the load, the effect of thermal drift can be minimized to the point that it is no longer an experimental concern. In general, bridge deflection experiments cover large displacements, $h > 1000$ nm, in a short period of time ($t < 100$ s). Assuming typical thermal drift rates, $\dot{h} \leq 0.1$ nm/s, the Δh due to thermal drift is generally small in comparison to the

magnitude of the displacement and can be safely ignored. However, thermal drift also affects the applied load. As the springs that support the indenter shaft respond to a thermal transient, their change in shape manifests itself as a change in the applied load. In most applications, the change in load is extremely small in comparison to the magnitude of the applied load and can be safely ignored. However, in applications where the applied load is small (P < 50 μN), it is quite possible that thermal drift may generate a force that is a significant fraction of the applied load. The factors that determine the magnitude of the change in load are the stiffness of the support springs, the thermal drift rate, and the time of the experiment, $\left(\Delta P = K_{springs}\dot{h}t\right)$. For the stiffest bridge examined here, which requires the *largest* normal load, the maximum h = 3 μm was achieved in 225 s and required P = 85 μN. Assuming a spring stiffness K_{spring} = 100 N/m and $\dot{h}$ = 0.2 nm/s, then ΔP = 4.5 μN, which is 5.3% of the applied load. Clearly, this problem becomes worse for more compliant films, as less load is required to achieve the same displacement. In addition, thermal drift also impacts the unloading data by giving the appearance of hysteresis, and the final load is incorrect by $2\Delta P$ = 9 μN. However, directly measuring the stiffness as a function of displacement completely avoids these problems.

While maximizing the thermal stability of the environment and decreasing the measurement time reduces the ΔP associated with thermal drift, there are additional factors to consider. In performing faster experiments, it is important to recognize that the measurement time constants and damping can also play an

important role in obtaining accurate *P*-*h* data. In fact, the effect of the displacement time constant and the damping both scale directly with the velocity of the indenter. The faster it moves, the further the measured displacement lags behind the actual, and the more force is absorbed by the available damping. Although these factors can be experimentally accounted for, they are completely avoided utilizing the proposed CSM technique.

Fig. 3.3 shows the measured *P*-*h* and *S*-*h* data from an experiment performed on sample 3568 C2 short. Although the *P*-*h* data suggest the film has plastically deformed, the *S*-*h* data clearly show the response is dominated by elasticity, as the loading and unloading curves are virtually indistinguishable (the repeatability in *S* vs. *h* is shown in Fig.'s 3.6 and 7). The hysteretic behavior of the *P*-*h* data is an experimental artifact due to the aforementioned thermal drift and the effect of damping in the measurement system. In addition, the measured *S*-*h* data are clearly more sensitive to the point of contact, as the change in stiffness at the point of contact is abrupt, in contrast to the change in load which is virtually imperceptible. Collectively, these data demonstrate that the *P*-*h* response is much more susceptible to the adverse effects of thermal drift and thus not well suited to estimating the mechanical properties of the film.

3.2. Determination of the film thickness

Regardless of the choice to use a conventional membrane deflection experiment (reliance on the measured *P*-*h* response) or the proposed CSM technique (reliance on the measured *S*-*h* response), accurate measurements of the mechanical properties of the film are critically dependent on determining the geometry of the bridge. While the length and width are relatively easy to determine, the thickness is more challenging. Here, we have used the nanoindentation system as a profilometer to determine the film thickness. As shown in Fig. 3.1, adjacent to the thin film bridges were a series of cantilever beams that were produced in parallel with the bridges. Because both structures were produced at the same time, the bridge thickness is taken to be that of the cantilevers. Using a blunt Berkovich indenter tip, the nanoindenter was used to push the cantilevers down to the substrate. The cantilevers were then profiled across their width using 6 μN of force and the tip oriented face forward. The lateral motion of the sample was controlled using a piezo motion stage. The film thickness was determined by evaluating the step height on both sides of the cantilever.

Fig. 3.4a shows the profile height as a function of lateral position for a cantilever structure on sample 3568 C2. As indicated by the data, the left side measures 551.0 nm ± 1.2%, the right side 542.6 nm ± 1.0%. Using the average of the two, the film thickness for all three bridges on sample 3568 C2 was taken to be 547

nm. This result correlates well with De Boer's profilometer measurements, which gave $t \approx 600$ nm on films from the same batch. Fig. 3.4b shows the profile data from the cantilever structures on samples 3568 C3. As the data show, the left side measures 573.8 nm ± 2.0%, the right side 566.9 nm ± 3.0%. Using the average of the two, the film thickness for sample 3568 C3 is taken to be 571 nm. The film thickness values are summarized in Table 1.

In considering all possible sources of error in the proposed method, our experience is that film thickness determination is among the weakest links in the process. Although profiling experiments are typically straight forward, profiling a delicate cantilever whose shape can be unpredictable due to residual stress introduces new challenges that are difficult to overcome, as buckling makes it more difficult to find common criteria that can be used to develop a robust method that does not damage the cantilever during the process. If the cantilever films could be adhered to the substrate by some means of stiction or electrostatics, the profiling experiments could be significantly more robust.

3.3. The measured stiffness-displacement response of doubly-clamped, free-standing thin film bridges

The goal of this experiment was to measure the *S*-*h* response of the thin film bridges, and then estimate *E* and σ_r from the data. As dictated by the modeling,

the bridge's were assumed to be flat, the load was applied to the center of the bridges, the deflection was assumed to be normal and elastic, the support posts were assumed to be rigid, and bending moments were ignored. As previously noted, De Boer's laser interferometric measurements indicated the fabrication technique produces films that are nominally flat along the long axis of the bridge and curved downward across their width with a radius of approximately 69 μm. Optical interference microscope images of 150 and 500 μm long bridges showed the bridges to be flat to within 20 and 35 nm, respectively. However, in contrast to the laser interferometric measurements, a profile across the width of the 150 μm bridge showed the bridge is slightly curved upward with an approximate radius of 1300 μm. Despite this discrepancy, these data demonstrate that the fabrication technique produces nominally flat films. It is therefore assumed, that all 4 films in this investigation are nominally flat. For each bridge tested, the wedge indenter was positioned within 1 μm or better of the center of the bridge by performing a microscope-to-indenter calibration on the structure immediately surrounding it. As will be demonstrated, the experimentally acquired *S*-*h* data were dominated by elasticity since the loading and unloading data were virtually indistinguishable. Although no attempt was made to align the edge of the wedge tip and the surface of the film, any deviation from normal deflection of the film is assumed to be small, as the geometry of residual impressions left by the wedge in a soft Al indicated a misalignment less than 3 degrees. The microfabrication technique developed at Sandia was specifically designed to minimize the support post compliance. De Boer's experimental investigation found no length

dependence in σ_r (l = 150, 300, and 500 μm), which suggests the support posts are in fact rigid. For each thin film bridge, the influence of bending behavior is predicted in the same fashion as outlined in section 2.2. As will be demonstrated, bending behavior is expected to make only a minimal contribution to the short and medium length films.

Data from the 3568 C3 short specimen were acquired on the Nano Indenter® DCM at 20 Hz using an oscillation amplitude (RMS) of 30 nm. Data from 3568 C2 short, medium, and long specimens were acquired on the Nano Indenter® XP at 45 Hz using oscillation amplitudes (RMS) of 40, 60, and 120 nm, respectively. It is assumed the Al/0.5% Cu thin films exhibit no significant time dependence at room temperature, and hence, the measured properties are taken to be independent of frequency. While increasing the oscillation amplitude does reduce the signal-to-noise ratio, it is possible that large amplitudes may affect the measured stiffness. The maximum ratio of oscillation amplitude to bridge length in this investigation is 0.075% (this is based on the peak-to-valley amplitude, which assuming a perfect sine wave, equals $2\sqrt{2}$ *RMS amplitude). In hindsight, it would have been advantageous to perform the experiments just below the instrument's resonant frequency, as this generally optimizes the measurement systems sensitivity to changes in stiffness and hence, improves the ability to detect the point of contact. The resonant frequency of the XP is typically 12 Hz; the DCM is about 180 Hz.

Fig. 3.5 shows the measured *S*-*h* response from a single experiment performed on sample 3568 C3 short. In general, this type of behavior was observed for all of the films in this investigation. As the data show, the stiffness is close to 0 N/m while the wedge indenter is approaching the surface of the film. At the point of contact the stiffness increases rapidly over the course of 170 nm as the wedge indenter comes into full contact across the width of the speciman, and in accordance with Eq. 2, plateaus at a value that is determined by the geometry of the film and σ_r, or, as dictated by Eq. 8, a combination of σ_r and bending behavior. Among the important observations in these data is the reversibility of the loading and unloading response, indicating that the deformation is entirely elastic. The initial ramp-up in the *S*-*h* response was observed in every experiment performed on all four films. The amplitude of the harmonic oscillation and the extent of indenter misalignment determine the magnitude of the ramp-up distance. For this sample (3568 C3 short), the peak-to-valley oscillation amplitude was 85 nm, which is consistent with the kink in the ramp and accounts for approximately one-half of the 170 nm ramp-up distance. The remaining increase in stiffness is presumably due to misalignment, which according to the width of the bridge and the displacement at which the stiffness plateaus ($h \approx 170$ nm), indicates that the misalignment is less than 1 degree. It is assumed that once the edge of the wedge indenter makes full contact with the surface of the film, the effect of the misalignment on the measured stiffness is negligible.

The measured *S*-*h* response was repeated four times on 3568 C3 short to a deflection distance of 2 μm, which corresponds to 1.3% of the bridge length. Fig. 3.6 shows the linear relationship between *S* and h^2. The loading and unloading data are plotted in black and the linear regression in red. Note the nearly constant slope as a function of h^2, as predicted by the membrane model. In accordance with Eqs. 5 and 6, the resulting *E* and σ_r are 75.3 GPa ± 1.0 GPa and 28.7 MPa ± 0.6 MPa, respectively. These results, as well as the slope and intercept values from the regression analysis, are presented in Table 2. In comparison to De Boer's electrostatic measurements, *E* agrees within 1.2% and σ_r within 4%. Agreement with the modulus in the literature is within 10.7%. As demonstrated by the linear relationship between *S* and h^2 and the good agreement in *E* and σ_r, the data appear to be nominally consistent with the assumptions of the membrane model. However, recalling the discussion from section 2.2, it is possible that bending behavior may cause the membrane model to overestimate σ_r in this film by as much as 10%.

In addition to comparison with De Boer's results and the literature modulus, the properties estimated by the membrane deflection experiment have also been evaluated as a function of bridge length, which is generally accepted to have no bearing on *E* or σ_r. Fig. 3.7 shows the linear relationship between *S* and h^2 for 8 measurements performed on the 3 samples. The data are plotted in black and the linear regression in red. As the plot shows, the data are more noisy in comparison to the data on 3568 C3 short, as the XP has less resolution and a

higher noise floor than the DCM. Despite the higher noise, the data are quite similar in that the slope is constant as a function of h^2. The resulting E and σ_r for each film are shown in the plot and presented in Table 2, along with the results of the linear regression. The estimated E from all 3 films match De Boer's results within 2%, and the expected literature E within 10.7%. The estimated σ_r, on the other hand, shows a length dependence, as the relative error scales with decreasing bridge length accordingly, -5.0%, 10.7%, and 19.1%. However, it is important to recognize that through the linear coefficient of thermal expansion, α, small changes in temperature can have a significant impact on the magnitude of σ_r. For Al, $\alpha = 23 \times 10^{-6}$/K, and assuming E = 75 GPa (the value estimated for these films) and $\Delta T = 3^{o}$C, the resulting change in stress is 5.2 MPa, which can easily account for the apparent length dependence.

4. Summary and conclusions

A new method for determining the elastic modulus and residual stress of doubly-clamped, free-standing thin film bridges has been developed. The technique relies on measuring the *S*-*h* response of the thin film bridge using frequency-specific, depth-sensing nanoindentation. The *S*-*h* data are modeled assuming the thin film bridge behaves as a membrane, which means that the deformation of the film is dominated by stretching as opposed to bending. The primary advantages of this technique are the improved signal-to-noise ratio in

comparison to broad-band measurements of load and displacement and, the minimization of problems associated with thermal drift in the measured displacement and the applied load. The post-test data analysis is simple to implement, requiring only the linear regression of experimentally acquired S vs. h^2.

Experimental verification of the proposed method was demonstrated on four Al/0.5% Cu free-standing films measuring nominally 22 μm wide, 0.55 μm thick, and 150, 300, and 500 μm long. The estimated modulus of the films match the value obtained from electrostatic techniques within 2%, and the expected literature E within 10.7%. Although the model's estimation of σ_r only matches the value measured by electrostatic techniques within 19.1%, this discrepancy can be attributed to a temperature change at the time of the measurements of only 3 ^{o}C. Collectively, these results demonstrate that the membrane model accurately describes the role of the elastic modulus and the residual stress in controlling the deformation of the thin film bridge and that these properties can be estimated using nanoindentation and the CSM technique to measure the stiffness-displacement response of the thin film bridge.

References

[1] Spearing, S. M., Acta mater. **48** (2000) 179-196.

[2] Nix, W. D., Metall. Trans. A, (1989), **20A**, 2217.

[3] Huang, H. and Spaepen, F., Acta mater. **48** (2000) 3261-3269.

[4] Senturia, S. D., Microsystem Design, Kluwer Publishers (2001) Boston.

[5] Haque, M. A. and Saif, M. T. A., Scripta Materialia **47** (2002) 863-867.

[6] Heinen, D., Bohn, H. G. and Schilling, W., J. Appl. Phys. **77** (1995) 3742.

[7] Read, D. T., Meas. Sci. Technol. **9** (1998) 676.

[8] Oliver, W. C. and Pharr, G. M., J. Mater. Res. **19** 1 (2004) 3.

[9] Hay, J. L. and Pharr, G. M., ASM Handbook **8** (2000) 232.

[10] Herbert, E. G., Oliver, W. C. and Pharr, G. M., Phil. Mag. **86** (2006) 5521.

[11] Taljat, B. and Pharr, G. M., Mater. Res. Soc. Symp. Proc. **594** (2000) 519-524.

[12] Pharr, G. M., Harding, D. S. and Oliver, W. C., Mechanical Properties and Deformation Behavior of Materials Having Ultra-Fine Microstructures, Kluwer Publishers (1993) Boston.

[13] Lucas, B. N. and Oliver, W. C., Metall. Mater. Trans. A **30** (1999) 601.

[14] Northen, M. T. and Turner, K. L., Sensors and Actuators A: Physical, **130-131** (2006) 583-587.

[15] M. R. VanLandingham, J. Res. Natl. Inst. Stand. Technol. **108** 4 (2003) 249.

[16] M. L. Oyen, R. F. Cook, J. Mater. Res. **18** 1 (2003) 139.

[17] C. A. Tweedie, K. J. Van Vliet, J. Mater. Res. **21** (2006) 1576.

[18] Herbert, E. G., Oliver, W. C. and Pharr, G. M., J. Phys. D: Appl. Phys. **41** (2008) 074021.

[19] Kraft, O and Volkert, C. A., Adv. Eng. Mater. **3** (2001) 99.

[20] Emery, R. D. and Povirk, G. L., Acta Materialia **51** (2003) 2067.

[21] Emery, R. D. and Povirk, G. L., Acta Materialia **51** (2003) 2079.

[22] Read, D. T. and Dally, J. W., J. Mater. Res., **8**, 7, (1993) 1542.

[23] Lee, D., Wei, X., Chen, X., Zhao, M., Jun, S. C., Hone, J., Herbert, E. G., Oliver, W. C. and Kysar, J.W, Scripta Materialia **56** (2007) 437.

[24] Su, Y.-J., Qian, C.-F., Zhang, T.-Y., Zhao, M.-H., and Zhang, T.-Y., Acta mater. **48** (2000) 4901-4915.

[25] De Boer, M. P., DelRio, F. W. and Baker, M. S., Acta Materialia, currently in press.

[26] De Boer, M. P., Corwin, A. D., Kotula, P. G., Subhash, G. and Shaw, M. J., Acta Materialia, currently in press.

[27] Espinosa, H. D., Prorok, B. C. and Fischer, M., J. Mech. and Phys. of Solids **51** (2003) 47.

[28] Zhang, T.-Y., Su, Y.-J., Qian, C.-F., Zhao, M.-H., and Chen, L.Q., Acta mater. **48** (2000) 2843-2857.

[29] Huh, Y. H., Kim, D., Hahn, J. H., Kim, G. S., Kee, C. D., Yeon, S. C. and Kim, Y. H., Mater. Res. Soc. Symp. Proc. **875** (2005) O4.15.

Acknowledgements

Sandia is a multiprogram laboratory operated by Sandia Corporation, a Lockheed Martin Company, for the United States Department of Energy under contract DE-AC04-94AL85000.

Appendix 3.1.

Fig. 3.A1 shows the free body diagram of the membrane deflection experiment illustrated in Fig. 3.2. Summing forces in the *x* and *y* directions reveals the uniaxial force in the film,

$$\overset{+}{\rightarrow}\sum F_y = 0 \Rightarrow F_2\cos\theta - F_1\cos\theta = 0 \Rightarrow F_2 = F_1 = F$$

and (A1)

$$\overset{+}{\uparrow}\sum F_z = 0 \Rightarrow F\sin\theta + F\sin\theta - P = 0 \Rightarrow 2F\sin\theta - P = 0 \Rightarrow F = \frac{P}{2\sin\theta}. \quad \text{(A2)}$$

The strain is defined based on the geometry of the deformed film,

$$\sin\theta = \frac{2h}{l+\Delta l}, \quad \text{(A3)}$$

$$\tan\theta = \frac{2h}{l}, \quad \text{(A4)}$$

and thus

$$\varepsilon = \frac{\Delta l}{l} = \frac{2h}{l\sin\theta} - 1 = \frac{2h}{l\sin\left[\tan^{-1}\left(\frac{2h}{l}\right)\right]} - 1. \quad \text{(A5)}$$

Assuming the deformation of the bridge is elastic, the stress in the bridge may be expressed

$$\sigma = \frac{F}{A} = E\varepsilon + \sigma_r, \quad \text{(A6)}$$

and thus,

$$F = A\left(E\varepsilon + \sigma_r\right). \quad \text{(A7)}$$

Recalling Eq. A2,

$$F = \frac{P}{2\sin\theta} = A\left(E\varepsilon + \sigma_r\right), \quad \text{(A8)}$$

and therefore,

$$P = 2A\left(E\varepsilon + \sigma_r\right)\sin\theta\,. \tag{A9}$$

Substituting Eq. A5 for the ε (strain as a function of sin θ) and simplifying leads to the following expression,

$$P = \frac{4AEh}{l} - 2AE\sin\theta + 2A\sigma_r \sin\theta \tag{A10}$$

A trigonometric series approximation is used in place of the term sin θ in order to define the angle in terms of the displacement,

$$\tan^{-1}(x) = x - \frac{1}{3}x^3 + \frac{1}{5}x^5 - \ldots \quad \text{for } x^2 < 1 \tag{A11}$$

$$\sin(x) = x - \frac{x^3}{3!} + \frac{x^5}{5!} - \frac{x^7}{7!} + \ldots \tag{A12}$$

$$\sin\left(x - \frac{x^3}{3}\right) = x - \frac{x^3}{2} \tag{A13}$$

$$\sin\theta = \sin\left[\tan^{-1}\left(\frac{2h}{l}\right)\right] = \frac{2h}{l} - \frac{\left(\frac{2h}{l}\right)^3}{2} = \frac{2h}{l} - \frac{4h^3}{l^3} \tag{A14}$$

Replacing the sin θ term in Eq. A10 and simplifying yields the final *P-h* relationship written in terms of the geometry and properties of the thin film bridge,

$$P = \frac{8AEh^3}{l^3} - \frac{8A\sigma_r h^3}{l^3} + \frac{4A\sigma_r h}{l}\,. \tag{A15}$$

It is important to recognize that utilization of the trigonometric series approximation limits the applicability of the *P-h* relationship to small angles.

Appendix 3.2.

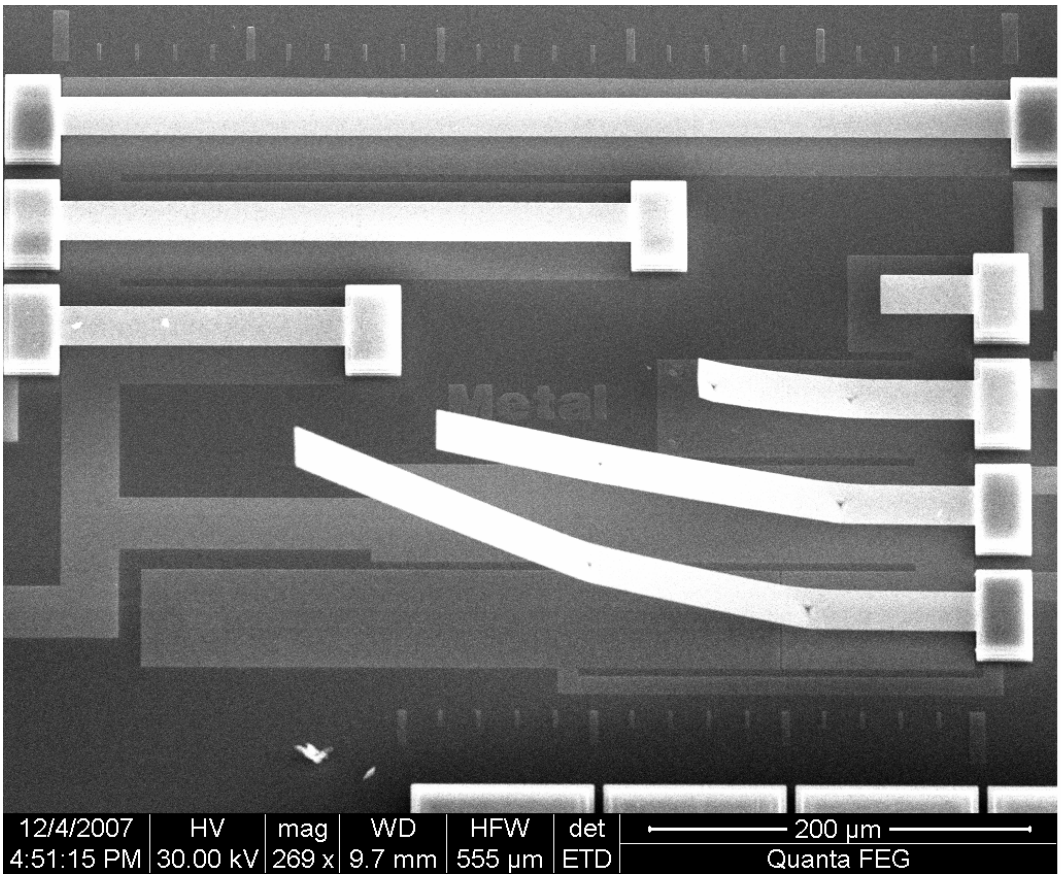


Figure 3.1. SEM image of the test structure, showing the thin film bridges and cantilevers on sample 3568 C3.

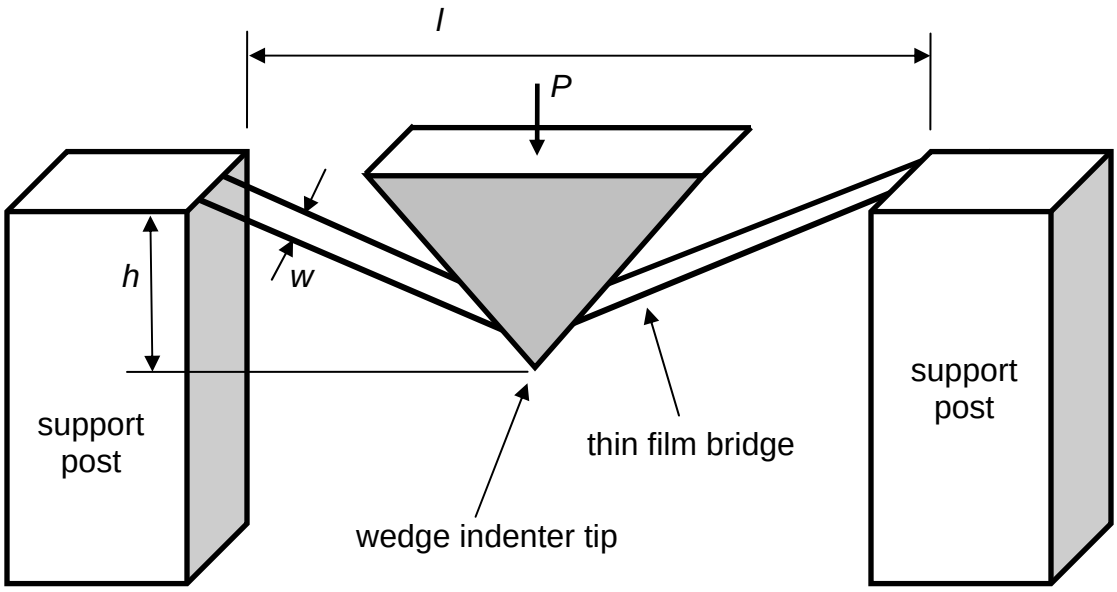


Figure 3.2. Schematic illustration of the Membrane Deflection Experiment (MDE). The support posts are assumed to be rigid and the film is modeled as a membrane (it does not support bending moments).

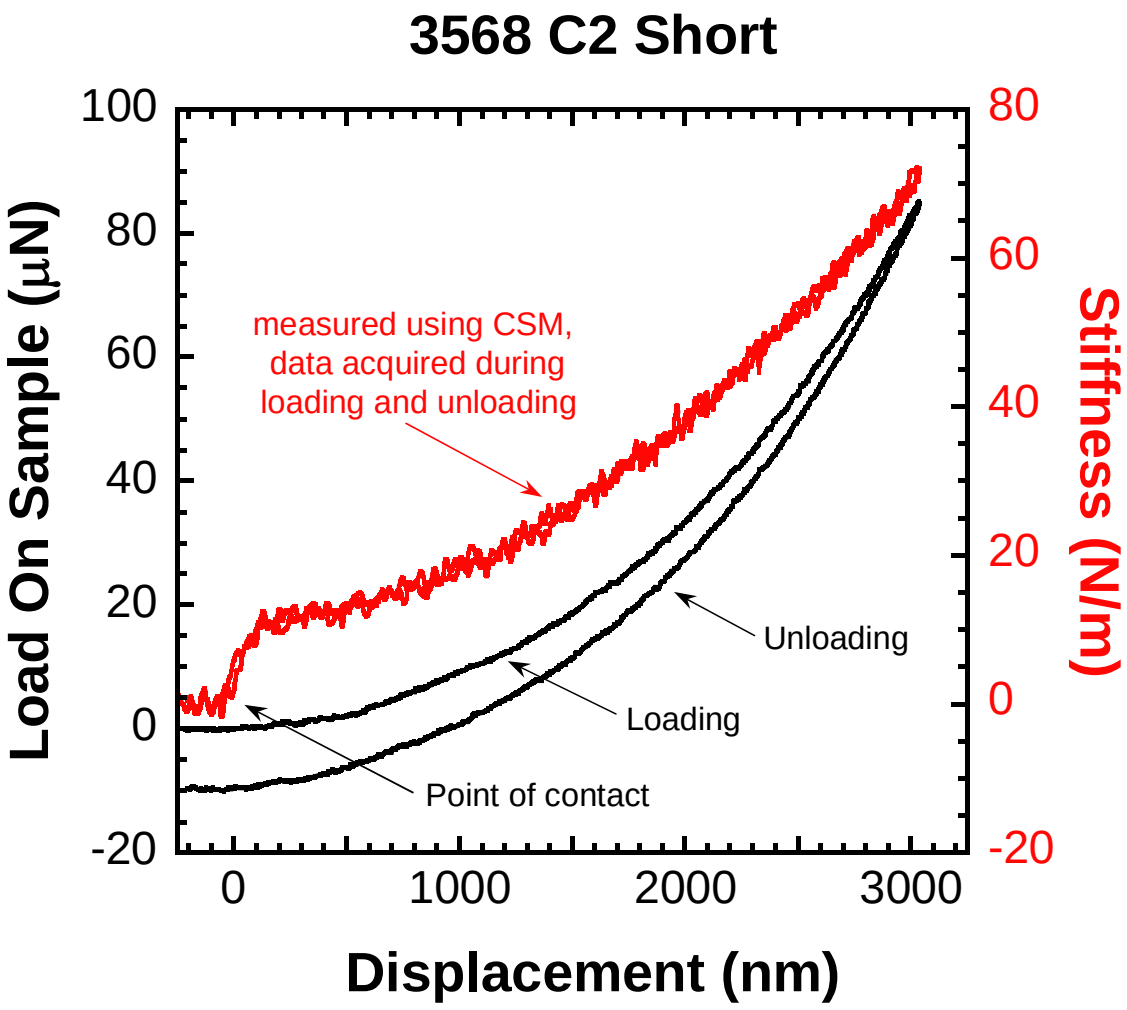


Figure 3.3. The load and stiffness as a function of deflection distance. The reversibility of the *S-h* data indicate the behavior is dominated by elasticity. The hysteretic *P-h* behavior is an experimental artifact due to thermal drift and the damping in the measurement system.

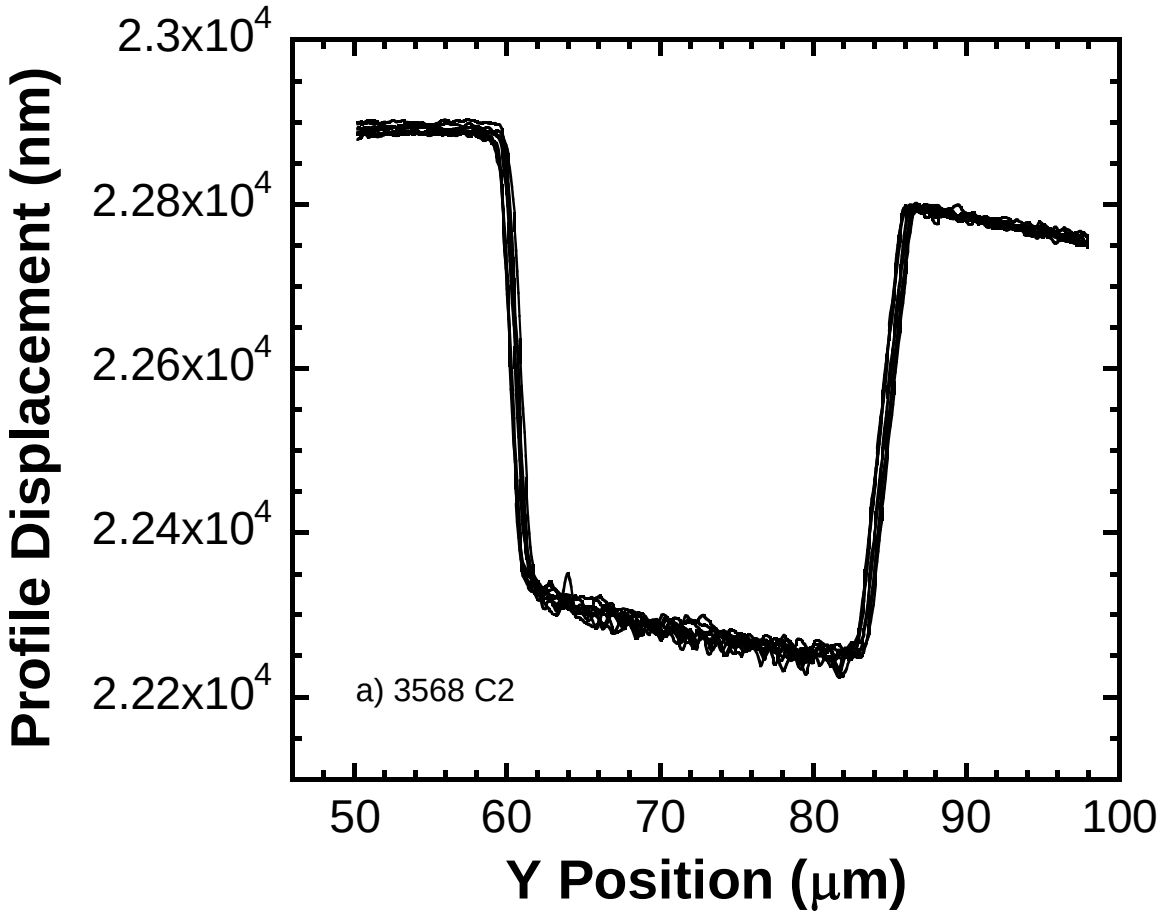


Figure 3.4. Film thickness measurements performed on the cantilever beams, a) samples 3568 C2 short, medium, and long, b) sample 3568 C3 short.

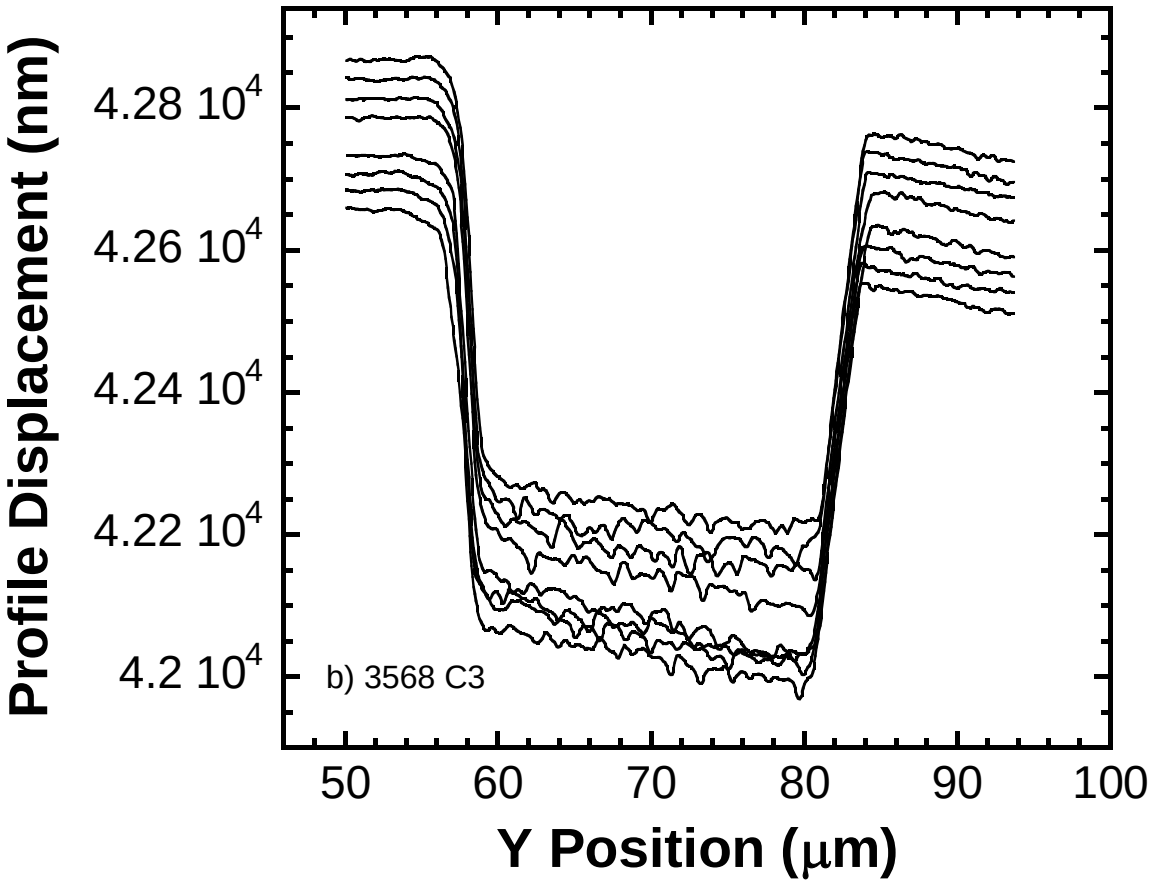


Figure 3.4. Continued.

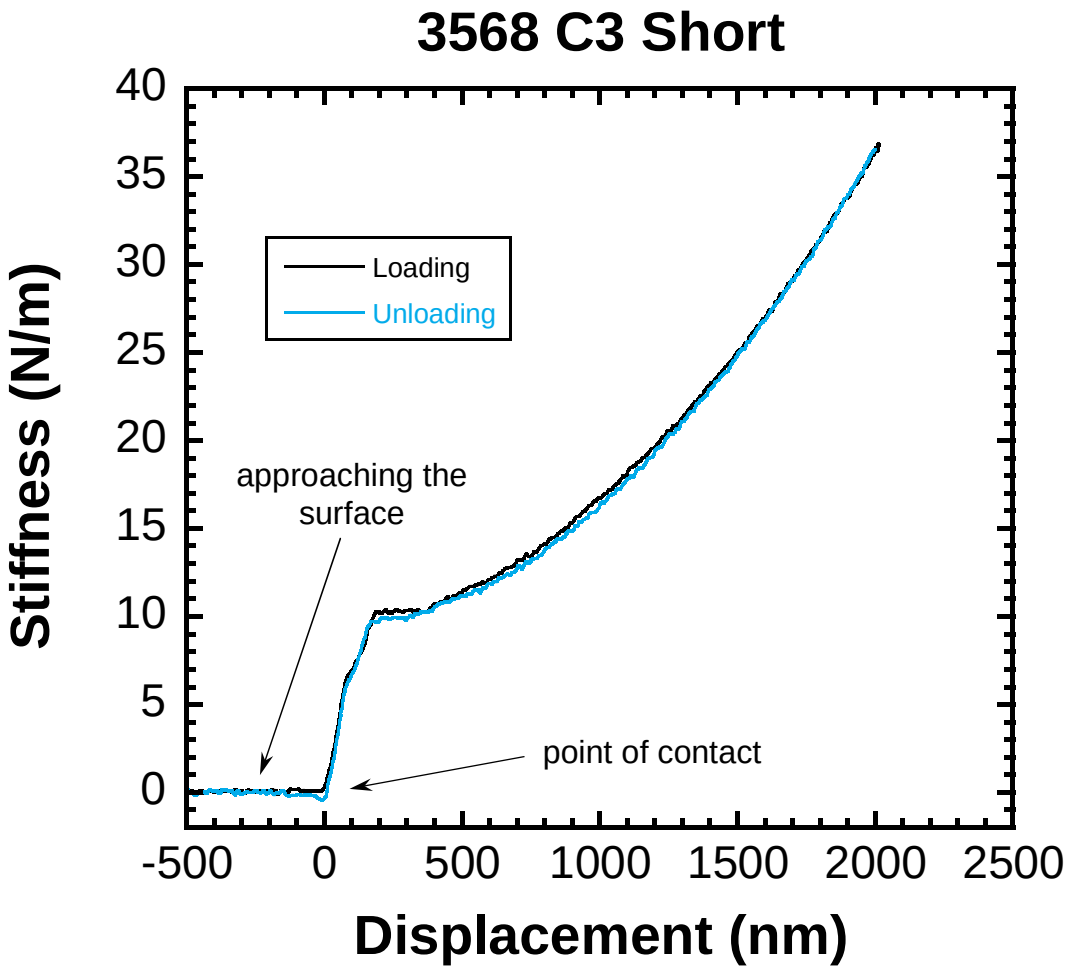


Figure 3.5. *S* vs. *h*, taken on sample 3568 C3 short. The data clearly show the point of contact and illustrate the films behavior is dominated by elasticity, as the loading and unloading are quite repeatable.

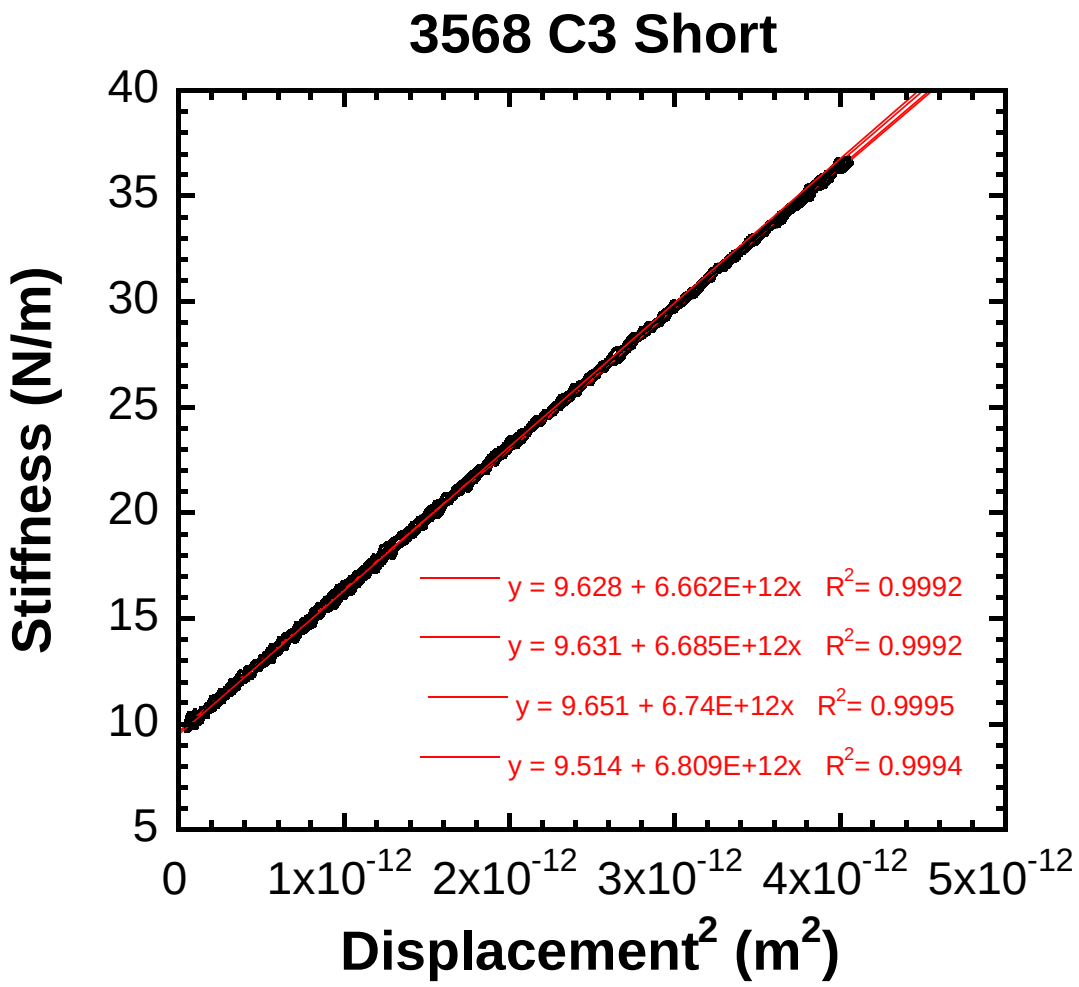


Figure 3.6. *S* vs. h^2, taken on 3568 C3 short. As the data show, the slope is relatively constant as a function of h^2, as predicted by the membrane model.

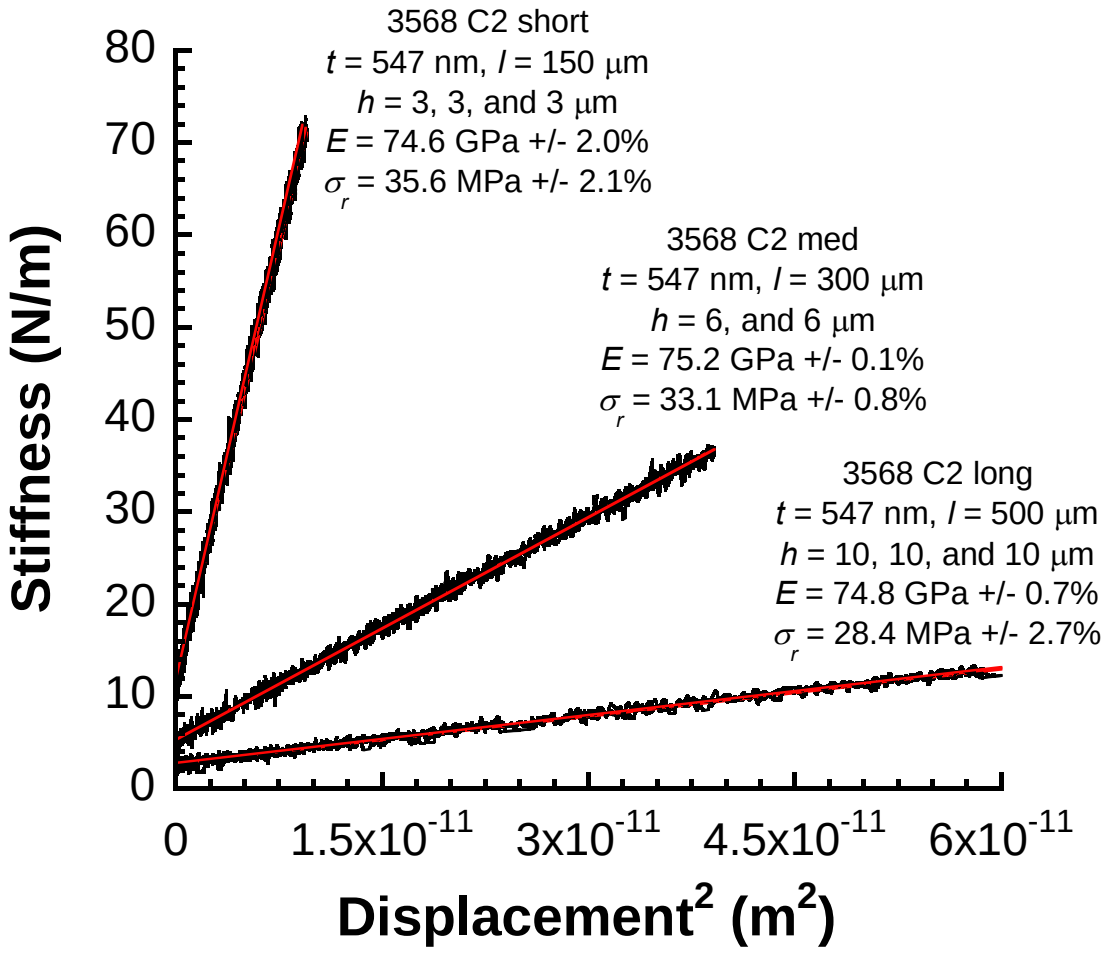


Figure 3.7. *S* vs. h^2 for the 8 measurements performed on the 3568 C2 short, medium, and long bridges.

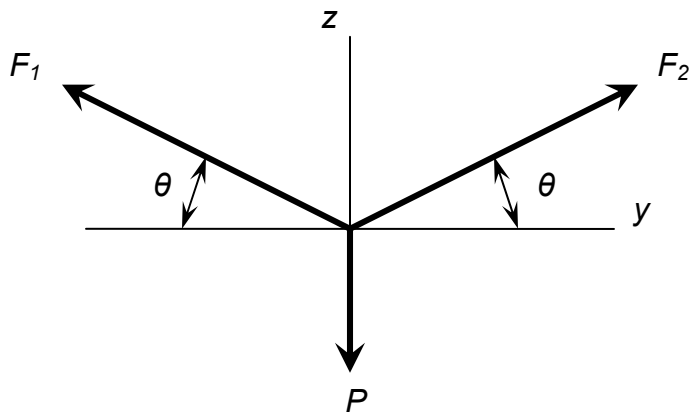


Figure 3.A1. A free body diagram of the membrane deflection experiment.

Table 3.1. Sample identification, dimensions, and the magnitude of $\left(\frac{t}{l}\right)^2$.

Sample ID	*Length, l* (μm)	*Width, w* (μm)	*Thickness, t* (μm)	$\left(\frac{t}{l}\right)^2$
3568 C2 long	500	22	0.547	1.197E-6
3568 C2 medium	300	22	0.547	3.325E-6
3568 C2 short	150	22	0.547	1.33E-5
3568 C3 short	150	22	0.571	1.449E-5

Table 3.2. Results summary.

Sample ID & dimensions (l, w, t) [µm]	*Freq. [Hz], & osc. amp. [nm]*	*Deflection, h* [µm]	*Slope* [N/m^3]	*y-intercept* [N/m]	*E* [GPa]	σ_r [MPa]
3568 C2 long	45, 120	10	1.71E$^+$11	2.69	74.2	27.9
(500, 22, 0.547)		10	1.73E$^+$11	2.69	75.1	27.9
		10	1.73E$^+$11	2.82	75.1	29.3
					74.8 ± 0.7	*28.4 ± 2.7*
3568 C2 med	45, 60	6	8.05E$^+$11	5.29	75.3	33.0
(300, 22, 0.547)		6	8.04E$^+$11	5.35	75.2	33.3
					75.2 ± 0.1	*33.1 ± 0.8*
3568 C2 short	45, 40	3	6.27E$^+$12	11.20	73.3	34.9
(150, 22, 0.547)		3	6.35E$^+$12	11.39	74.3	35.5
		3	6.52E$^+$12	11.67	76.2	36.4
					74.6 ± 2.0	*35.6 ± 2.1*
3568 C3 short	20, 30	2	6.66E$^+$12	9.63	74.6	28.8
(150, 22, 0.571)		2	6.68E$^+$12	9.63	74.9	28.8
		2	6.74E$^+$12	9.65	75.5	28.8
		2	6.81E$^+$12	9.51	76.3	28.4
					75.3 ± 1.0	*28.7 ± 0.6*

Vita

Erik Gregory Herbert was born in Boston, MA on October 20, 1969. He was raised in Massachusetts, New Hampshire, Pennsylvania, and Tennessee. He graduated from Anderson County High School in 1987. He received a B.A. in political science with a minor in business administration from the University of Tennessee, Knoxville, in 1992. He received his M.S. in Materials Science and Engineering from the University of Tennessee, Knoxville, in 2006. Erik has been a full time employee at the MTS Nano Instruments Innovation Center in Oak Ridge, TN since 1998.